

UPC

CTTC

On the Numerical Simulation of Compressible Flows

Centre Tecnològic de Transferència de Calor
Departament de Màquines i Motors Tèrmics
Universitat Politècnica de Catalunya

Juan Bautista Pedro Costa
Doctoral Thesis

On the Numerical Simulation of Compressible Flows

Juan Bautista Pedro Costa

TESI DOCTORAL

presentada al

Departament de Màquines i Motors Tèrmics
E.S.E.I.A.A.T.
Universitat Politècnica de Catalunya

per a l'obtenció del grau de

Doctor per la Universitat Politècnica de Catalunya

Terrassa, Maig 2019

On the Numerical Simulation of Compressible Flows

Juan Bautista Pedro Costa

Director de la tesi

Dr. Assensi Oliva Llena

Tutor de la tesi

Dr. Carles David Pérez-Segarra

Tribunal Qualificador

Cristobal Cortés Gracia
Universidad de Zaragoza

Francesc Xavier Trias Miquel
Universitat Politècnica de Catalunya

Antonio Lecuona Newman
Universidad Carlos III de Madrid

*This thesis is dedicated to
mamá y papá*

*Cuando estés acorralado y no haya esperanza de un mañana, no desesperes.
Y recuerda, más grande será la caída.
Etcétera...*

- Coronel Jack O'Neill.

Agradecimientos

Quiero agradecer a toda la gente que ha hecho posible la realización de este trabajo.

En primer lugar, a los Profs. Asensi Oliva y Carles David Pérez Segarra, catedráticos del *Centre Tecnològic de Transferència de Calor* (CTTC) por haberme descubierto el mundo del CFD durante mis años de estudiante y haberme proporcionado la oportunidad de realizar el doctorado en este departamento. También por su ayuda y confianza a lo largo de estos años.

A Aleix Bàez, mi mentor y amigo, quién me adentró en el mundo de la simulación de flujos compresibles y me ha guiado durante el desarrollo de mi trabajo. Gràcies pel teu temps i consell !

También quiero agradecer al resto de compañeros del laboratorio que me han acogido como a uno más y me han ayudado en todo momento. Especial mención a Santi y Nico por acogerme y ayudarme en mis primeros momentos, a Jordi Chiva por su ayuda al programar, a Octavi por su soporte para poder desarrollar mi trabajo sin problemas y a Oriol Lehmkuhl, Ivette Rodríguez y Jordi Ventosa por haberme ayudado en los diferentes proyectos en los que hemos colaborado a lo largo de estos años.

En el ámbito personal también quiero agradecer a mis padres por su apoyo incondicional, tanto emocional como económico, a mis amigos por mantenerme distraído de vez en cuando y a mis hermanos de Opatov por proporcionarme los mejores momentos de mi vida.

Abstract

In this thesis, numerical tools to simulate compressible flows in a wide range of situations are presented. It is intended to represent a step forward in the scientific research of the numerical simulation of compressible flows, with special emphasis on turbulent flows with shock wave-boundary-layer and vortex interactions. From an academic point of view, this thesis represents years of study and research by the author. It is intended to reflect the knowledge and skills acquired throughout the years that at the end demonstrate the author's capability of conducting a scientific research, from the beginning to the end, present valuable genuine results, and potentially explore the possibility of real world applications with tangible social and economical benefits. Some of the applications that can take advantage of this thesis are: marine and offshore engineering, combustion in engines or weather forecast, aerodynamics (automotive and aerospace industry), biomedical applications and many others. Nevertheless, the present work is framed in the field of **compressible aerodynamics** and **gas combustion** with a clear target: aerial transportation and engine technology. The presented tools allow for studies on sonic boom, drag, noise and emissions reduction by means of geometrical design and flow control techniques on subsonic, transonic and supersonic aerodynamic elements such as wings, airframes or engines. Results of such studies can derive in new and ecologically more respectful, quieter vehicles with less fuel consumption and structural weight reduction.

We start discussing the motivation for this thesis in chapter one, which is placed into the upcoming second generation of supersonic aircraft that surely will be flying the skies in no more than 20 years. Then, compressible flows are defined and the equations of motion and their mathematical properties are presented. Navier Stokes equations arise from conservation laws, and the hyperbolic properties of the Euler equations will be used to develop numerical schemes.

Chapter two is focused on the numerical simulation with Finite Volumes techniques of the compressible Navier-Stokes equations. Numerical schemes commonly found in the literature are presented, and a unique hybrid-scheme is developed that is able to accurately predict turbulent flows in all the compressible regimens (subsonic, transonic and supersonic). The scheme is applied on the flow around a NACA0012 airfoil at several Mach numbers, showing its ability to be used as a design tool in order to reduce drag or sonic boom, for example. At subsonic regimens, results show excellent agreement with reference data which allowed the study of the same case at transonic conditions. We were able to observe the buffet phenomenon on the airfoil, which consists of shock-waves forming and disappearing, causing a dramatic loss of aerodynamic performance in a highly unsteady process.

To perform a numerical simulation, however, boundary conditions are also required in addition to numerical schemes. A new set of boundary conditions is intro-

duced in chapter three. They are developed for three-dimensional turbulent flows with or without shocks. They are tested in order to asses its suitability. Results show good performance for three-dimensional turbulent flows with additional advantages with respect traditional boundary conditions formulations.

Unfortunately, compressible flows usually require high amounts of computational power to its simulation. High speeds and low viscosity result in very thin boundary layers and small turbulent structures. The grid required in order to capture this flow structures accurately often results in unfeasible simulations. This fact motivates the use of turbulent models and wall models in order to overcome this restriction. Turbulent models are discussed in chapter four. The Reynolds-Averaged Navier Stokes (RANS) approach is compared with Large-Eddy Simulation (LES) with and without wall modeling (WMLES). A transonic diffuser is simulated in order to evaluate its performance. Results showed the ability of RANS methods to capture shock-wave positions accurately, but failing in the detached part of the flow. LES, on the other hand, was not able to reproduce shock-waves positions accurately due to the lack of precision on the shock wave-boundary-layer interaction (SBLI). The use of a wall model, nevertheless, allowed to overcome this issue, resulting in an accurate method to capture shock-waves and also flow separation. More research on WMLES is encouraged for future studies on SBLIs, since they allow three-dimensional unsteady studies with feasible levels of computational requirements.

With all these tools, we are able to solve at this point any problem concerned with the aerodynamic design of high-speed vehicles which were identified in previous paragraphs.

Finally, multi-component flows are discussed in chapter five. Our hybrid scheme is upgraded to deal with multi-component gases and tested in several cases. We demonstrate that with a redefinition of the discontinuity sensor multi-components flows can be solved with low levels of diffusion while being stable in the presence of high scalar gradients.

As a result of the work of this thesis, a complete numerical approach to the numerical simulation of compressible turbulent multi-component flows with or without discontinuities in a wide range of Reynolds and Mach numbers is proposed and validated. Direct applications can be found in civil aviation (subsonic and supersonic) and engine operation.

Contents

Abstract	v
Nomenclature	xi
1 Introduction	1
1.1 Motivation	1
1.2 Compressible flows	2
1.3 Mathematical formulation	3
1.3.1 Conservation laws	3
1.3.2 Gas dynamics	5
1.3.3 Hyperbolicity	10
1.3.4 An analytical example: The Sod's Shock Tube	12
1.4 Numerical methods	15
1.5 Objectives of the thesis	18
1.6 Outline of the thesis	18
References	19
2 A hybrid numerical flux for discontinuous turbulent compressible flows.	21
2.1 Introduction	21
2.2 State of the Art	21
2.2.1 Shock-capturing schemes	23
2.2.2 Energy-consistent schemes	24
2.2.3 Shock-capturing techniques	25
2.2.4 Open issues	28
2.3 Development of a hybrid numerical scheme	29
2.3.1 Kinetic energy preserving	30
2.3.2 Numerical diffusion	31
2.3.3 Shock capturing	36
2.3.4 Discretization of viscous fluxes	37
2.4 Numerical tests	37
2.4.1 The Shock Tube Problem	37
2.4.2 Advection of a two-dimensional isentropic vortex	39
2.4.3 Taylor-Green Vortex Problem	42
2.4.4 Supersonic Cylinder	44
2.5 Application on the flow around a NACA0012 airfoil	45
2.6 Conclusions	53
References	56

3 Boundary conditions for turbulent compressible flows.	61
3.1 Introduction	61
3.2 State of the art	62
3.3 Development of new boundary conditions	64
3.3.1 Fluid-type boundary conditions	65
3.3.2 Solid-type boundary conditions	67
3.4 Numerical tests	68
3.4.1 Acoustic pulse	68
3.4.2 Two-dimensional vortex advection	68
3.4.3 Driven Cavity	70
3.4.4 Flow over a circular cylinder	71
3.5 Conclusions	74
References	76
4 Turbulence modeling for discontinuous turbulent compressible flows.	79
4.1 Introduction	79
4.2 State of the art	80
4.2.1 More on SBLIs	81
4.3 Turbulence modeling	82
4.3.1 RANS	85
4.3.2 LES	88
4.3.3 WMLES	89
4.4 Numerical tests	92
4.4.1 Channel Flow	92
4.4.2 Sajben's transonic diffuser	96
4.5 Conclusions	100
References	103
5 Multi-component turbulent compressible flows.	107
5.1 Introduction	107
5.2 State of the art	108
5.3 Multi-component Navier Stokes equations	110
5.4 Upgrading the hybrid flux	114
5.5 Numerical tests	116
5.5.1 Non-reactive propane Jet	116
5.6 Conclusions	119
References	122
6 Conclusions and Further Research	125
6.1 Conclusions	125
6.2 Further research	128

A The Shock Tube Problem	131
B Computing Resources	135
References	135
C Publications	137

Nomenclature

		Symbols
$A = \partial f / \partial \phi$	Jacobian matrix	α
A_f	face area	Δt
a	speed of sound	Δx
c_p, c_v	heat capacities	δ_{ij}
E	total energy	γ
e	specific internal energy	κ
e_k	specific kinetic energy	Λ
F	discrete flux function	λ
f	flux function	μ
$f' = \partial f / \partial \phi$	Jacobian matrix	μ_T
H	total enthalpy	$\nabla = (\frac{\partial}{\partial x}, \frac{\partial}{\partial y}, \frac{\partial}{\partial z})$
h	specific enthalpy	Ω
L_{ss1}, L_{ss2}	Larsson sensor constants	$\partial \Omega$
m	mass	ω
$\mathbf{n} = (n_x, n_y, n_z)$	face unitary normal vector	Φ
p	pressure	ϕ
\mathbf{q}	heat flux	$\tilde{\phi}$
R	eigenvectors matrix	ρ
R_g	gas constant	τ
r	eigenvector of A	
T	temperature	
t	time	
$\mathbf{u} = (u, v, w)$	flow velocity	
V_i	volume of the i th control volume	
$\mathbf{x} = (x, y, z)$	vector position	

Introduction

The main topic of this research is the **numerical simulation of compressible flows**. In this introductory chapter, the motivation of this thesis is discussed. Then, compressible flows are defined, the **equations of motion** are presented and their physical and mathematical **properties** are explained. As an example of application, the shock tube problem is analytically solved in order to understand all the concepts related to the phenomenology of compressible fluids and their numerical study. Based on the issues presented, the main **objectives** and **outline** of the thesis are derived.

1.1 Motivation

This thesis finds its sense for existence in the numerous and strong investments in supersonic civil aviation and private space exploration at the present time (2017). Supersonic civil aviation as a transportation method born in the 80s, with the appearance of the Concorde. Nevertheless, the numerous problems, delays and accidents even with human casualties, resulted in a premature cancellation of the technology around the world. A second generation of supersonic aircraft never saw the light of day, due in part in the interest in other scientific areas such as space exploration and nuclear energy.

The difficulties that a supersonic vehicle manufacturer must face are numerous. First, developing a supersonic engine and do it eco-friendly and economically competitive represent a major challenge. The Concorde could consume over 166 ml of fuel per passenger and kilometer, number that differs drastically from those of big subsonic jetliners (16-44 ml for models such as the A330, B747 or A380). The figure does not vary too much if it is compared with private subsonic jets (148 ml for the G550). It is at this point where the “second coming” of supersonic aviation finds its sweet spot: long private travels where passengers value most speed and comfort than cost. Second, the aerodynamic performance of the aircraft represents also a major problem. A vehicle **drag** increases with its drag coefficient, air density and the

square of the velocity. This means that the faster the vehicle moves, more force is required to move it and more fuel is consumed. Since the objective is to move as fast as possible, designers can only play with the other two factors. Low air density is achieved by flying as high as possible. A small drag coefficient is achieved by shaping the vehicle in a particular way that limit heavily the rest of the design. Furthermore, supersonic vehicles are subjected to wave drag at transonic speeds, caused by **shock waves**. This can result in an increase of 4 times the drag coefficient, that reduces to 30 to 50 % at full supersonic speed. The fact that a supersonic aircraft must transition between the different compressible regimens (subsonic at take off and landing, transonic and supersonic at cruise) require all the aircraft elements to perform at every stage, which in turns results in a heavy design constrain. The Concorde had an aerodynamic performance (ratio between lift and drag) of 7.14, in contrast to 17 of the B747.

Other aerodynamic aspect that limit supersonic vehicles is the **sonic boom**, caused by shock waves, that restrict the supersonic operation of these aircraft on isolated zones such as over the ocean. New advances on sonic boom reduction, using tools similar to the ones presented in this thesis, promise to overcome this problem allowing the operation of supersonic aircraft on populated areas. Finally, other issues such as extra R&D costs, materials (the Concorde could achieve over 127 ° C at Mach 2), specific production techniques and other technical issues are also challenging.

At the end of the day, a Concorde ticket for London-New York at the late 90s was priced at around 10k \$, which is the price of the same route nowadays of first class travels. Considering that today the total travel time is more than twice, this can be seen as an opportunity and a motivation for the second coming of supersonic (and hypersonic) transportation. NASA is investing in supersonic projects focused on sonic boom reduction with the reactivation of its X-planes program and, like Airbus, is collaborating with private companies such as Reaction Engines, Aerion or Boom in the development of private supersonic jets. In words of NASA: "We're on the cusp of a new era in aviation that is dramatically cleaner, quieter, and even faster". Another fact that is promoting supersonic aviation is the threats at which subsonic aviation is subjected, with the development of faster trains and upcoming technologies (such as the Hyperloop) that seriously threatens the aviation domination in short to middle distance flights.

1.2 Compressible flows

A **fluid** is called **compressible** when its density varies significantly in response to a change in other thermodynamic property, in general pressure. For example, a change in pressure of 500 kPa results in a change in air density of 250 %, meanwhile this change is only of 0.024 % in the case of water (considering ambient temperature and

fluids at rest). Although all fluids are compressible this effect is less significant for liquids than for gases, which leads to the general treatment of liquids (and gases at low speed) as incompressible fluids. Compressible effects are characterized by the **Mach number** (Ma), which is the ratio between the flow velocity and the speed of sound. In the case of the air, if $Ma < 0.2 - 0.3$, the incompressibility assumption can be made. When the incompressibility assumption cannot be made, or more accurate results are required, the compressible model has to be used along with the required numerical techniques that will be explained throughout this thesis.

Many industrial **applications** rely on the use of compressible fluids, such as the study of resistance of ships or wave impacts on vessels (marine and offshore engineering), combustion in engines, climate control in the passenger compartment, aerodynamics (automotive and aerospace industry) and also biomedical applications such us respiratory flow in lungs.

The equations that describe the motion of compressible fluids are the **Navier-Stokes** (NS) equations. This system of non-linear equations cannot be solved analytically, except for a few exceptional cases. This is the reason why the numerical analysis is used in order to get an approximate solution of these equations. Computational Fluids Dynamics, or **CFD**, is the field of the fluids mechanics responsible for the numerical study of the NS equations, and the characterization of fluids behavior in any possible situation of interest.

1.3 Mathematical formulation

In the following, polytropic ideal gas (in particular air) with constant c_p is assumed. The generalization to multi-component real gases will be discussed in chapter 5.

1.3.1 Conservation laws

Conservation laws arise from physical principles [1]. Consider the simplest fluid dynamics problem, in which a one-dimensional flow with known velocity which can be written as a function of distance and time, i.e. $u(x, t)$. Let $\rho(x, t)$ be the density of the gas, the function to be determined. Consider a section of pipe $x_1 < x < x_2$, the total mass of the gas in the pipe is given by

$$m(t) = \int_{x_1}^{x_2} \rho(x, t) dx \quad (1.1)$$

If there is no creation or destruction of gas in this section (e.g. nuclear reactions) the total mass within this section only can change due to the flux or flow of particles

through the endpoints of the section at x_1 and x_2 .

$$\frac{\partial}{\partial t} \int_{x_1}^{x_2} \rho(x, t) dx = F_1(t) - F_2(t) \quad (1.2)$$

Here, $F_i(t)$ for $i = 1, 2$ are the fluxes at the endpoints. This is the basic integral form of a conservation law, and the basis of conservation. Roughly speaking, the variation of mass within the section is the sum of what is entering the section plus what is leaving it. Remember that $\rho(x, t)$ has to be computed. It is therefore required to relate the flux with the variable. In this case, the flux is given by the product of the density and the velocity

$$f(x, t) = u(x, t)\rho(x, t) \quad (1.3)$$

The function $f(x, t)$ is the flux function, and $F_i(t) = f(x_i, t)$. Since the velocity is known, the flux function reads $f(\rho(x, t))$.

$$\frac{\partial}{\partial t} \int_{x_1}^{x_2} \rho(x, t) dx = f(\rho(x_1, t)) - f(\rho(x_2, t)) \quad (1.4)$$

The function $\rho(x, t)$ that satisfies equation 1.4 cannot be directly found. Instead it is transformed into a partial differential equation that can be handled with standard techniques.

$$\frac{\partial}{\partial t} \int_{x_1}^{x_2} \rho(x, t) dx = - \int_{x_1}^{x_2} \frac{\partial}{\partial x} f(\rho(x, t)) dx \quad (1.5)$$

Or, manipulating

$$\int_{x_1}^{x_2} \left[\frac{\partial}{\partial t} \rho(x, t) dx + \frac{\partial}{\partial x} f(\rho(x, t)) \right] dx = 0 \quad (1.6)$$

Since the integral must be zero for all values of x_1 and x_2 , the final differential equation is

$$\frac{\partial}{\partial t} \rho(x, t) + \frac{\partial}{\partial x} f(\rho(x, t)) = 0 \quad (1.7)$$

Notice that the derivation of the differential equation requires that both $\rho(x, t)$ and $f(\rho(x, t))$ be smooth functions. This is true in most cases, but **discontinuities** may appear in the general treatment of compressible flows. This is an important fact, because when a discontinuity appears the differential conservation equation cannot be used and the integral form must be revisited.

Summarizing, the differential equation of a conservation law takes the form

$$\frac{\partial}{\partial t} \phi(x, t) + \frac{\partial}{\partial x} f(\phi(x, t)) = 0 \quad (1.8)$$

Here, ϕ is called the **conserved variable** (like the density in the previous development), and $f(\phi(x, t))$ is the **flux function** of the conserved variable. The main focus will be to compute $\phi(x, t)$, given the initial and boundary conditions. In order to use a more friendly notation, equation 1.8 is expressed as

$$\phi_t + f(\phi)_x = 0 \quad (1.9)$$

Where the subscripts t and x denote the partial derivatives with respect to time and space, respectively.

1.3.2 Gas dynamics

The science in the branch of fluid dynamics concerned with the study of motion of gases and its effects on physical systems is called **gas dynamics**. The studies in gas dynamics are often defined with gases flowing around or within physical objects at speeds comparable to or exceed the speed of sound and causing a significant change in temperature, density and pressure. These variables are related via conservation laws. In this subsection, the conservation laws that describe the motion of polytropic ideal gases, e.g. air, are presented [2]. They are the NS equations for compressible flows.

The Continuity Equation

The continuity equation was already derived in section 1.3.1. In the continuity equation the density is the conserved variable, and can only change due to the flux of density through the boundaries of the considered domain.

$$\frac{\partial}{\partial t} \int_{\Omega} \rho d\Omega + \int_{\partial\Omega} \rho \mathbf{u} \cdot \mathbf{n} dS = 0 \quad (1.10)$$

The differential form of the continuity equation is

$$\rho_t + \nabla \cdot (\rho \mathbf{u}) = 0 \quad (1.11)$$

The Momentum Equation

Consider a gas at rest, with $\mathbf{u} = 0$. Since the velocity is a macroscopic quantity that represents an average over the molecules of a gas, one cannot say that the gas is strictly at rest because the molecules are indeed moving, with their velocity. If a pressure difference is applied at the boundaries of the gas domain, an acceleration of the gas moving towards the zone with lower pressure will be seen. This means that the pressure has a contribution on the momentum flux. The viscosity of the fluid

also has a contribution in the momentum flux, which can be written (neglecting body forces) as

$$\frac{\partial}{\partial t} \int_{\Omega} \rho \mathbf{u} d\Omega + \int_{\partial\Omega} \rho \mathbf{u} (\mathbf{u} \cdot \mathbf{n}) dS + \int_{\partial\Omega} p \mathbf{n} dS - \int_{\partial\Omega} \boldsymbol{\tau} \cdot \mathbf{n} dS = 0 \quad (1.12)$$

The differential form of the momentum equation is

$$(\rho \mathbf{u})_t + \nabla \cdot (\rho \mathbf{u} \mathbf{u}) = \nabla \cdot \boldsymbol{\tau} - \nabla p \quad (1.13)$$

Viscous stress tensor is related to the strain rate through the Stokes' law

$$\boldsymbol{\tau}_{ij} = \mu \left[\left(\frac{\partial u_i}{\partial x_j} + \frac{\partial u_j}{\partial x_i} \right) - \frac{2}{3} \frac{\partial u_k}{\partial x_k} \delta_{ij} \right] \quad (1.14)$$

In case of air, viscosity can be computed using the Sutherland's law,

$$\mu = 1.461^{-6} \frac{T^{3/2}}{110.3 + T} \quad (1.15)$$

with T in K and μ in kg/ms .

The Energy Equation

The total energy is defined as

$$E = \rho e + \frac{1}{2} \rho \mathbf{u} \cdot \mathbf{u} \quad (1.16)$$

The term $\frac{1}{2} \rho \mathbf{u} \cdot \mathbf{u}$ is the kinetic energy and ρe is the internal energy, with e the specific internal energy (includes translational, rotational and vibrational energy and possibly other forms of energy in more complicated situation). If one assume that the gas is in local chemical and thermodynamic equilibrium, then the internal energy is a function of pressure and density

$$e = e(p, \rho) \quad (1.17)$$

This is called the equation of state of the gas. The integral form of the energy equation is

$$\frac{\partial}{\partial t} \int_{\Omega} E d\Omega + \int_{\partial\Omega} E \mathbf{u} \cdot \mathbf{n} dS + \int_{\partial\Omega} p \mathbf{u} \cdot \mathbf{n} dS - \int_{\partial\Omega} (\boldsymbol{\tau} \cdot \mathbf{u}) \cdot \mathbf{n} dS + \int_{\partial\Omega} \mathbf{q} \cdot \mathbf{n} dS = 0 \quad (1.18)$$

Where the work carried out by body forces has been neglected. The flux of energy is given by the advection of energy due to the velocity, the work done by the pressure and viscosity forces and the heat flux \mathbf{q} . The differential form of the energy equation is

$$E_t + \nabla \cdot ((E + p)\mathbf{u}) = \nabla \cdot (\boldsymbol{\tau} \cdot \mathbf{u}) - \nabla \cdot \mathbf{q} \quad (1.19)$$

The heat flux is obtained according to the Fourier's law,

$$\mathbf{q} = -\kappa \nabla T \quad (1.20)$$

where $\kappa = \frac{\mu c_p}{Pr}$, $c_p = 1004 \text{ J/kgK}$ and $Pr = 0.71$ for air.

The Equation of State

In order to close the problem the equation of state must be specified. For an ideal gas

$$de = c_v dT \quad (1.21)$$

where c_v is the specific heat at constant volume. If this coefficient is constant, the internal energy is proportional to the temperature T , i.e. $e = c_v T$. From the ideal gas law,

$$p = \rho R_g T \quad (1.22)$$

where R_g is obtained dividing the universal gas constant by the molecular mass of the gas. It can be established (assuming constant c_v)

$$e = \frac{c_v}{R_g} \frac{p}{\rho} \quad (1.23)$$

The specific enthalpy of the gas is defined

$$h = e + \frac{p}{\rho} \quad (1.24)$$

And for an ideal gas

$$dh = c_p dT \quad (1.25)$$

where c_p is the specific heat at constant pressure. By the ideal gas law

$$c_p - c_v = R_g \quad (1.26)$$

and defining the ratio of specific heats

$$\gamma = \frac{c_p}{c_v} \quad (1.27)$$

equation 1.23 can be written as

$$e = \frac{p}{(\gamma - 1)\rho} \quad (1.28)$$

Finally, total energy is obtained

$$E = \frac{p}{\gamma - 1} + \frac{1}{2}\rho\mathbf{u} \cdot \mathbf{u} \quad (1.29)$$

This is the relation that close the system. For air, under ordinary circumstances, $\gamma = 1.4$ and $R_g = 287 \text{ J/kgK}$.

Equations 1.11, 1.13 and 1.19 are the NS equations. They include second-order derivatives that make the system parabolic. They are more realistic than the Euler equations, which neglect viscosity and heat transfer terms. However, when the viscosity and heat conductivity are very small, the Euler equations are a good approximation. The resulting discontinuous shock waves are good approximations to what is observed in reality (very thin regions over which the solution is rapidly varying). If discontinuities location is unknown, the grid resolution required for the computation of NS equations would increase the computational costs. Euler equations can be used to find an approximate result, and then refine the model with the more realistic NS equations if the costs are admissible.

Non-dimensional NS Equations

In some cases, it is more useful to work with non-dimensional parameters. In order to derive the non-dimensional NS equations reference magnitudes have to be defined, resulting in the non-dimensional variables,

$$\begin{aligned} x^* &= \frac{x}{x_{ref}} & t^* &= \frac{t}{t_{ref}} & \rho^* &= \frac{\rho}{\rho_{ref}} & u^* &= \frac{u}{u_{ref}} \\ p^* &= \frac{p}{\rho_{ref}u_{ref}^2} & T^* &= \frac{T}{T_{ref}} & E^* &= \frac{E}{\rho_{ref}u_{ref}^2} \end{aligned}$$

Introducing the non-dimensional variables in the NS equations one gets,

$$\rho_t + \nabla \cdot (\rho\mathbf{u}) = 0 \quad (1.30)$$

$$(\rho\mathbf{u})_t + \nabla \cdot (\rho\mathbf{u}\mathbf{u}) = \nabla \cdot \boldsymbol{\tau} - \nabla p \quad (1.31)$$

$$E_t + \nabla \cdot ((E + p)\mathbf{u}) = \nabla \cdot (\boldsymbol{\tau} \cdot \mathbf{u}) - \nabla \cdot \mathbf{q} \quad (1.32)$$

$$p = \frac{\rho T}{\gamma Ma_{ref}^2} \quad (1.33)$$

The subscript $(\cdot)^*$ has been dropped in sake of simplicity. Notice that the equation of state is the only equation in the system that has changed, and it only involves the computation of the gas constant as $R_g = 1/\gamma Ma_{ref}^2$. The rest of relations still unchanged except for the viscosity and heat transfer coefficient,

$$\mu = \frac{T^{3/2}}{Re_{ref}} \frac{1.3686}{0.3686 + T} \quad \kappa = \frac{\mu}{(1 - \gamma)Ma_{ref}^2 Pr_{ref}} \quad (1.34)$$

As it can be seen, very few changes are applied on the overall formulation, so its implementation is straightforward. Alternative non-dimensional equations can be found in the literature, making use of a as reference velocity or introducing γ in the definition of reference magnitudes, for example. Nevertheless, these approaches complicate the overall numerical approach.

The three non-dimensional numbers that appear are the **Reynolds** number, the **Mach** number and the **Prandtl** number

$$Re = \frac{\rho u L}{\mu} \quad Ma = \frac{u}{a} \quad Pr = \frac{\mu c_p}{\kappa} \quad (1.35)$$

where $a = \sqrt{\gamma p / \rho}$ is the speed of sound. The Reynolds number is the relation between inertial forces and viscous forces within the flow. Compressible flows are generally low-viscosity fluids at high-speeds which lead to high-Reynolds numbers in almost every practical application. This means, in turn, turbulence and thin boundary layers which require fine grids to capture all the important details. The Mach number expresses the ratio between the fluid velocity and the speed of sound. As it will be explained, information propagates within the flow at the speed of sound relative to the fluid velocity. This property is used to classify compressible flows in different regimens: subsonic incompressible ($Ma < 0.3$), subsonic compressible ($0.3 < Ma < 1$), transonic ($Ma \approx 1$), supersonic ($1 < Ma < 5$) and hypersonic ($Ma > 5$). Below transonic conditions, compressible fluids are smooth and behaves similar to incompressible flows. But once transonic conditions are achieved, discontinuities in form of shock-waves can appear within the flow.

1.3.3 Hyperbolicity

Under the assumption that ϕ is smooth, equation 1.9 can be rewritten as

$$\phi_t + f'(\phi)\phi_x = 0 \quad (1.36)$$

where $f'(\phi) = \frac{\partial f}{\partial \phi}$ is the Jacobian matrix corresponding to the derivative of the flux function with respect to the conserved variable. In general, system of equations are faced, ϕ is a vector containing the several conserved variables and $f'(\phi)$ is a $m \times m$ matrix with m equal to the number of equations that form the system. For convenience, equation 1.36 is rewritten as

$$\phi_t + A\phi_x = 0 \quad (1.37)$$

where $A = f'(\phi)$. Equation 1.37 is written in the so called quasilinear, or **characteristic**, form. This linear system is called **hyperbolic** if the matrix A is diagonalizable with real eigenvalues $\lambda^1 \leq \lambda^2 \leq \dots \leq \lambda^m$. These eigenvalues are also called **characteristic values**. The matrix is diagonalizable if there is a complete set of eigenvectors, i.e., if there are nonzero vectors r^1, r^2, \dots, r^m such that $Ar^p = \lambda^p r^p$ for $p = 1, 2, \dots, m$.

Lets define the following matrices:

$$\Lambda = \begin{bmatrix} \lambda^1 & & \\ & \ddots & \\ & & \lambda^m \end{bmatrix} = \text{diag}(\lambda^1, \lambda^2, \dots, \lambda^m). \quad (1.38)$$

which is a diagonal matrix containing the characteristic values, and

$$R = \begin{bmatrix} r^1 & \dots & r^m \end{bmatrix} \quad (1.39)$$

is the eigenvectors matrix, containing the eigenvectors of the system. Notice that $A = R\Lambda R^{-1}$. The definition of these matrix allows to rewrite equation 1.37 as follows

$$R^{-1}\phi_t + R^{-1}ARR^{-1}\phi_x = \omega_t + \Lambda\omega_x = 0 \quad (1.40)$$

where ω is a vector containing the characteristic variables. Since Λ is a diagonal matrix, and each λ is real, equation 1.40 can be seen as a decoupled system of m wave equations that can be used to solve the original system of equations. Wave and conserved variables are related via the eigenvectors,

$$\phi = R\omega = \sum_{p=1}^m w^p r^p \quad (1.41)$$

The characteristic variables can be interpreted as waves traveling at a finite speed given by the characteristic value. The conserved variables can be seen, therefore, as the combination of m waves traveling at the characteristic speeds $\lambda^1, \lambda^2, \dots, \lambda^m$. With only one equation the hyperbolic analysis is quite simple (only one characteristic value, and the conserved and the characteristic variables are the same). When working with systems of equations, in order to develop a good numerical scheme, it is required to determine properly which waves are traveling at which speed and their relation with the conserved and primitive variables.

The NS equations are not hyperbolic, but parabolic, due to the viscous and heat transfer terms. Nevertheless, in the vast majority of compressible cases, these terms are almost negligible in the smooth parts of the flow. This means that far away from the boundary layers, where viscosity and heat transfer are dominant, the hyperbolic part of the system of equations play a major role. This fact is of vital importance in the presence of shock-waves, where information directionality must be addressed by the numerical scheme. This is the reason why classical schemes take advantage of upwind-like approaches. However, as it will be seen in the next chapter, they are not the best choice for turbulent problems.

Consider the one-dimensional Euler equations,

$$\frac{\partial}{\partial t} \begin{pmatrix} \rho \\ \rho u \\ E \end{pmatrix} + \nabla \cdot \begin{pmatrix} \rho u \\ \rho u^2 + p \\ (E + p)u \end{pmatrix} = 0 \quad (1.42)$$

In order to obtain the Jacobian matrix of the system the flux vector is derived with respect to the conserved variables,

$$A = \begin{bmatrix} 0 & 1 & 0 \\ \frac{1}{2}(\gamma - 3)u^2 & (3 - \gamma)u & \gamma - 1 \\ \frac{1}{2}(\gamma - 1)u^3 - uH & H - (\gamma - 1)u^2 & \gamma u \end{bmatrix} \quad (1.43)$$

Where $H = \frac{E-p}{\rho}$ is the specific total enthalpy. Now we can compute the eigenvalues,

$$\lambda = \begin{pmatrix} u - a \\ u \\ u + a \end{pmatrix} \quad (1.44)$$

and the eigenvectors,

$$R = \begin{bmatrix} 1 & 1 & 1 \\ u - a & u & u + a \\ H - au & \frac{1}{2}u^2 & H + au \end{bmatrix} \quad (1.45)$$

The Euler equations form, indeed, a hyperbolic system of equations. The conserved variables will be transported within the flow at the characteristic speeds given by λ

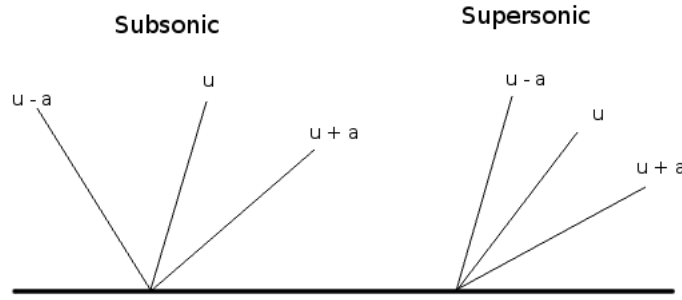


Figure 1.1: Waves diagram for the Euler equations traveling at the characteristic speeds at subsonic case (left) and supersonic (right).

in form of waves. Discontinuities within the flow will appear if $|u| > a$. Since the information cannot travel faster than the speed of sound, the flow will have to adapt to new conditions in small regions and short times, giving rise to what is called shock waves.

1.3.4 An analytical example: The Sod's Shock Tube

The aim of this subsection is to apply the previous concepts in a real application, as a first approach to hyperbolic systems of equations. This case is called the shock tube and, under some hypothesis, is possible to obtain its analytical solution [3]. Shock tubes have been used to measure dissociation energies and molecular relaxation rates, investigate shock wave behaviour, and they have been used in aerodynamic tests. The fluid flow in the driven gas (the gas behind the shock wave) can be used as a wind tunnel, allowing higher temperatures and pressures replicating the conditions in the turbine sections of jet engines. However, test times are limited to a few milliseconds, either by the arrival of the contact surface or the reflected shock wave. They have been further developed into shock tunnels, with an added nozzle and dump tank. The resultant high temperature hypersonic flow can be used to simulate atmospheric re-entry of spacecraft or hypersonic craft, again with limited

testing times.

The shock tube problem is also very useful to evaluate the shock-capturing capabilities of a numerical method. This test will be used in the next chapter, among other tests intended to give solid arguments involving the validation of the different numerical techniques developed in the context of this thesis.

rest with different thermodynamic properties (pressure, density and temperature). The pressure in the region $x < 0$ (the working gas), denoted by the subscript l , is higher than the pressure in the region $x > 0$ (the driven gas), denoted with the subscript r . At $t = 0$ the membrane suddenly breaks, generating the air flow in the tube. In the lower pressure region a shock wave travels at a speed D . Meanwhile, in the higher pressure region an expansion waves occur. Between the heated gas and the gas left behind by the expansion a contact discontinuity is placed that travels at the local air speed. As it can be seen, the problem present several discontinuities in the fluid properties. Accuracy in the correct capture of these discontinuities will be required for a numerical code, and the comparison between the numerical and exact solution will be useful in order to quantify the resolution of the different numerical schemes. All the details concerning the resolution of the problem can be found in appendix A.

Summarizing, characteristic lines are used to propagate the constant values of the Riemann variables through the tube. This procedure allows to compute u and a at any point, meanwhile p , ρ and T can be computed with equation A.3 and the equation of state. The change of the thermodynamic variables through the discontinuities are given by the conservation laws through them. The present solution is analytical, therefore exact. The exact solution for the Riemann problem is displayed in figure 1.2. Notice that the initial jump discontinuity is placed at $x = 0.5$. The solution is the same but delayed in the x -direction. This non-dimensional solution belongs to the following initial state, for $t = 0.2$.

$$\rho_l = 8 \quad p_l = 10/\gamma \quad u_l = 0 \quad \rho_r = 1 \quad p_l = 1/\gamma \quad u_r = 0 \quad (1.46)$$

It can be seen how the shock wave travels towards $x > 0$, giving motion to the fluid and increasing pressure, density and temperature. Between the shock wave and the contact discontinuity the properties remain constant. A jump in density and temperature occur in the contact discontinuity, but velocity and pressure do not change. Through the expansion wave, temperature, pressure and density smoothly decrease from the initial conditions at the left side meanwhile the fluid is accelerated. As it was already mentioned, notice the short time of the event (0.5 ms if reference pressure is 0.1 MPa and reference density is 1.25 kg m^{-3}).

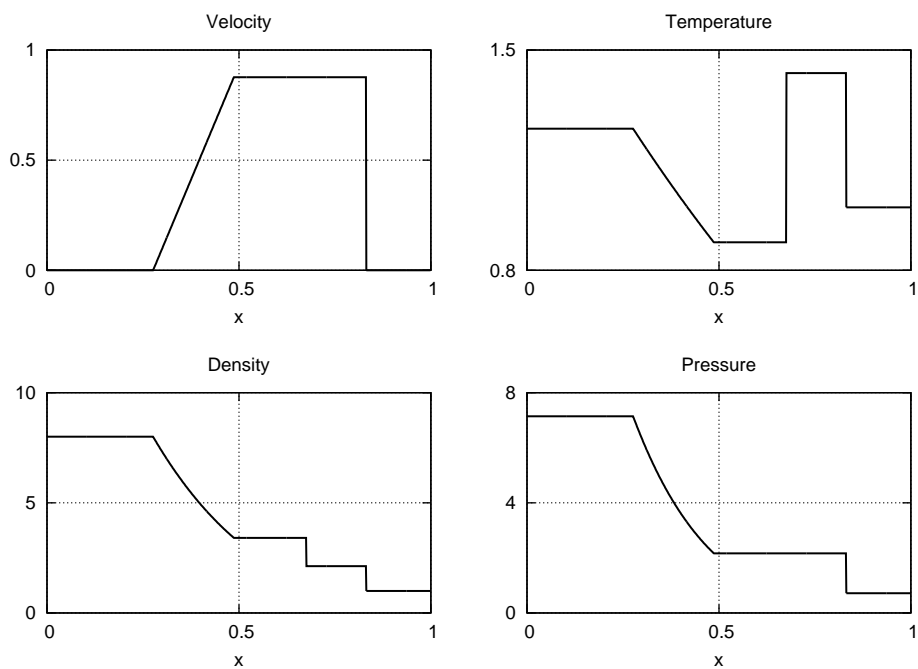


Figure 1.2: Non-dimensional exact solution for the Shock Tube problem at $t = 0.2$.

1.4 Numerical methods

Equations of motion have been introduced and their most important continuous properties have been presented. The **discretization** procedure is now discussed. Our objective is the development of accurate numerical methods with minimal computational effort, flexible to solve different problems, easy to maintain and reliable. To construct a numerical method for solving PDEs we need to consider how to represent our solution by an approximate solution, together with the main properties of the PDE to be solved. We need ways to generate a system of algebraic equations from the well-posed PDE and incorporate initial and boundary conditions. Basically, to solve the system while minimizing unavoidable errors that are introduced in the process. Considering the above mentioned one-dimensional conservation law

$$\phi_t + f(\phi)_x = 0 \quad (1.47)$$

We are going to discuss basic ideas and the advantages and disadvantages of different classical methods.

The **finite difference** method (FDM) consists of representing the computational domain by a set of collocated points. The solution is represented locally as a polynomial

$$\phi(x, t) = \sum_{l=0}^2 a_l(t)(x - x^k)^l \quad f(x, t) = \sum_{l=0}^2 b_l(t)(x - x^k)^l \quad (1.48)$$

The PDE is satisfied in a point-wise manner

$$\frac{\partial \phi(x^k, t)}{\partial t} + \frac{f(x^{k+1}, t) - f(x^{k-1}, t)}{h^k + h^{k+1}} = 0 \quad (1.49)$$

Local smoothness requirement pose a problem for solving complex geometries, internal discontinuities and overall grid structure. Finite difference methods are simple to understand, straightforward to implement on structured meshes, high-order accurate, they allow explicit integration in time and they have an extensive body of theoretical and practical work since the 60s. The main disadvantage is their implementation on complex geometries, non-suitability for discontinuous problems and require grid smoothness.

On the other hand, **finite volume** methods (FVM) discretizes the domain with a set of non-overlapping cells, where the solution is represented locally as a cell average

$$\bar{\phi}(x^k, t) = \frac{1}{h^k} \int_{\Omega^k} \phi(x, t) dx \quad (1.50)$$

The PDE is satisfied on conservation form

$$h^k \frac{\partial \bar{\phi}^k}{\partial t} + f(x^{k+1/2}, t) - f(x^{k-1/2}, t) = 0 \quad (1.51)$$

A flux function needs to be reconstructed on cells interfaces

$$f(x^{k+1/2}) = F(\phi^k, \phi^{k+1}) \quad (1.52)$$

Finite volume methods are robust, support complex geometries, are well suited for hyperbolic problems, local, explicit in time, locally conservative (due to telescopic property) and an extensive theoretical background exists since the 70s. Their main problems are the inability to achieve high-order accuracy on general grids and grid smoothness is required.

Another formulation, known as **finite element** method (FEM), consists in discretizing the domain by non-overlapping elements where the solution is represented globally with piecewise continuous polynomials.

$$\phi(x) = \sum_{k=1}^K \phi(x_k, t) N^k(x) \quad (1.53)$$

The PDE is satisfied in a global manner

$$\int_{\Omega_h} (\phi_t + f_x) N^j(x) dx = 0 \quad (1.54)$$

The semi-discrete scheme is implicit by construction and reduces overall efficiency for explicit time-integration. Finite element methods are robust, support unstructured meshes, are high-order, well-suited for elliptic problems (due to the global statement) and extensive theoretical framework exists since the 70s. Their main disadvantages are that they are not well suited for hyperbolic problems (due to directionality) and they are implicit in time (reducing overall efficiency).

An old methodology, which is currently being used successfully, is the so called Discontinuous Galerkin Methods (DGM), and the more advanced $P_N P_M$ methods [4]. This type of methods represent a combination of FEM and FVM that take advantage of the local statement and geometrical flexibility of FVM, redefining the cell averaged nature by the local high-order formulation of FEM. Briefly, the computational domain is subdivided into non-overlapping elements as in FVM and FEM. The global solution is represented using local high-order polynomials similar to FEM. Elements are then connected with numerical fluxes at elements interfaces as in FVM. DGM are arbitrary high-order schemes, locally conservative, flexible, explicit in time, locally adaptive (hp -refinement) and well-suited for hyperbolic problems. The main disadvantage is its higher computational cost and relative lack of theoretical background compared with the other methods.

	Complex geometries	High-order accuracy and hp -adaptivity	Explicit semi-discrete form	Conservation laws	Elliptic problems
FDM	✗	✓	✓	✓	✓
FVM	✓	✗	✓	✓	(✓)
FEM	✓	✓	✗	(✓)	✓
DG-FEM	✓	✓	✓	✓	(✓)

Figure 1.3: Numerical methods comparison.

Among the above mentioned methodologies, we restrict ourselves to the FVM. The reason of this choice is based on the robustness and ability to deal with hyperbolic problems in complex geometries and unstructured meshes. Since high-order reconstructions for FV unstructured meshes are still an open issue, we will focus on low-order schemes (first and second-order). This choice is strength by the fact that, despite the use of high-order schemes, in the presence of shocks the order of accuracy always reduces to one for unsteady cases. On the other hand, low-order schemes suffer from numerical viscosity and dispersion errors. We will evaluate these issues in the next chapters.

As mentioned before, in the FVM framework the computational domain is divided in a set of non-overlapping elements, or control volumes. The global solution is represented locally with the cell averages of the different variables. A general face can be defined by its unitary normal vector and the two adjacent cells. Hence, the flux through a normal face is defined as

$$F_f = F(\phi_O, \phi_P) \quad (1.55)$$

where ϕ_O and ϕ_P are the values of ϕ in the adjacent cells and the unitary normal vector going from cell O to cell P . High-order reconstructions may use also information from more cells

$$F_f = F(\phi_O, \phi_P, \phi'_O, \phi'_P) \quad (1.56)$$

Finally, the PDE is satisfied in conservation form

$$V_i \frac{\partial \phi}{\partial t} + \sum_{f=1}^{N_f^i} \mathbf{F}_f \cdot \mathbf{n} A_f \quad (1.57)$$

where V_i is the volume of the cell, \mathbf{n} is the face unitary normal vector, A_f is the face surface and N_f^i is the total number of faces that form the i th cell.

1.5 Objectives of the thesis

At this point compressible flows have been defined, several fields of applications have been mentioned, and the equations that describe their motion have been derived from physical principles, i.e. the NS equations. The physical and mathematical properties of the NS equations applied to compressible flows have been presented and a simple analytical problem has been solved in order to consolidate the aforementioned aspects of the phenomenology. From now on, the numerical resolution of the NS equations is tackled with the aim of solving real world problems involving compressible fluids, which usually consists of **discontinuous turbulent flows**. They can be found in several fields such as aerodynamics, turbines, aircraft engines design and more. In transonic regimes and beyond, this is when the speed velocity achieves sonic conditions, discontinuities in form of shock waves may appear within the flow, interacting with structural elements and other flow structures such as boundary layers and turbulent vortices. These interactions affect in turn the performance of the studied object. Therefore, the objective of this thesis is to provide the numerical tools required to investigate such phenomena in order to be able to quantify their effects on real applications and predict their performance.

1.6 Outline of the thesis

First, the finite volume techniques required to numerically solve the NS equations in a compressible framework are identified in chapter 2, where the most common numerical approaches are presented and a unique **hybrid numerical flux** model is developed in order to meet the requirements that will allow us to achieve our goals (turbulent compressible flows from subsonic to supersonic). After that, **boundary conditions** for turbulent compressible simulations are presented in chapter 3. In chapter 4 the **turbulence modeling** of compressible flows is faced and the different approaches that can be found in the literature are evaluated and tested. Special emphasis is put on shock-boundary layer interactions. With all that, we will have all the tools required for solving compressible aerodynamics in any compressible regimen. Finally, in chapter 5 the formulation for **multi-component** gases is presented. The hybrid numerical scheme is upgraded in order to solve mixtures of gases and some tests are performed. By adding the multi-component formulation we end up with a numerical method capable of solving a wide range of real applications ranging from subsonic, transonic and supersonic aerodynamics to supersonic mixtures in civil aircraft, engines and turbomachinery. Final **conclusions** and further work is presented in chapter 6.

References

- [1] J. Randall and Leveque. *Finite Volume Methods for Hyperbolic Problems*. Cambridge University Press, 2002.
- [2] A. Liñán Martínez, M. Rodríguez Fernández, and F J. Higuera Antón. *Mecánica de Fluidos*. Madrid, Escuela Técnica Superior de Ingeniería Aeronáutica, 2005.
- [3] E F. Toro. *Riemann Solvers and Numerical Methods for Fluid Dynamics*. New York: Springer, 2009.
- [4] Lei Shi, Z. J. Wang, Song Fu, and Laiping Shang. A $P_N P_M$ -CPR Method for Navier Stokes Equations. *50th AIAA Aerosp. Sci. Meet. Exhib.*, 2012.

A hybrid numerical flux for discontinuous turbulent compressible flows.

2.1 Introduction

In this chapter, the methodology for the discretization of the NS equations using FVM on unstructured meshes is presented. First, numerical methods for turbulent compressible flows in the presence of shock waves are reviewed. As we will see, traditional methods cannot be used at all compressible regimes. Some of them work well for subsonic flows, but fail at transonic and supersonic speeds. Some others work in all regimes when solving the Reynolds-averaged Navier Stokes equations (RANS), but fail with direct numerical simulations (DNS) and large-eddy simulations (LES). With the objective of building a numerical method that is suitable for any kind of compressible flow, independently of the turbulent model used, a new **hybrid numerical scheme** is developed. The new scheme is carefully tested in a wide range of cases in order to evaluate its properties and performance.

2.2 State of the Art

The reference physical model consists of the compressible NS equations for a calorically perfect gas, here written in semi-discretized form in a volume V_c whose surfaces are A_f :

$$\frac{\partial}{\partial t} \phi_i + \frac{1}{V_c} \sum_f f(\phi_f) A_f = 0 \quad (2.1)$$

where ϕ is a vector containing the conserved variables.

$$\phi = \begin{pmatrix} \rho \\ \rho \mathbf{u} \\ E \end{pmatrix} \quad (2.2)$$

and the flux-function is also a vector

$$f(\phi) = \begin{pmatrix} \rho \mathbf{u} \\ \rho \mathbf{u} \mathbf{u} + p \mathbf{n} \\ (E + p) \mathbf{u} \cdot \mathbf{n} \end{pmatrix} - \begin{pmatrix} 0 \\ \boldsymbol{\tau} \cdot \mathbf{n} \\ (\mathbf{u} \cdot \boldsymbol{\tau}) \cdot \mathbf{n} - \mathbf{q} \cdot \mathbf{n} \end{pmatrix} \quad (2.3)$$

The numerical scheme will determine the form in which ϕ_f is computed and, as we will see, this aspect is crucial in the numerical simulation of compressible flows.

Numerical simulation of high-speed flows has a long history, dating back to the beginning of the computer era [1–3]. Several textbooks on numerical methods have appeared over the years [4–7]. Important advancements have been made, but computational gasdynamics has not yet converged to an optimal computational strategy. The purpose of this section is to check the status of the discipline and select the best candidates for our numerical scheme among the enormous amount of material produced over the years, as illustrated by a recent comparative study [8].

For this thesis purposes, we limit ourselves to analyzing the family of FVM schemes that are frequently used, especially in the academic community, for DNS and LES of compressible turbulent flows. Resolving the wide range of scales present in these flows requires numerical schemes that must be accurate, robust, and efficient in terms of CPU requirements.

Neglecting molecular diffusion effects in 2.3 leads to the Euler equations, which only incorporate the influence of macroscopic convection and molecular collisional effects due to pressure forces. Some useful properties for the development of numerical methods are briefly recalled here. First, the system of Euler equations can be cast in characteristic form. This means that projection of the equations in any spatial direction gives rise to a system of coupled wave-like equations used as a prototype for the development of numerical methods for hyperbolic equations, as it was already mentioned in the previous chapter. Second, the Euler equations have the obvious property (as is clear from their integral form) that the integrals of ρ , $\rho \mathbf{u}$, E over an arbitrary control volume can only vary because of flux through the boundaries. Under the assumption of smooth flow, a balance equation in a finite volume V_c for the kinetic energy $\rho \mathbf{u} \cdot \mathbf{u}/2$ can be derived combining the continuity and momentum equations.

$$\frac{\partial}{\partial t} \int_{V_c} \rho \mathbf{u} \cdot \mathbf{u} / 2 dV = - \int_{\partial V} (\rho \mathbf{u} \cdot \mathbf{u} / 2 + p) \mathbf{u} \cdot \mathbf{n} dS + \int_{V_c} p \nabla \cdot \mathbf{u} dV \quad (2.4)$$

Equation 2.4 shows that the total kinetic energy only varies because of momentum flux through the boundary and volumetric work of pressure forces (which is zero for incompressible flow). Additionally, the inviscid terms do not cause any net variation. This property has inspired numerical schemes based on the attempt to enforce **kinetic energy preservation** in the discrete sense. Other approaches based on entropy functions can be considered, but they are out of our scope.

To summarize, high-speed flows typically feature regions where the flow is smooth, and the governing equations in their differential form hold, interspersed by extremely thin regions, where the flow properties vary abruptly. A possible exception is the case of flows in which shocklets embedded in turbulent flow occur, associated with velocity fluctuations of the order of the sound speed. Apparently, even when this happens, their frequency and strength are not such to severely threaten the robustness and accuracy of numerical algorithms. Furthermore, the shocklets thickness is found to scale with the Kolmogorov length, rather than the mean-free path [9], making their resolution possible in DNS. Therefore, it is not surprising that numerical methods for high-speed flows have specialized into two classes, one capable of dealing with smooth flows and the other with shock waves, each with quite different properties. Indeed, it is known that standard discretizations used for smooth flows cause (potentially dangerous) Gibbs **oscillations** in the presence of shock jumps, whereas typical methods used to regularize shock calculations exhibit excessive **numerical viscosity**.

2.2.1 Shock-capturing schemes

These schemes can capture shock waves while being stable. As mentioned before, they suffer from excessive artificial diffusion. This effect can be alleviated constructing high-order approximations, which is not a suitable solution for unstructured grids. Furthermore, as numerical dissipation is reduced, Gibbs oscillation phenomena appear. Therefore, the initial problem is not solved and additional viscosity has to be added.

Upwind schemes

The upwinding approach, commonly followed in the gasdynamics community, is based on the idea that solutions of the Euler equations propagate along characteristics, and therefore a stable numerical method should also propagate its information in the same characteristic direction.

In the FVM framework, upwinding is usually achieved through the flux difference splitting, or **Godunov** approach. A suitable reconstruction operator is used to determine approximate left and right states at the cell interface, and solving the Riemann problem (like in the shock tube example in chapter 1). The interface flux is replaced with the numerical flux resulting from an exact (or approximate) Riemann solver [7, 10]. The extension to a higher order of accuracy is achieved by replacing piece-wise constant reconstructions with piece-wise polynomial reconstructions [11].

Upwinding has the main effect of damping the Fourier modes with the highest supported wave numbers, with a subsequent stabilizing effect on the numerical solution. High-order upwind schemes have often been used for DNS of shock-free compressible turbulence with a good degree of success. However, the numerical dissipation introduced by upwinding can be harmful for LES, for which proper resolution of marginally resolved wave numbers is crucial, as it may hamper the effect of subgrid-scale models. This is not the case of RANS simulations, where this kind of schemes have been the most successful.

ENO and WENO schemes

Classical upwind schemes were found to suffer from loss of accuracy at both smooth and nonsmooth extrema, which stimulated researchers to pursue alternatives for constructing uniformly high-order accurate shock-capturing schemes. The successful family of essentially nonoscillatory (ENO) schemes [12] is based on the idea of determining the numerical flux from a high-order reconstruction over an adaptive stencil that is selected to avoid as much interpolation across discontinuities as possible, thus minimizing Gibbs oscillations.

The type of the weighted essentially nonoscillatory (WENO) schemes, first introduced by Liu et al. [13], and generalized and improved by Jiang & Shu [14], is based on the idea of constructing a high-order numerical flux from a convex linear combination of lower-order polynomial reconstructions over a set of staggered stencils. Their weights are selected to achieve maximum formal order of accuracy in smooth regions. Nearly zero weight is assigned to reconstruction on stencils crossed by discontinuities.

2.2.2 Energy-consistent schemes

These schemes do not introduce artificial viscosity, but are unstable in the presence of shock-waves.

Central derivative approximations have been widely used in the literature, especially for wave propagation problems in which nonlinearities are weak [15]. However, it is known that application of standard central discretizations to high-Reynolds

number turbulent flows typically leads to numerical instability, owing to the accumulation of the aliasing errors resulting from discrete evaluation of the nonlinear convective terms [16]. Such deficiency can also be traced back to the failure to discretely preserve quadratic invariants associated with the conservation equations [17]. Although finite viscosity may help to stabilize calculations, it is usually safer to revert to alternative discretization techniques capable of ensuring stability in the inviscid limit.

Several attempts have been made to design nonlinearly stable numerical schemes by replicating the energy-preservation properties of the governing equations in the discrete sense. Most efforts are based on the idea of **splitting** the convective derivatives, i.e.

$$\frac{\partial \rho u_i \phi}{\partial x_i} = \frac{1}{2} \frac{\partial \rho u_i \phi}{\partial x_i} + \frac{1}{2} \phi \frac{\partial \rho u_i}{\partial x_i} + \frac{1}{2} \rho u_i \frac{\partial \phi}{\partial x_i} \quad (2.5)$$

Discretization of the mass and momentum equations in the split form implies kinetic energy preservation at the semidiscrete level [18], provided the difference operators satisfy the summation by parts property [19]. Ducros et al. [20] showed that the split convective forms give rise to locally conservative schemes, when the derivative operators are discretized with explicit central formulas.

Stabilization

Filtering the computed solution is a commonly used practice to cure nonlinear instabilities of central schemes, while retaining high-order accuracy [21, 22]. Stabilization of numerical schemes can also be achieved by enforcing, at the discrete level, the conservation properties associated with entropy. Tadmor [23] developed a second-order FV, locally conservative discretization of the Euler equations. An alternative strategy to ensure entropy stability was proposed by Gerritsen & Olsson [24], who split the flux vector into conservative and nonconservative parts. Honein & Moin [18] developed entropy-consistent schemes by applying the convective splitting given in equation 2.5 to the Euler equations, upon replacement of the total energy equation with the entropy equation. This approach effectively preserves the integrals of ρs and ρs^2 . Those authors also showed that the internal and total energy equations can be rearranged in such a way that the split convective form of the entropy equation automatically follows. This is particularly advantageous, as the total energy equation is typically used in compressible flow codes, especially for shock calculations.

2.2.3 Shock-capturing techniques

Energy-consistent schemes presented in the previous section suffer from spurious Gibbs oscillations near shock jumps, which may lead to nonlinear instabilities. The

onset of oscillations can be avoided (or at least limited) by following two strategies. The first one, the shock-fitting approach, treats shock waves separately from the rest of the flow as genuine discontinuities. Their dynamics are governed by their own algebraic equations. The Rankine-Hugoniot relations are used as a set of nonlinear boundary conditions to relate the states on the two sides of the discontinuity [25]. The second approach, the shock-capturing, uses the same discretization scheme at all points and achieves regularization through the addition of numerical dissipation, which inhibits the onset of Gibbs oscillations. Although the former approach often guarantees more accurate representations of shocked flows [26], it is only feasible in cases in which the shock topology is extremely simple and no shock waves are formed during the calculation. In this review, we discuss only the shock-capturing approach.

Artificial Viscosity Methods

The basic idea of artificial viscosity methods is to explicitly introduce the amount of numerical dissipation needed to stabilize shock computations through the addition of diffusive terms that adaptively adjust to the local regularity of the solution. Some examples can be found in [3, 27].

Hybrid Schemes

This type of methods are based on the idea of endowing a baseline non-dissipative scheme with shock-capturing capability through local replacement with a classical shock-capturing scheme or through the controlled addition of the dissipative part of a shock-capturing scheme, which is made to act as a nonlinear filter. A key role in this class of schemes is played by shock sensors that must be defined in such a way that numerical dissipation is effectively confined in shocked regions, so that it does not pollute smooth parts of the flow field.

Shock-Capturing Through Subgrid-Scale Models

Methods of this type are based on the attempt to regularize weak solutions of the conservation equations through the addition of subgrid-scale models that drain energy from the unresolved scales of motion, in analogy to what is done in LES of smooth flows.

About shock-capturing methods

A major flaw of shock-capturing schemes, often disregarded, is the reduction of accuracy near shocks. Indeed, even (nominally) uniformly high-order schemes yield

first-order accurate solutions downstream of moving shocks, mainly because shocks have zero thickness, and therefore their location is only known to $O(h)$ on a finite grid. The loss of accuracy was highlighted in model scalar shock-sound interaction problems [28], and it is likely to be the cause of the slow convergence of apparently simple shock/turbulence interaction calculations [29]. Shock-capturing schemes applied to systems of conservation laws also suffer from spurious post-shock oscillations, especially in the case of slowly moving shocks [30], which may prevent the accurate prediction of shock/sound and shock/turbulence interactions, as observed by Johnsen et al. [26]. These pathologies are apparently unavoidable, unless one reverts to special techniques, such as subcell resolution [31] or even to shock-fitting.

FVM provide greater flexibility than FDM in dealing with complex geometries. As locally conservative, FV schemes can be easily designed for both structured and unstructured meshes. The FV framework also allows the design of one-step methods in time (as opposed to multistage Runge-Kutta time integration commonly used for FDM). Furthermore, it appears that a FV formulation, with the use of suitable positivity-preserving approximate Riemann solvers, is necessary in some instances, such as the computation of compressible multicomponent flows, to avoid oscillations in the presence of material interfaces [32]. With regard to FVM for structured meshes, it is known that straightforward dimensional splitting gives rise to second-order errors (regardless of the accuracy of the underlying reconstructions), unless computationally expensive quadratures are used to evaluate the flux integrals transverse to the direction being reconstructed. High-order accurate, quadrature-based FV schemes have been developed [33, 34]. However, as observed by Ducros et al. [20] the splitting error is usually small, and line-wise application of 1D reconstructions is quite successful in practice, yielding an accurate representation of smooth flow features and good shock-capturing properties. Unstructured meshes mandate the use of both high-order flux quadratures at cell interfaces and genuinely multidimensional reconstructions [35], thus making high-order FV schemes highly expensive. An important step in the direction of improving the computational efficiency of high-order FV schemes was accomplished by Dumbser et al. [36], who succeeded in designing one-step nonoscillatory FV schemes for unstructured tetrahedral meshes with arbitrary order of accuracy, without the need of quadratures. Their strategy exploits a characteristic WENO reconstruction yielding the whole polynomial information in each cell and a Cauchy-Kovalewski procedure to provide a space-time Taylor series for the conserved quantities and the physical fluxes. This information is used to construct highly accurate upwind numerical fluxes, which are subsequently integrated analytically in space and time. A comprehensive review of modern FVM is given by Toro [7].

Jameson [37] and Subbareddy & Candler [38] have developed second-order FVM suitable for unstructured meshes that discretely preserve kinetic energy. In particu-

lar, in the latter study, fully discrete energy conservation was obtained through a density weighted Crank-Nicholson-like time integration, and shock-capturing was incorporated in the method in the form of a TVD filter controlled by the Ducros sensor. The development of energy and entropy-consistent methods for unstructured meshes is dealt with in the monographic review by Perot [39].

2.2.4 Open issues

Some open issues remain. First, one must be aware that the global order of accuracy of shock-capturing schemes in unsteady problems is always reduced to unity, and shock-capturing is the cause of spurious oscillations, especially downstream of slowly moving shocks. These limitations, related to the misrepresentation of discontinuities on a mesh with finite spacing, can only be overcome by some form of shock-fitting. A detailed study of the effect of shock-capturing oscillations on the prediction of shock/sound and shock/turbulence interactions is still pending and would be highly desirable. Second, even though hybrid schemes are frequently used, a systematic quantitative analysis of the coupling between shock-capturing and non dissipative schemes has not been carried out yet. Third, a comparative efficiency analysis of numerical algorithms (in terms of CPU cost for a given error tolerance) for problems involving shock waves is not available at present, and cost figures are seldom reported in computational studies. Fourth, it appears that efficient, low-dissipative methods suitable for compressible turbulence simulation on unstructured meshes are missing in the literature, one notable exception being the recent work of Subbareddy & Candler [38] (however, limited to second-order accuracy). Further efforts are needed before computational gas dynamics can reach a fully mature stage and cope with the growing demand for DNS and LES of high-speed turbulent flows for configurations of technological relevance. To summarize:

1. Methods designed for smooth flows and shocked flows have quite different features. The former type is driven by the intent of achieving nonlinear stability without introducing numerical dissipation. The latter type attempts to stabilize shock computations through the addition of some (possibly not excessive) numerical dissipation.
2. Robust and accurate methods for smooth flows can be developed with the guidance of physical conservation principles of kinetic energy and entropy.
3. Discretization of the split convective form of the equations leads to methods that are nonlinearly stable for smooth flows, also in the infinite Reynolds number limit.
4. Shock-capturing methods are always globally first-order accurate for unsteady problems, as the shock location is unknown to $O(h)$, where h is the mesh spacing.
5. WENO schemes are the currently dominant type of shock-capturing methods, as they are at the same time accurate and robust.

6. WENO schemes are too dissipative for DNS and LES and should be preferably used in hybrid form, i.e. in conjunction with low-dissipative algorithms for smooth parts of the flow.

7. A key role for the success of hybrid methods is played by shock sensors that should be able to localize the necessary amount of numerical dissipation around shock waves.

8. Nonlinear artificial viscosity methods constitute an attractive alternative to hybrid-WENO schemes.

The present thesis tackles the aforementioned lack on efficient, low-dissipative methods suitable for compressible turbulence simulation on unstructured meshes. The following sections and chapters are intended to develop such a kind of numerical method to advance in the knowledge of computational gas dynamics for compressible turbulent flows.

2.3 Development of a hybrid numerical scheme

Ideal numerical methods for highly compressible flows should be accurate and free from numerical dissipation in smooth parts of the flow, and at the same time they must robustly capture shock waves without significant Gibbs ringing, which may lead to nonlinear instabilities. Adapting to these conflicting goals leads to the design of strongly nonlinear numerical schemes that depend on the geometrical properties of the solution. With low-dissipation methods for smooth flows, numerical stability can be based on physical conservation principles for kinetic energy and/or entropy. Shock-capturing requires the addition of artificial dissipation, in more or less explicit form, as a surrogate for physical viscosity, to obtain nonoscillatory transitions.

In the previous section different methods used for the numerical simulation of turbulent compressible flows in the presence of shocks have been presented. The virtues and flaws of the different approaches have been stated. At this point all the required information to chose a method to achieve the proposed objectives is gathered. We focus only on low-order FVM for unstructured grids in order to solve turbulent compressible flows, by means of DNS or any turbulent modeling (LES or RANS). Therefore, upwind-like schemes are discarded because they are too dissipative for DNS and LES. We chose, hence, the class of numerical schemes that are kinetic energy preserving (central approximations) suitable for DNS and LES. In order to stabilize the method in the presence of shocks, an upwind scheme will be used only at shock-waves. The abrupt changes in the flow are identified by means of a discontinuity sensor. The resulting scheme will be able to deal with any kind of compressible flow (continuous or discontinuous, laminar or turbulent) and will admit any type of turbulence modeling.

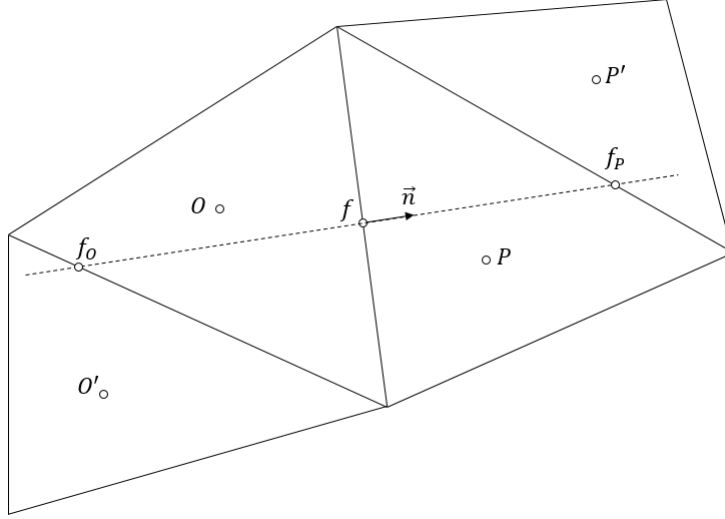


Figure 2.1: Finite control volume diagram.

As a first step, we distinguish between discretized inviscid and viscous fluxes (see equation 2.3).

$$F(\phi_f) = F^{inv}(\phi_f) + F^{visc}(\phi_f) \quad (2.6)$$

Inviscid fluxes are computed in most of the fluid domain using a Kinetic Energy Preserving scheme as a basis. When the discontinuity sensor recognizes a discontinuity within the flow, artificial diffusion is added in a very selective way by means of an upwind method. This approach minimizes the amount of numerical viscosity while having a stable scheme provided a fine tune of the discontinuity sensor, Φ .

$$F^{inv}(\phi_f) = (1 - \Phi)F^{KEP}(\phi_f) + \Phi F^{UDS}(\phi_f) \quad (2.7)$$

Viscous fluxes are treated in section 2.3.4.

2.3.1 Kinetic energy preserving

Following section 2.2, the discretization of the convective terms in **divergence form** (DIV) leads to unstable schemes.

$$F(\phi_f) = \frac{1}{2}(F(\phi_P) + F(\phi_O)) \quad (2.8)$$

Alternative formulations are based on the splitting of the convective term of the momentum equation in conservative and non-conservative form (see equation 2.5). Ducros et al. [20] showed that different split convective forms of equation 2.5 give rise to locally conservative schemes, when the derivative operators are discretized with explicit central formulas. This **splitting** form (KEP) can be written as,

$$\phi_f = \frac{1}{2}(\phi_P + \phi_O) \quad (2.9)$$

Figure 2.4 shows the comparison between DIV and KEP formulation on the inviscid Taylor Green vortex problem. When KEP form is used, the total amount of kinetic energy is preserved throughout the simulation. On the other hand, the use of DIV form results in an error accumulation that rapidly blows up. This result confirms what has been observed by other authors. Therefore, the splitting approach is preferred over the divergence formulation to use as a basis for our hybrid scheme for the discretization of the convective terms of the Navier Stokes equations.

2.3.2 Numerical diffusion

The artificial diffusion required to make the numerical scheme stable in presence of flow discontinuities is introduced by means of an upwind-like scheme. These methods are based on the Godunov's method, which solves the Riemann problem at each cell interface. Consider ϕ_i^n the approximation to the cell average of $\phi(\mathbf{x}, t_n)$ over the cell V_c .

$$\phi_i^n \approx \frac{1}{V_c} \int_{V_c} \phi(\mathbf{x}, t_n) dV \quad (2.10)$$

The idea is to use the piecewise constant function defined by these cell values as initial data $\hat{\phi}^n(\mathbf{x}, t_n)$ for the conservation laws. Solving over time Δt with this data gives a function $\hat{\phi}^n(\mathbf{x}, t_{n+1})$ which is then averaged over each cell to obtain

$$\phi_i^{n+1} = \frac{1}{V_c} \int_{V_c} \hat{\phi}^n(\mathbf{x}, t_{n+1}) dV \quad (2.11)$$

If the time step Δt is sufficiently small, the exact solution $\hat{\phi}^n(\mathbf{x}, t)$ can be determined by piecing together the solutions to the Riemann problem arising from each cell interface.

We use equation 2.1 to update ϕ^{n+1} with $F(\phi_f) = F(\phi^*(\phi_P, \phi_O))$ where ϕ_P and ϕ_O are the averaged values of ϕ at each side of the face f (see figure 2.1). $\phi^*(\phi_P, \phi_O)$ denotes the solution to the Riemann problem between ϕ_P and ϕ_O .

In order to avoid the interaction of waves from neighboring Riemann problems the time step is required to be

$$\frac{\lambda_{max}\Delta t}{\Delta x} \leq 1 \quad (2.12)$$

where λ_{max} is the maximum absolute value for the characteristic speeds and $\Delta x = V_c^{1/3}$.

The Riemann Problem

The Riemann problem consists of a hyperbolic equation with an initial piecewise constant data represented by a single jump discontinuity

$$\phi = \begin{cases} \phi_l & \text{if } x < 0 \\ \phi_r & \text{if } x > 0 \end{cases} \quad (2.13)$$

Notice that the shock tube problem is a Riemann problem. We expect this discontinuity to propagate along the characteristic curves. The solution to the Riemann problem consists of the discontinuity $\phi_r - \phi_l$ propagating at the characteristic speeds.

$$\phi_l = \sum_{p=1}^m w_l^p r^p \quad \phi_r = \sum_{p=1}^m w_r^p r^p \quad (2.14)$$

The solution to the Riemann problem is based on the sum of the waves propagating to the left from the right region, plus the waves traveling towards the right from the left region.

$$\phi(x, t) = \sum_{p: \lambda^p < x/t} w_r^p r^p + \sum_{p: \lambda^p > x/t} w_l^p r^p \quad (2.15)$$

An important fact is that the jump in ϕ is an eigenvector of the matrix A , being a scalar multiple of r^p ,

$$(w_r^p - w_l^p)r^p = \alpha^p r^p \quad (2.16)$$

This condition is called the Rankine-Hugoniot jump condition. Therefore, solving the Riemann problem consists of taking the initial data and decomposing the jump $\phi_r - \phi_l$ into eigenvectors of A

$$\phi_r - \phi_l = \sum_{p=1}^m \alpha^p r^p = \sum_{p=1}^m W^p \quad (2.17)$$

what in turn requires solving the linear system of equations

$$R\alpha = \phi_r - \phi_l \quad (2.18)$$

for the vector α . Finally, one can derive the expression for the flux function

$$F(\phi_f) = A\phi_O + \sum_{p=1}^m (\lambda^p)^- \alpha^p r^p \quad (2.19)$$

or

$$F(\phi_f) = A\phi_P - \sum_{p=1}^m (\lambda^p)^+ \alpha^p r^p \quad (2.20)$$

Approximate Riemann Solvers

The process of solving the Riemann problem is often quite expensive, even though in the end we use very little information from this solution in defining the flux. It is often true that is not necessary to compute the exact solution to the Riemann problem in order to obtain good results.

Approximate Riemann solvers can be applied much more cheaply than the exact Riemann solver, giving still good results. For given data ϕ_P and ϕ_O , an approximate Riemann solution might define a function that approximates the true similarity solution to the Riemann problem. This function will consist of some set of M_w waves W_f^p propagating at some speeds λ_f^p with

$$\phi_P - \phi_O = \sum_{p=1}^{M_w} W_f^p \quad (2.21)$$

A natural approach to define an approximate Riemann solution is to replace the nonlinear problem by some linearized problem defined locally at each cell interface

$$\phi_t + A_f \phi_x = 0 \quad (2.22)$$

The matrix A_f is chosen to be some approximation to $F'(\phi)$ valid in the neighborhood of the data ϕ_P and ϕ_O . The matrix A_f should be diagonalizable with real eigenvalues. Since this is a linear problem, the Riemann problem can be solved more easily than the original nonlinear problem,

$$\phi_P - \phi_O = \sum_{p=1}^m W_f^p \quad (2.23)$$

where $W_f^p = \alpha_f^p r_f^p$, being r_f^p the eigenvectors of A_f and α_f^p some coefficients.

Roe Solver for the Euler Equations

Consider the Euler equations,

$$\frac{\partial}{\partial t} \begin{pmatrix} \rho \\ \rho \mathbf{u} \\ E \end{pmatrix} + \nabla \cdot \begin{pmatrix} \rho \mathbf{u} \\ \rho \mathbf{u} \mathbf{u} + p \mathbf{n} \\ (E + p) \mathbf{u} \mathbf{n} \end{pmatrix} = 0 \quad (2.24)$$

The approximated Jacobian matrix for a general face, A_f , is

$$\begin{bmatrix} 0 & n_x & n_y & n_z & 0 \\ (\gamma - 1)e_k n_x - uu_n & u_n - (\gamma - 2)un_x & un_y - (\gamma - 1)vn_x & un_z - (\gamma - 1)wn_x & (\gamma - 1)n_x \\ (\gamma - 1)e_k n_y - vu_n & vn_x - (\gamma - 1)un_y & un - (\gamma - 2)vn_y & vn_z - (\gamma - 1)wn_y & (\gamma - 1)n_y \\ (\gamma - 1)e_k n_z - wu_n & wn_x - (\gamma - 1)un_z & wn_y - (\gamma - 1)vn_z & un - (\gamma - 2)wn_z & (\gamma - 1)n_z \\ ((\gamma - 1)e_k - H)u_n & Hn_x - (\gamma - 1)uu_n & Hn_y - (\gamma - 1)vu_n & Hn_z - (\gamma - 1)wu_n & \gamma u_n \end{bmatrix} \quad (2.25)$$

where $\mathbf{n} = (n_x, n_y, n_z)$ is the face normal vector, $\mathbf{u} = (u, v, w)$ is the velocity vector, $u_n = \mathbf{u} \cdot \mathbf{n}$ is the face normal velocity, $e_k = \frac{1}{2}\mathbf{u} \cdot \mathbf{u}$ is the specific kinetic energy.

The eigenvalues of the Jacobian matrix can be found solving the system ,

$$\det(A - \lambda I) = 0 \quad \rightarrow \quad \lambda = \begin{pmatrix} u_n - a \\ u_n \\ u_n \\ u_n \\ u_n + a \end{pmatrix} \quad (2.26)$$

and the eigenvectors must satisfy $AR = \lambda R$,

$$R = \begin{bmatrix} 1 & 1 & 0 & 0 & 1 \\ u - an_x & u & n_y & -n_z & u + an_x \\ v - an_y & u & -n_x & 0 & v + an_y \\ w - an_z & u & 0 & n_x & w + an_z \\ H - au_n & e_k & un_y - vn_x & wn_x - un_y & H + au_n \end{bmatrix} \quad (2.27)$$

These eigenvectors are not unique, and any linear combination of them can also be used [40].

For the Euler equations, Roe [10] proposed the parameter vector $z = \rho^{-1/2}\phi$, leading to the averages,

$$\begin{aligned} \hat{u} &= \frac{\sqrt{\rho_p} u_p + \sqrt{\rho_O} u_O}{\sqrt{\rho_p} + \sqrt{\rho_O}} \\ \hat{H} &= \frac{\sqrt{\rho_p} H_p + \sqrt{\rho_O} H_O}{\sqrt{\rho_p} + \sqrt{\rho_O}} \\ \hat{a} &= \sqrt{(\gamma - 1) \left(\hat{H} - \frac{1}{2} \hat{u}^2 \right)} \end{aligned} \quad (2.28)$$

However, a simple central approximation of the variables at the face has proved to be also satisfactory. The eigenvalues and eigenvectors of the Roe matrix are then obtained by evaluating equations 2.26 and 2.27 at this averaged state. The coefficients α_f^p in the wave decomposition,

$$\delta = \phi_P - \phi_O = \alpha^1 r^1 + \alpha^2 r^2 + \alpha^3 r^3 + \alpha^4 r^4 + \alpha^5 r^5 \quad (2.29)$$

can be obtained by inverting the matrix of right eigenvectors, which leads to the following formulas:

$$\alpha^1 = \frac{1}{2} \left(\delta_\rho - \alpha^2 - \frac{\delta_{\rho\mathbf{u}} \cdot \mathbf{n} - \delta_\rho u_n}{a} \right) \quad (2.30)$$

$$\alpha^2 = \frac{1}{e_k - H} \left(\delta_E - H_f \delta_\rho - \alpha^3 (u n_y - v n_x) - \alpha^4 (w n_x - u n_z) - (\delta_{\rho\mathbf{u}} \cdot \mathbf{n} - \delta_\rho u_n) u_n \right) \quad (2.31)$$

$$\alpha^3 = \frac{1}{n_x + \epsilon} (\delta_\rho v - \delta_{\rho v} + (\delta_{\rho\mathbf{u}} \cdot \mathbf{n} - \delta_\rho u_n) n_y) \quad (2.32)$$

$$\alpha^4 = \frac{1}{n_x + \epsilon} (\delta_{\rho w} - \delta_\rho w - (\delta_{\rho\mathbf{u}} \cdot \mathbf{n} - \delta_\rho u_n) n_z) \quad (2.33)$$

$$\alpha^5 = \frac{\delta_{\rho\mathbf{u}} \cdot \mathbf{n} - \delta_\rho u_n}{a} + \alpha^1 \quad (2.34)$$

where $\delta_{\rho\mathbf{u}} = (\delta_{\rho u}, \delta_{\rho v}, \delta_{\rho w})$ and ϵ is a small number to avoid division by 0.

Other approximate Riemann solvers have been used over the past decades, e.g. HLL and HLLC among others. These approximate solvers, nevertheless, have not been as satisfactory as the Roe solver. They do not use the full structure of the original Riemann problem, considering only two (HLL) or three (HLLC) waves. Details on these solvers can be found in [41].

Flux limiters

Flux limiters can be used to reduce numerical diffusion of the first-order upwind method. If we attempt to use a Godunov method solely, flux limiters are required because the first-order approach is very diffusive. Nevertheless, when using hybrid methods the upwind scheme is used so selectively that the need of numerical diffusion reduction is not a requirement for the method. It can be useful to increase shock sharpness in coarse meshes.

Flux limiters are based on the concept of total variation diminishing (TVD).

$$F(\phi_f) = F(\phi_f)^{1st} + \frac{1}{2} \sum_{p=1}^m |\lambda_f^p| \left(1 - \frac{\Delta t}{\Delta x} |\lambda_f^p| \right) \Theta(\hat{\lambda}_f^p) r_f^p \quad (2.35)$$

where $\hat{\alpha}_f^p$ is a limited version of α_f^p obtained comparing the wave coefficients of adjacent Riemann problems in the upwind direction.

$$\hat{\alpha}_f^p = \begin{cases} \frac{\alpha_{f_O}^p}{\alpha_f^p} & \text{if } \lambda_f^p > 0 \\ \frac{\alpha_{f_P}^p}{\alpha_f^p} & \text{if } \lambda_f^p < 0 \end{cases} \quad (2.36)$$

and $\Theta(\theta)$ is the flux limiter function. Some functions are,

$$\Theta(\theta) = \begin{cases} \max(0, \min(1, 2\theta), \min(2, \theta)) & \text{SUPERBEE} \\ \max(0, \min(\frac{1+\theta}{2}, 2, 2\theta)) & \text{MCLIMITER} \\ \frac{\theta + |\theta|}{1 + |\theta|} & \text{VANLEER} \end{cases} \quad (2.37)$$

Many more can be found in the literature. This approach increases considerably the computational effort since now we are solving three Riemann problems at each face. The information must then be available for each face. Therefore, it also affects memory performance. Figure 2.2 shows a comparison of the results for the shock tube problem using the upwind scheme with and without flux limiters. As it can be seen, solution is sharper with flux limiters and less control volumes inside discontinuities are found.

2.3.3 Shock capturing

For our hybrid scheme, shock capturing is achieved via a discontinuity sensor. This sensor is required to force the use of the non-dissipative scheme in the regions of turbulent smooth flow, while using the dissipative scheme in the vicinity of shocks. This means that a good sensor must distinguish between turbulent structures and flow discontinuities. To that end, sensors based on the divergence of the velocity vector and the magnitude of the vorticity are preferred. In the framework of this thesis, two different sensors have been used. The first one was proposed by Ducros [42] and has the form

$$\Phi = \frac{(\nabla \cdot \mathbf{u})^2}{(\nabla \cdot \mathbf{u}) + |\nabla \times \mathbf{u}| + \epsilon} \quad (2.38)$$

where ϵ is a small number to prevent division by zero.

An improvement over the Ducros sensor is the Larsson sensor [43], which has the form

$$\Phi = \begin{cases} 0 & \text{if } \Theta \leq 1 \\ 1 & \text{if } \Theta > 1 \end{cases} \quad (2.39)$$

where

$$\Theta = \frac{-\nabla \cdot \mathbf{u}}{\max(L_{ss1}|\nabla \times \mathbf{u}|, L_{ss2}(\frac{a}{\Delta x}))} \quad (2.40)$$

Here a is the speed of sound, $\Delta x = V_c^{1/3}$, and L_{ss1} and L_{ss2} are problem dependent constants. The Larsson sensor has the advantage of being binary, i.e. it can only take the values 1 (shock detected) or 0 (smooth flow). Furthermore, a fine tuning of the two constants allow more precision in the shock capturing than the Ducros sensor, especially in the interaction between shocks and boundary layers.

2.3.4 Discretization of viscous fluxes

Viscous terms are computed using a standard central difference approximation.

$$F^{visc}(\phi_f) = F^{visc}\left(\frac{1}{2}(\phi_P + \phi_O)\right) \quad (2.41)$$

This approach has been successfully used in several works and no problems have been encountered so far.

2.4 Numerical tests

The aim of this section is to test the presented hybrid numerical scheme, evaluating its performance and validating its application in real world problems. Numerical tests are focused on the evaluation of key aspects of the hybrid method and all the parts involved, i.e the KEP scheme, the UDS scheme and the discontinuity sensor.

2.4.1 The Shock Tube Problem

The shock tube problem with air was used to evaluate the shock capturing capability of the method. A $100 \times 5 \times 5$ structured mesh was used. The flow was initialized at the conditions $\rho_l = 8$, $p_l = 10/\gamma$, $u_l = 0$ and $\rho_r = 1$, $p_r = 1/\gamma$, $u_r = 0$. The solution for $t = 0.2$ is presented in figure 2.2. Results show that all the approaches are able to capture discontinuities, although the KEP method is unstable near them. The use of a flux limiter helps to increase shock sharpness. The hybrid approach gives similar results than Godunov's approach.

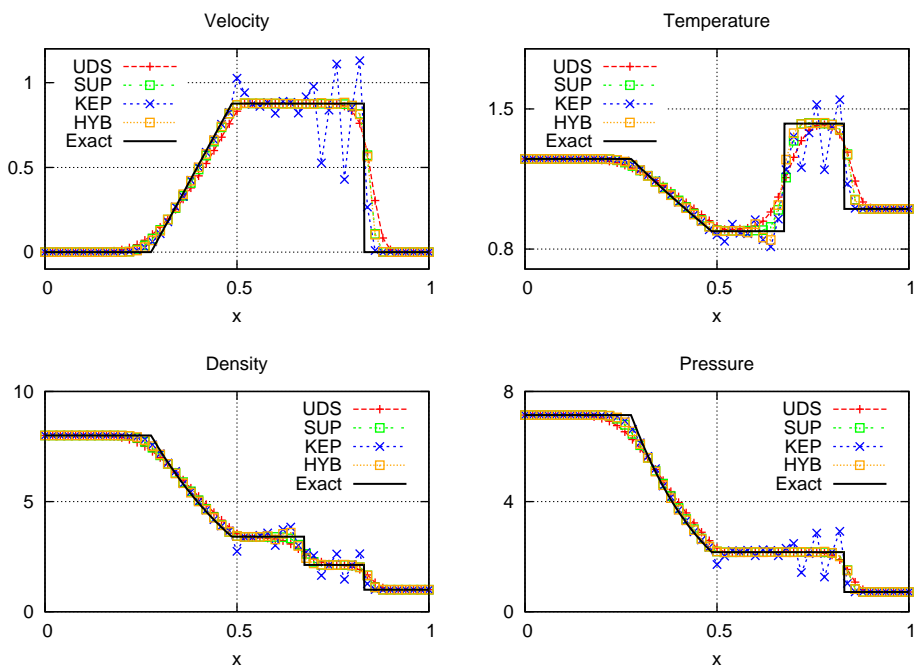


Figure 2.2: Comparison between upwind-like (UDS), kinetic energy preserving (KEP), superbee flux limiter (SUP) and hybrid (HYB) schemes on the shock-tube problem.

2.4.2 Advection of a two-dimensional isentropic vortex

One way to test the numerical dissipation of a given numerical scheme is the advection of an inviscid two-dimensional isentropic vortex. The vortex is placed within a freestream and is advected through a full periodic domain. Some vortex properties, density for example, can be traced in time in order to see whether the numerical scheme is dissipating the vortex or simply advecting it. Since the problem is inviscid any vortex dissipation will be due to the numerical scheme artificial viscosity.

The vortex model used for the simulation is a Lamb-type vortex [44]. This vortex has a finite core. The principal parameters that characterize the vortex are its strength Γ and the radius of its core r_c . The cylindrical velocity distribution of a point located at a distance r from the vortex core center is given by

$$u_\theta = \frac{\Gamma}{2\pi R} \frac{r^2}{r^2 - r_c^2} \quad (2.42)$$

The pressure and density fields induced by this vortex in a uniform freestream can be determined from the radial momentum equation and the constant total enthalpy flow relation, namely:

$$p = p_\infty e^{f(r)} \quad (2.43)$$

$$\rho = \left(\frac{\gamma}{\gamma - 1} \frac{1}{h_\infty - 1/2 u_\theta^2} \right) p \quad (2.44)$$

where

$$h_\infty = \frac{\gamma}{\gamma - 1} \frac{p_\infty}{\rho_\infty} \quad (2.45)$$

$$f(r) = \frac{2D}{E^{1/2}} \left[\tan^{-1} \left(\frac{2r^2 + B}{E^{1/2}} \right) - \frac{\pi}{2} \right] \quad (2.46)$$

with

$$D = 1/2 \left(\frac{\Gamma}{2\pi} \right)^2 \frac{p_\infty}{\rho_\infty} \quad (2.47)$$

$$B = 2r_c^2 - D(\gamma - 1)/\gamma \quad (2.48)$$

$$E = 4r_c^2 - B^2 > 0 \quad (2.49)$$

It is noted here that equations 2.42, 2.43, and 2.44 satisfy the governing equations for steady, inviscid, and adiabatic two-dimensional flows. The vortex disturbance field is then given by

$$\begin{aligned}\Delta u &= -u_\theta \sin\theta \\ \Delta v &= u_\theta \cos\theta \\ \Delta \rho &= \rho - \rho_\infty \\ \Delta p &= p - p_\infty\end{aligned}\tag{2.50}$$

The initial conditions simulating the presence of a vortex in a steady and uniform flow region of some background flow field can be constructed as follows:

$$\begin{aligned}u &= u_b + \Delta u \\ v &= v_b + \Delta v \\ p &= p_b + \Delta p \\ \rho &= \rho_b + \Delta \rho\end{aligned}\tag{2.51}$$

Here, the subindex b denotes some background flow. It is noted here that vortex must be placed in a region in which u_b , v_b , ρ_b and p_b are steady and uniform.

Calculations are started from this initial condition, integrating the flow equations on a fixed grid to follow the convection of this vortex through the computational grid. In these calculations, the reference length is the vortex core radius and the reference flow conditions are the free stream conditions. Time, t , is made dimensionless by freestream velocity and the vortex core radius, e.g. an increment $\Delta t = 1.0$ represents the time required for a particle at freestream velocity to travel one vortex core radius.

In order to evaluate the numerical diffusion of the methods, a study of the advection of a two-dimensional isentropic vortex was performed [44]. The KEP and UDS methods, with and without flux limiter, are compared in a 120×120 structured grid. Periodic boundary conditions are imposed in all directions. A 20×20 computational domain was used, and a vortex with strength $\Gamma = 20$ and $r_c = 5$ was superimposed in a $Ma = 0.536$ freestream.

As it is an inviscid problem, the initial solution is expected to be moved over time within the freestream with no dissipation. That means that any diffusion of the initial vortex is due to the numerical scheme. The initial density profile is compared against the vortex density profile at the three first vortex turnarounds. The results are depicted in figure 2.3. The KEP method preserves the initial solution unchanged over time, while Godunov's approach dissipate the initial vortex over time. The use of flux limiters alleviate this problem, although numerical diffusion still affects the solution quality.

This result is the clear example of why kinetic energy preserving methods must be used when DNS or LES are used on the analysis of turbulent flows. Upwind-based schemes diffuse the turbulent structures affecting the solution. Resort to high-

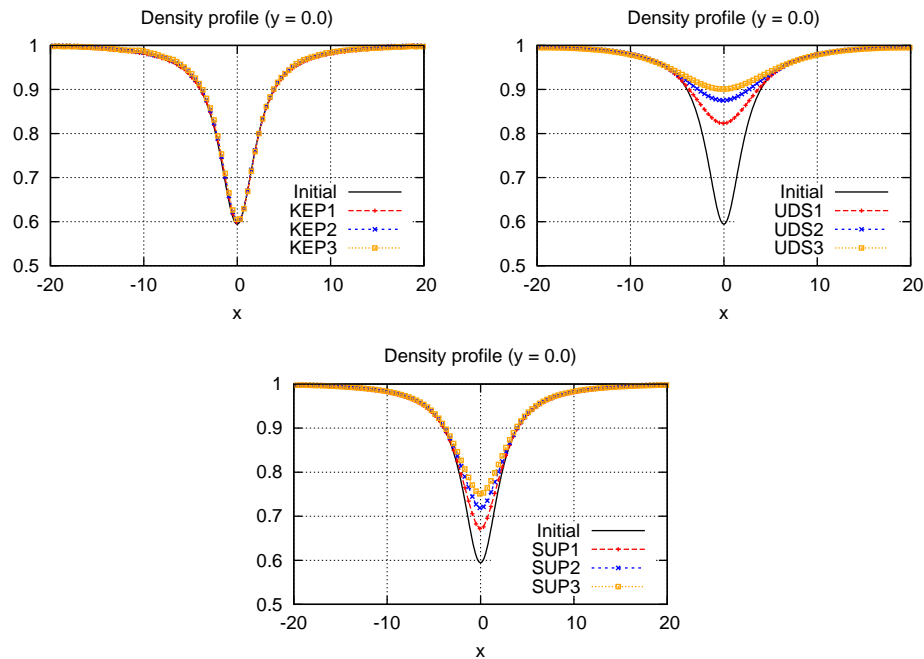


Figure 2.3: Density profile of the vortex at the first three turns for KEP (top left), upwind (UDS, top right) and upwind with the Superbee flux limiter (SUP, bottom).

order schemes (like the use of flux limiters) reduce the amount of numerical viscosity, but not completely. This fact, combined with the reduction of the order of accuracy to one in unsteady shocked-flows, favor the use of low-order energy preserving schemes instead of (very) high-order upwind-like schemes. The advection of a 2D inviscid vortex is a simple test, but the same results can be seen on more complex three-dimensional flows.

2.4.3 Taylor-Green Vortex Problem

The Taylor-Green vortex problem evolves from a resolved initial condition continually stretching and producing ever smaller structures analogous to the cascade of structures found in turbulent flow. If used in a inviscid regimen, such as the Euler equations, there is no lower bound on the length scale of these structures because there is no dissipation other than the provided by the advection scheme used. Therefore, the inviscid Taylor-Green vortex problem can be used to test the level of numerical dissipation of numerical schemes by means of their ability to temporally conserve the mean kinetic energy (or other thermodynamic property). Furthermore, it can be used to evaluate the temporal stability of a numerical method. For the initial conditions, the following dimensionless quantities are used,

$$\begin{aligned} p &= \frac{1}{16\gamma Ma^2} (\cos(2z) + 2(\cos(2x) + \cos(2y))) \\ u &= \sin(x)\cos(y)\cos(z) \\ v &= -\cos(x)\sin(y)\cos(z) \\ w &= 0 \end{aligned} \tag{2.52}$$

with reference density and temperature, $\rho = T = 1$. Some tests were conducted in a 32^3 grid all periodic $2\pi^3$ cubic domain in order to test the numerical stability of the two methods. As it can be seen in figure 2.4 the divergence form is unstable and diverge before 5 time units. On the other hand, the splitting form conserves kinetic energy and is stable.

The diffusive properties of upwind schemes can be clearly seen in this problem. Results shown in figure 2.5 compare the time evolution of the total kinetic energy for the first order upwind scheme, a superbee flux limiter and the kinetic-energy preserving scheme presented in section 2.3.1. As it can be seen, the first order upwind scheme dissipates energy at a faster rate than the flux limiter scheme. This is the clear example of the properties we seek for our hybrid scheme, a non-dissipative base with a diffusive scheme to be used in a selective way only where it is necessary for stability purposes.

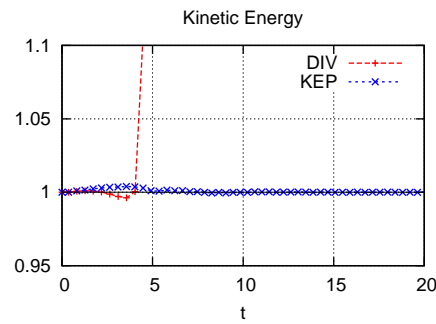


Figure 2.4: Total kinetic energy time evolution comparison of the conservative form (DIV) and the non-conservative form (KEP) on the inviscid Taylor-Green vortex problem.

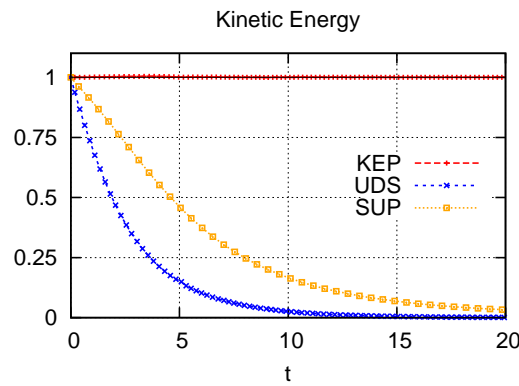


Figure 2.5: Inviscid Taylor-Green vortex problem mean Kinetic Energy time evolution for the different numerical schemes.

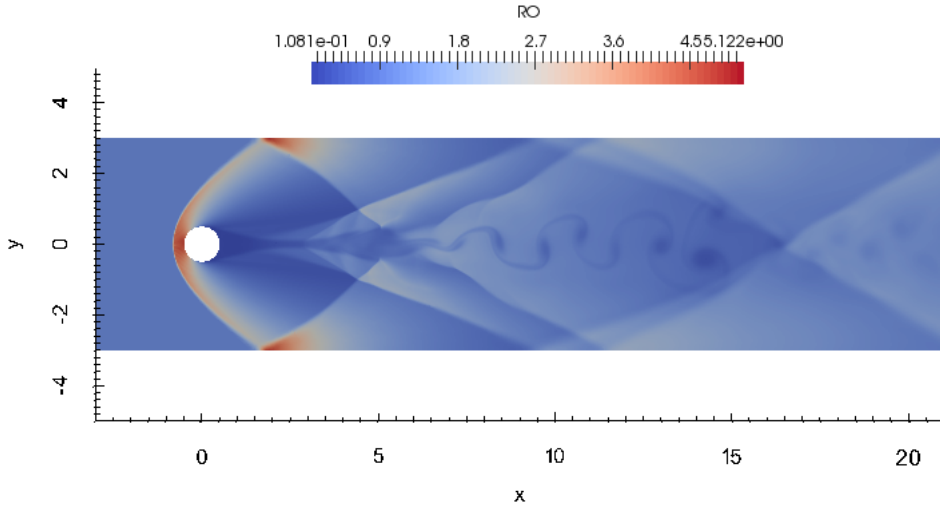


Figure 2.6: Computational domain and instantaneous density contours.

2.4.4 Supersonic Cylinder

The two-dimensional Mach 3.5 flow of a calorically perfect gas over a circular cylinder was simulated to test the ability of the hybrid scheme to resolve a flow rich in shock-shock and shock-vortex interactions. These type of interactions are of particular interest when computing turbulent flows with shock-boundary layer interactions (SBLIs). To that end, a viscous flow over a cylinder at a moderate Reynolds was computed to provide a complex temporally evolving flow. This case will check the ability of the hybrid scheme to robustly and reliably capture and resolve shock-shock and shock-vortex interactions.

Geometry and flow properties are defined in figure 2.6. Three grids were used to study the scheme behavior, one composed by $\approx 100k$ control volumes, a second one composed by $\approx 300k$ control volumes and a final one composed by $\approx 600k$ control volumes. All three meshes are unstructured grids, refined over the cylinder surface to ensure well reproduction of the boundary layer and also refined in the wake zone to reproduce well turbulent vortex.

The inlet and outlet boundaries, $x = -3$ and $x = 21$, are treated as supersonic inflow and non-reflective outflow respectively. The lower and upper boundaries,

$y = \pm 3$, are treated as inviscid walls. The cylinder wall is treated as a non-slip adiabatic wall. The flow is initialized with the upwind numerical scheme and run over several time units. Then, the hybrid scheme is enabled and the flow is simulated forward in time with the third order Runge-Kutta TVD scheme.

The discontinuity sensor behavior is depicted in figures 2.7 to 2.9. Figure 2.7 shows the Ducros sensor field for three different threshold values, ranging from 0.001 to 0.01. As it can be seen, for the lowest threshold value, the instability sensor over predicts the shock zone and introduce too much diffusion. As we raise the threshold, less flow is affected, being the threshold value of 0.005 the optimum value in this case, since the highest one (0.01) leads to an unstable simulation due to a lack of artificial diffusion. Nevertheless, when compared with results shown in figure 2.8, we see that the Ducros sensor is not as well suited for unstructured meshes since grid size also affect the discontinuity sensor field. This is the reason why the Larsson sensor is preferred, since it is sharper in discontinuities, not affected by grid configuration and since it is defined by two constants it is more versatile, being able to control shock-wave width and also the level of penetration in the boundary layer. Furthermore, for the lowest constant cases, turbulence is left unaffected by the discontinuity sensor (which only grows in shocks).

2.5 Application on the flow around a NACA0012 airfoil

The objective of this study is to analyze the turbulent flow around a NACA 0012 airfoil at $Re = 50000$, angle of attack $AoA = 5^\circ$ in different compressible regimes: from nearly incompressible ($Ma = 0.1$) to subsonic compressible ($Ma = 0.4$ and 0.6). The hybrid numerical scheme presented in this thesis will be used. Part of these results were presented at ECOMASS'14, under the title *Comparing kinetic energy preserving and high-order Godunov schemes on simulations of the flow around a NACA 0012*. Available data exists from other authors [45,46] that will be used to validate the numerical scheme. Jones et al. [46] computed DNS of the flow at $Ma = 0.4$ and provided reference data for this regimen. Rodríguez et al. [45] computed the incompressible flow around the airfoil and characterized the laminar separation bubble (LSB) behavior for this regimen. Both studies are used to verify the two first cases. Afterwards, a more challenging case at $Ma = 0.6$ is studied. At this point, the flow undergoes transonic resulting in a completely different flow behavior and strongly affecting the airfoil performance. To the author's knowledge, this case has not been presented yet.

Under adverse pressure gradient a boundary layer may separate, leading to reverse (upstream) fluid flow. Within the separated region disturbances are strongly amplified, typically leading to transition to turbulence. The resultant turbulent flow enhances mixing and momentum transfer in the wall-normal direction, and causes the boundary layer to reattach. This system of laminar separation, transition and

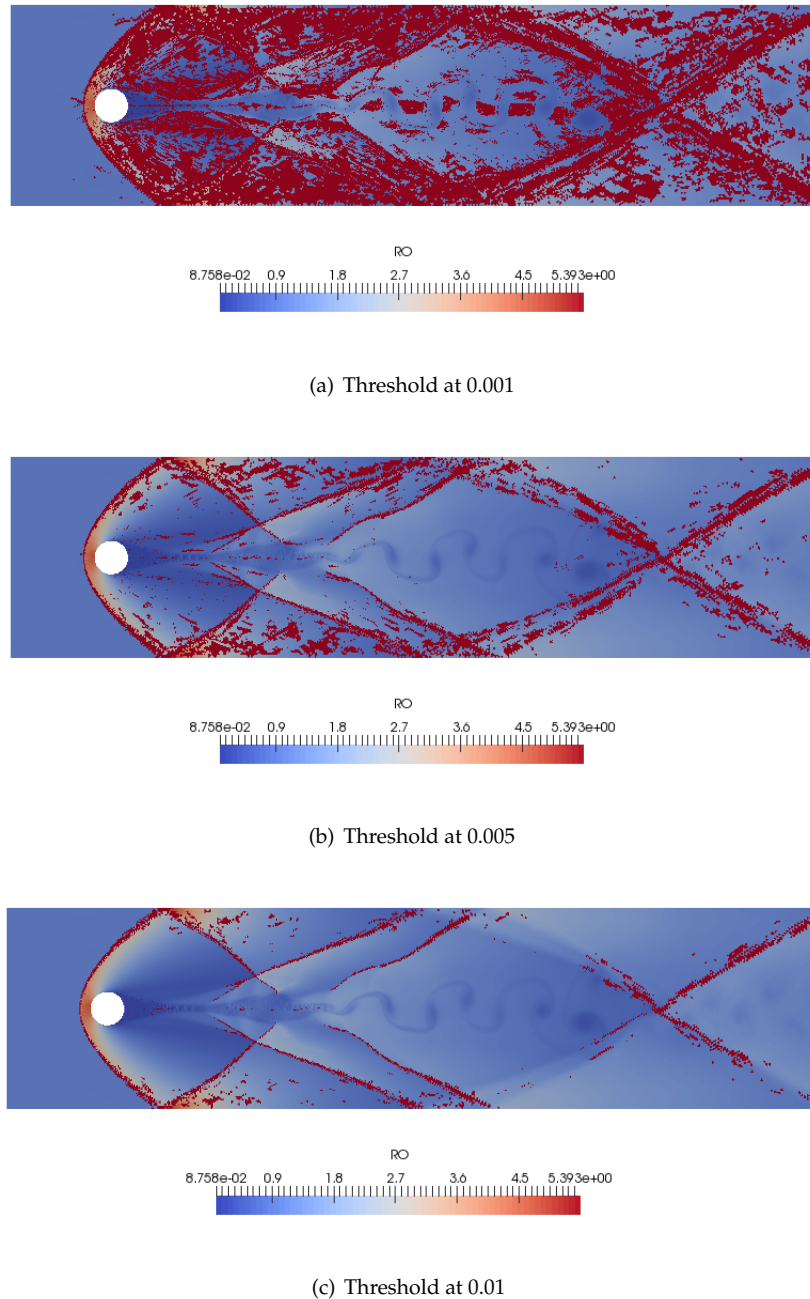


Figure 2.7: Ducros discontinuity sensor comparison.

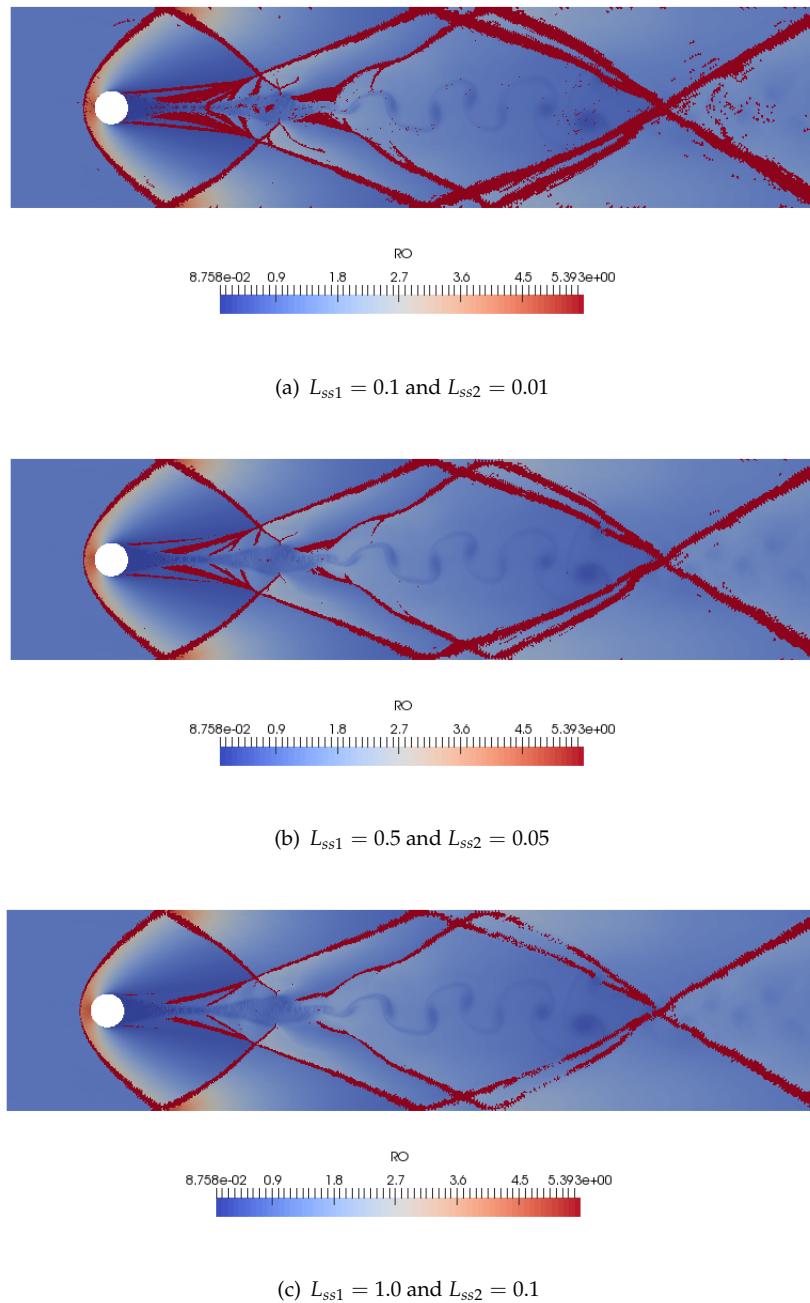
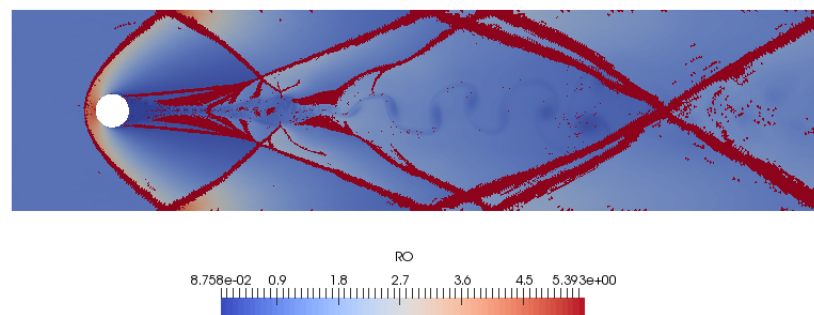
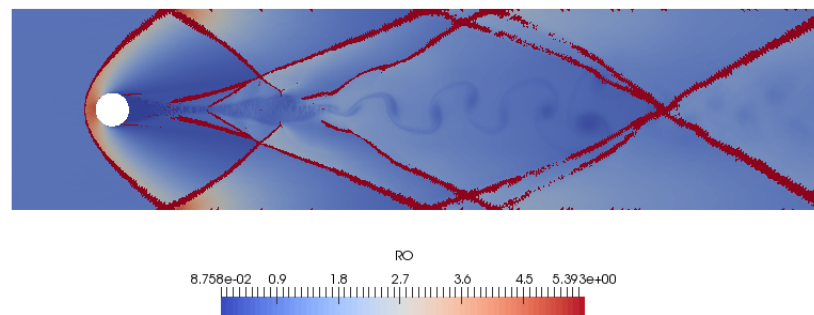


Figure 2.8: Larsson discontinuity sensor comparison.

(a) $L_{ss1} = 0.1$ and $L_{ss2} = 0.01$ (b) $L_{ss1} = 0.1$ and $L_{ss2} = 0.1$ **Figure 2.9:** Larsson discontinuity sensor comparison.

turbulent reattachment is referred to the already mentioned laminar separation bubble (LSB), and is typically associated with flows at low to moderate Reynolds numbers. In airfoils, forces are typically increased leading to loss in aerodynamics performance. The purpose of the present study is to investigate the influence of the Mach number on the LSB behavior and aerodynamic performance.

Grid geometry, resolution and boundary conditions.

The NACA0012 includes a sharp trailing edge and is rescaled to unit chord. The coordinate system is defined such that the leading and trailing edges are located at $(x, y) = (0, 0)$ and $(1, 0)$ respectively. Grids are unstructured, consisting of about 265k control volumes in a two-dimensional plane that is equidistantly spaced in the z -direction a total number of 96 planes. Therefore, the whole mesh involves more than 25M control volumes.

All simulations were run at a Reynolds number based on airfoil chord of $Re = 5 \times 10^4$, $AoA = 5^\circ$, at $Ma = 0.1, 0.4$ and 0.6 . The compressible NS equations are solved, using the hybrid numerical scheme presented in this thesis. The explicit third-order Adam-Bashford scheme is chosen for the temporal integration. Concerning boundary conditions, a subsonic inflow is used, along with a non-reflecting outflow. The surface of the airfoil is treated as a non-slip adiabatic wall. Periodicity is assumed in the span-wise direction.

Grid resolution is assumed to be enough for a DNS simulation, since the defined grid is the same that the one used in [45], where a resolution study was conducted to ensure all scales are resolved. As for the span-wise direction, a length of 0.2 is chosen based on reference studies.

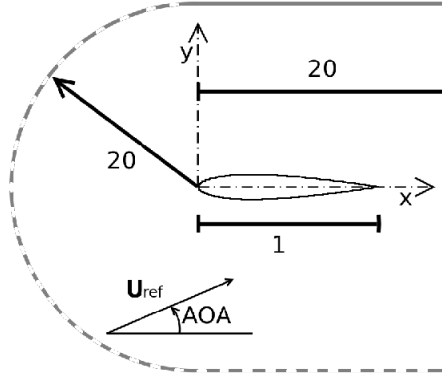


Figure 2.10: NACA0012 airfoil computational domain.

Statistical analysis

As it can be seen in table 2.1 and figure 2.11, the presented results are in good agreement with the reference results. The lift coefficient C_L rises as Mach increases, as it is predicted by the Prandtl-Glauert equation ($C_p(M) = C_p(0)/(1 - M^2)$). The same can be said for the drag coefficient C_D . Concerning the LSB, the separation point x_{sep} moves towards the leading edge due to the higher adverse pressure gradient. The reattachment point x_{reatt} also moves towards the leading edge, but the overall LSB length remains nearly constant, $x_{reatt} - x_{sep} \approx 0.4$ in all cases. Nevertheless, the LSB height increases with the Mach number due to the pressure waves build up towards the leading edge.

Case	C_L	C_D	x_{sep}	x_{reatt}
Rodríguez et al.	0.569	0.0291	0.170	0.566
DNS ($M = 0.1$)	0.569	0.0278	0.175	0.548
Jones et al.	0.615	0.0294	0.128	0.500
DNS ($M = 0.4$)	0.624	0.0334	0.119	0.492

Table 2.1: NACA0012 airfoil comparison with reference data.

Once the numerical approach is verified against other studies, a more challenging and unexplored case is performed. This is the transonic $Ma = 0.6$ flow around the airfoil. Traditional schemes based on numerical diffusion cannot be used for this case because the artificial dissipation would destroy turbulent scales. On the other hand, energy-consistent schemes cannot either be used because as soon as the flow reaches transonic conditions, error accumulation around shock-waves would result in a simulation blow-up. Hence, this is a sweetspot for our hybrid scheme: DNS (and LES) of turbulent flows with discontinuities. This is part of the reason why a relatively small number of transonic DNS and LES are found in the literature, the lack of accurate and stable numerical schemes that can deal with such flows.

First, the time evolution of the lift coefficient for the compressible cases are presented in figure 2.13. It can be seen how the C_L for the subsonic case, $Ma = 0.4$, oscillates at a high frequency near its mean value. In this case, the flow is attached and unsteadiness is caused by the vortex shedding downstream. This behavior is typical of attached flows. On the other hand, the lift time evolution of the transonic case, $Ma = 0.6$, shows the loss of performance once the transonic regimen is achieved. A very low frequency and high amplitude behavior is observed denoting a process of flow attachment and reattachment. This phenomenon is known as **transonic buffet** and limits aircraft flight envelope. It causes a dramatic loss in performance. For this reason, it is very important to control it.

Q-criterion is used to visualize turbulent structures on the transonic airfoil in fig-

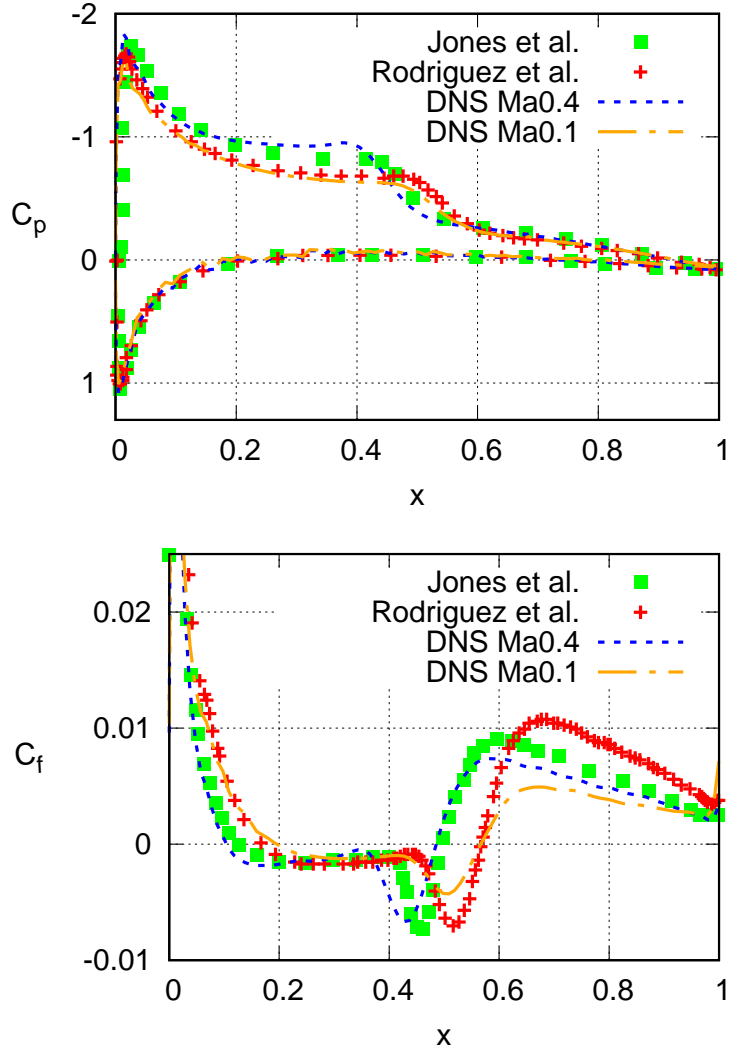


Figure 2.11: Pressure (left) and skin friction (right) coefficients distribution.

ure 2.14 . Two states are depicted, matching the higher and lower peaks on the lift coefficient time evolution. When the lift coefficient is higher, the flow is subsonic. Hence, the configuration is similar to that observed in the subsonic case. Never-

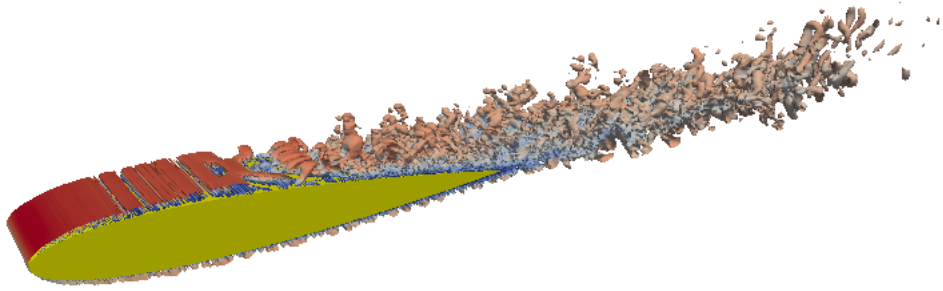


Figure 2.12: Q iso-contours for $Ma = 0.4$.

theless, the flow tends to accelerate through the extrados achieves sonic conditions forming a shock wave. This shock causes a high adverse pressure gradient on the boundary layer, causing it to fatten and resulting in a boundary layer detachment. This in turns causes the lift coefficient to drop abruptly causing the stall of the airfoil. Nevertheless, since the far field flow conditions are still subsonic, the flow can reattach again causing the lift coefficient to increase again repeating the cycle.

Summary

In the current work the subsonic incompressible, subsonic compressible and transonic compressible flow over a NACA0012 airfoil has been studied. The simulations have been performed by means of DNS at a $Re = 50000$, $AoA = 5^\circ$ and $Ma = 0.1, 0.4$ and 0.6 . All computations have been carried out in the same 26MCVs grid. The subsonic cases, corresponding to $Ma = 0.1$ and 0.4 have been compared with reference studies [45, 46]. Time-averaged lift coefficients are computed and compared, giving excellent agreement. LSB separation and reattachment points have also been computed and compared, with a good level of agreement. It was found that increasing the Mach number results in a higher value of the lift coefficient. Also, the detachment and reattachment points of the LSB moved towards the leading edge as Mach increased. Nevertheless, the total length of the LSB was nearly constant while its height decreased due to higher pressure build-up.

Once the numerical set-up was verified, a transonic case was performed. At this

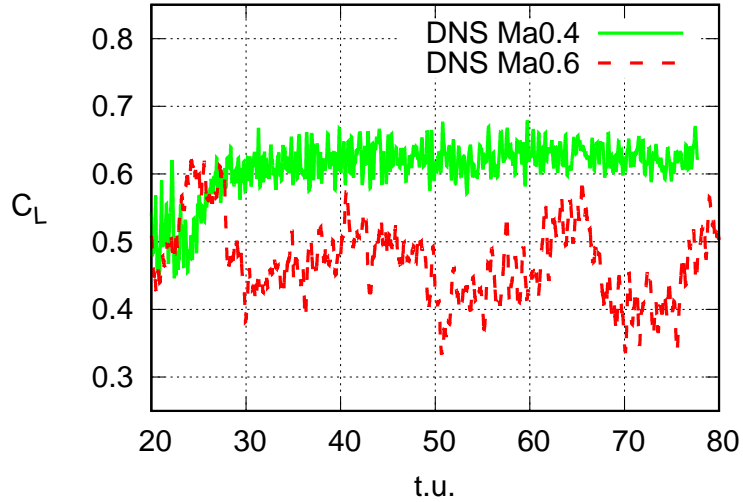


Figure 2.13: Lift coefficients time evolution.

regimen, lift coefficient showed a highly transient evolution high abrupt changes. The transonic buffet phenomena was observed and characterized, causing the flow over the airfoil to dettach and attach completely at very low frequencies. In supersonic aviation we want to fly fast, and since aircraft must take off and land transonic effects will occur in aircraft operation. First, the numerical tools presented in this thesis can be used to study the aerodynamic performance of such vehicles. Then, phenomenon like buffet (among others) can be characterized. Afterwards, the geometrical design can be changed in order to mitigate such loss in performance. Finally, the process would be repeated until design constrains are met. Flow control devices can also be added to the geometry and studied using the numerical tools developed in this thesis. Vortex-generators, for example, are useful devices in order to overcome performance loss due to transonic buffet.

2.6 Conclusions

At the beginning of this chapter we reviewed the state of the art concerning the numerical simulation of turbulent compressible flows. The main conclusions of this process revealed that in order to simulate the kind of flows we are interested in we have to use numerical schemes with low numerical dissipation. Kinetic energy preserving schemes (KEP) are chosen as the basis of our hybrid scheme since they do

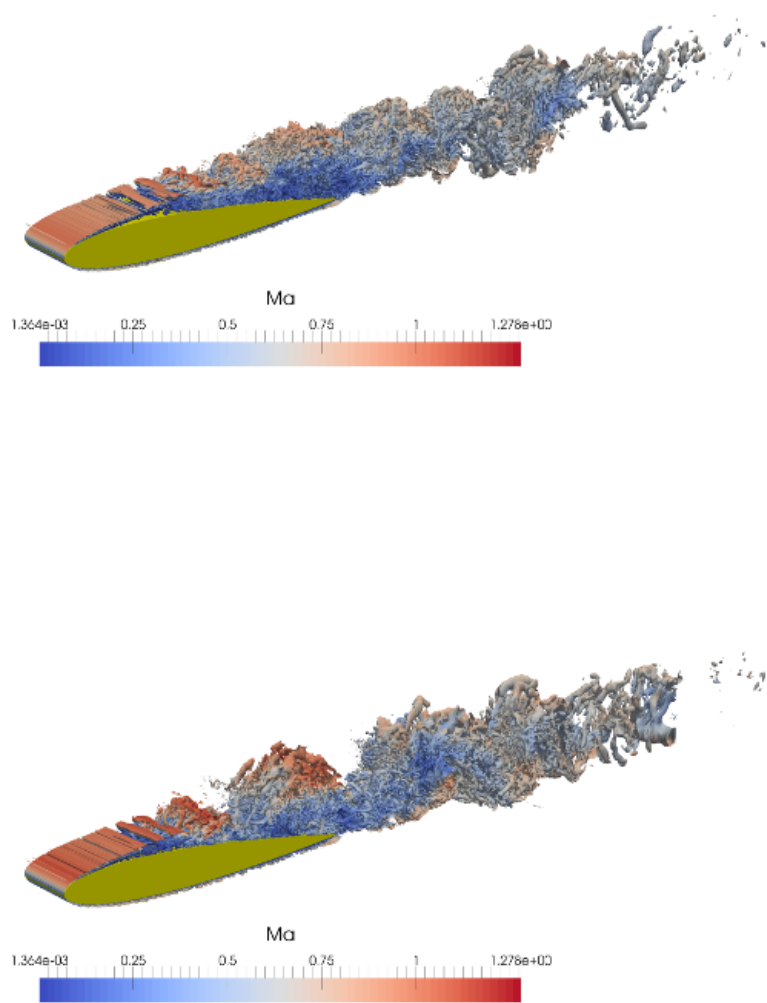


Figure 2.14: NACA0012 airfoil Q iso-contours for $Ma = 0.6$, subsonic regimen (top) and transonic (bottom).

not introduce numerical diffusion at all. However, in the presence of flow discontinuities, this kind of methods suffer from instabilities. It is at this point where we resort to an upwind scheme in order to introduce a small amount of numerical diffusion, only in shock waves. The use of a good shock sensor is crucial for a hybrid scheme.

Concerning the implementation details, we saw how the use of a KEP scheme in its splitting form is required in order to obtain a scheme that is both accurate and stable in time. On the other hand, the use of a approximate Riemann solver help to overcome the cost related to the solution of the Riemann problem required by the upwind scheme.

The developed method has been tested in several cases designed to evaluate the different key properties that a numerical scheme must present in order to simulate turbulent discontinuous flows accurately and reliably. They are: the ability to identify and reproduce shocks without interfering other flow structures (turbulent vortex and boundary layers), kinetic energy-preservation on the smooth parts of the flow minimizing the introduction of numerical dissipation. The first test consisted on a shock tube. Results showed that the KEP scheme was unstable due to the discontinuities, while the hybrid and UDS scheme were stable. The second test consisted on the advection of a 2D isentropic vortex. Results showed that the KEP scheme was able to advect the vortex indefinitely conserving its shape, while the UDS scheme was diffusing the vortex throughout the simulation. Since the problem has no discontinuities, only the KEP part of the hybrid scheme was activated. The next test was the 3D Taylor-Green vortex problem, which confirmed the ability of the KEP scheme to preserve the total amount of kinetic energy during the simulation while the UDS scheme dissipated it. We also confirmed the requirement on using the KEP scheme in its splitting form, since the diverging form resulted in a fast simulation blow up. The final test consisted on the supersonic flow around a circular cylinder. We demonstrated that the use of a Larsson detector is a better choice for unstructured grids. We also saw the ability of the final hybrid scheme to capture sharp discontinuities leaving turbulent structures unaffected by the numerical diffusion. After all the test were performed, the hybrid scheme was used to study the flow over a NACA0012 airfoil at different compressible regimens. Concerning the computational part of the study, the hybrid scheme performed well in all the cases. For the subsonic cases, results showed very good agreement with reference data. On the transonic case, the scheme also performed well, allowing to obtain results thanks to the stabilization introduced via the upwind scheme whenever shocks appeared. Concerning the physical part of the case, we saw how increasing the Mach number affects the LSB behavior, moving it towards the leading edge until the flow undergoes transonic. Once this condition is achieved, the flow separates and reattaches at a small frequency causing the flow to be highly unstable with a strong loss in performance. This phenomena is known

as buffet and it is typical of transonic flows over airfoils.

References

- [1] R. Courant, E. Isaacson, and M. Rees. On the solution of non-linear hyperbolic differential equations. *Commun. Pure Appl. Math.*, 5:243â55, 1952.
- [2] S K. Godunov. A difference scheme for numerical computation of discontinuous solution of hydrodynamic equations. *Math. Sbornik*, 47:271â306, 1959.
- [3] J. von Neumann and R D. Richtmyer. A method for the calculation of hydrodynamical shocks. *J. Appl. Phys.*, 21:232â7, 1950.
- [4] C. Hirsch. *Numerical Computation of Internal and External Flows*. New York:Wiley, 1988.
- [5] C B. Laney. *Computational Gasdynamics*. Cambridge, UK: Cambridge Univ. Press, 1998.
- [6] R. Leveque. *Numerical Methods for Conservation Laws*. Basel: Birkhauser-Verlag, 1990.
- [7] E F. Toro. *Riemann Solvers and Numerical Methods for Fluid Dynamics*. New York: Springer, 2009.
- [8] S. Pirozzoli. Numerical Methods for High-Speed Flows. *Annu. Rev. Fluid Mech.*, 43:163â94, 2011.
- [9] R. Samtaney, D I. Pullin, and B. Kosovic. Direct numerical simulation of decaying compressible turbulence and shocklet statistics. *Phys. Fluids*, 13:1415â30, 2001.
- [10] P L. Roe. Approximate riemann solvers, parameter vectors, and difference schemes. *J. Comput. Phys.*, 43:357â72, 1981.
- [11] B. van Leer. Towards the ultimate conservative difference scheme v. a second order sequel to godunovs method. *J. Comput. Phys.*, 32:101â36, 1979.
- [12] A. Harten, B. Engquist, S. Osher, and S R. Chakravarthy. Uniformly high order accurate essentially nonoscillatory schemes. *J. Comput. Phys.*, 71:231â303, 1987.
- [13] X D. Liu, S. Osher, and T. Chan. Weighted essentially non-oscillatory schemes. *J. Comput. Phys.*, 115:200â12, 1994.

- [14] G S. Jiang and C W. Shu. Efficient implementation of weighted eno schemes. *J. Comput. Phys.*, 126:202–28, 1994.
- [15] T. Colonius and S K. Lele. Computational aeroacoustics: progress on nonlinear problems of sound generation. *Progr. Aerosp. Sci.*, 40:345–416, 2004.
- [16] N A. Phillips. An example of nonlinear computational instability. In *The Atmosphere and the Sea in Motion*, Oxford, UK: Oxford Univ. Press, pages 501–4, 1959.
- [17] D K. Lilly. On the computational stability of numerical solutions of time-dependent non-linear geophysical fluid dynamics problems. *J. Comput. Phys.*, 93:11–26, 1965.
- [18] A E. Honein and P. Moin. Higher entropy conservation and numerical stability of compressible turbulence simulations. *J. Comput. Phys.*, 201:531–45, 2004.
- [19] B. Strand. Summation by parts for finite difference approximations for d/dx . *J. Comput. Phys.*, 110:47–67, 1994.
- [20] F. Ducros, F. Laporte, T. Soulères, V. Guinot, P. Moinat, and B. Caruelle. High-order fluxes for conservative skew-symmetric-like schemes in structures meshes: application to compressible flows. *J. Comput. Phys.*, 161:114–39, 2000.
- [21] S K. Lele. Compact finite difference schemes with spectral-like resolution. *J. Comput. Phys.*, 103:16–42, 1992.
- [22] M R. Visbal and D V. Gaitonde. High-order accurate methods for complex unsteady subsonic flows. *AIAA J.*, 37:1231–9, 1999.
- [23] E. Tadmor. The numerical viscosity of entropy stable schemes for systems of conservation laws. *I. Math. Comput.*, 49:91–103, 1987.
- [24] M. Gerritsen and P. Olsson. A stable high order finite difference scheme and sharp shock resolution for the euler equations. *J. Comput. Phys.*, 129:245–62, 1996.
- [25] G. Moretti. Computation of flows with shocks. *Annu. Rev. Fluid Mech.*, 19:313–37, 1987.
- [26] E. Johnsen, J. Larsson, A V. Bhagatwala, W H. Cabot, P. Moin, B J. Olson, P S. Rawar, S K. Shankar, B. Sjogreen, H C. Yee, X. Zhong, and S K. Lele. Assessment of high-resolution methods for numerical simulations of compressible turbulence with shock waves. *J. Comput. Phys.*, 229:1213–37, 2010.

- [27] A. Jameson, W. Schmidt, and E. Turkel. Numerical simulation of the euler equations by finite volume methods using runge-kutta time stepping schemes. *AIAA paper*, page 1259, 1981.
- [28] J. Casper and M H. Carpenter. Computational considerations for the simulation of shock-induced sound. *SIAM J. Sci. Comput.*, 19:813–828, 1998.
- [29] J. Larsson and S K. Lele. Direct numerical simulation of canonical shock/turbulence interaction. *Phys. Fluids*, 21:126101, 2009.
- [30] M. Arora and P L. Roe. On postshock oscillations due to shock capturing schemes in unsteady flows. *J. Comput. Phys.*, 130:25–40, 1999.
- [31] A. Harten. Eno schemes with subcell resolution. *J. Comput. Phys.*, 83:148–84, 1989.
- [32] E. Johnsen and T. Colonius. Implementation of weno schemes in compressible multicomponent flow problems. *J. Comput. Phys.*, 219:715–32, 2006.
- [33] V A. Titarev and E F. Toro. Finite-volume weno schemes for three-dimensional conservation laws. *J. Comput. Phys.*, 201:238–60, 2004.
- [34] V A. Titarev amd E F. Toro. Ader schemes for three-dimensional non-linear hyperbolic systems. *J. Comput. Phys.*, 204:715–36, 2005.
- [35] C. Hu and C W. Shu. Weighted essentially non-oscillatory schemes on triangular meshes. *J. Comput. Phys.*, 150:97–127, 1999.
- [36] M. Dumbser, M. Kaser, V A. Titarev, and E F. Toro. Quadrature-free non-oscillatory finite volume schemes on unstructured meshes for nonlinear hyperbolic systems. *J. Comput. Phys.*, 226:204–43, 2007.
- [37] A. Jameson. Formulation of kinetic energy preserving conservative schemes for gas dynamics and direct numerical simulation of one-dimensional viscous compressible flow in a shock tube using entropy and kinetic energy preserving schemes. *J. Sci. Comput.*, 34:188–208, 2008.
- [38] P K. Subbareddy and G V. Candler. A fully discrete, kinetic energy consistent finite-volume scheme for compressible flows. *J. Comput. Phys.*, 228:1347–64, 2009.
- [39] J B. Perot. Discrete conservation properties of unstructured mesh schemes. *Annu. Rev. Fluid Mech.*, 43:299–318, 2009.
- [40] Axel Rohde. Eigenvalues and eigenvectors of the Euler equations in general geometries. *AIAA*, 2609, 2001.

- [41] J. Randall and Leveque. *Finite Volume Methods for Hyperbolic Problems*. Cambridge University Press, 2002.
- [42] F. Ducros, V. Ferrand, F. Nicoud, C. Weber, D. Darracq, C. Gachereau, and T. Poinsot. Large-eddy Simulation of Shock-turbulence Interaction. *J. Comput. Phys.*, 152(2):517–49, 1999.
- [43] J. Larsson, R. Vicquelin, and I. Bermejo-Moreno. Large Eddy Simulations of the HyShot ii Scramjet. *Center For Turbulence Research, Annual Research Report Briefs*, 2011.
- [44] F. Davoudzadeh, H. McDonald, and B E. Thompson. Accuracy Evaluation of Unsteady CFD Numerical Schemes by Vortex Preservation. *Comput. Fluids*, 24(8):883–95, 1995.
- [45] I. Rodríguez, O. Lehmkuhl, R. Borrell, and A. Oliva. Direct Numerical Simulation of a NACA0012 in Full Stall. *Int. J. Heat Fluid Fl.*, 43:194–203, 2013.
- [46] L E. Jones, R D. Sandberg, and N D. Sandham. Direct numerical simulations of forced and unforced separation bubbles on an airfoil at incidence. *J. Fluid Mech.*, 602:175–207, 2008.

Boundary conditions for turbulent compressible flows.

3.1 Introduction

For the resolution of any system of Partial Differential Equations (PDEs) two elements are required to close the problem: the initial condition and boundary conditions. The initial condition establish the starting value for all the unknown variables from which they will be evolved in time and space according to the PDEs. Boundary conditions determine the values for the unknowns in the computational domain limits.

Any numerical scheme is constrained by the boundary conditions which have to be included in the final numerical model. Most turbulent studies with DNS are performed with periodic boundary conditions. In these configurations, the reference frame moves at the mean flow speed and flow periodicity is assumed. This is the only geometry for which the problem can be closed exactly at the boundary. By assuming periodicity, the computational domain is folded on itself and no boundary conditions area is actually required. Nevertheless, the periodicity assumption considerably limits the possible applications of these simulations. When no periodicity is considered, flow inlets and outlets must be treated. These simulations are dependent on the boundary conditions and on their treatment, and general boundary conditions for direct simulations of compressible flows are needed.

The intention of this chapter is to present a new methodology for the computation of boundary conditions for both DNS and LES of turbulent compressible flows.

The approach is useful for a wide range of applications. First, we review classical approaches found in the literature. Then, the numerical methodology developed in this thesis is presented. Finally, some tests are performed to evaluate the behavior of the different boundary conditions developed.

3.2 State of the art

Among the different methods for DNS and LES computation of boundary conditions on turbulent compressible flows, the one that has seen more success is the NSCBC method (Navier-Stokes Characteristic Boundary Conditions) [1,2]. Poinsot et al. [1] derived boundary conditions for the direct simulation of compressible flows in the finite difference framework and provide notions of well-posedness along with some simple tests. This approach consists of solving the finite difference NS equations at nodes placed at the boundaries transforming normal boundary terms in its wave-approach equivalent (via the hyperbolic analysis, see section 1.3.3). Then, incoming waves are related to outgoing waves using the so called LODI relations (Local One-Dimensional Inviscid). Lodato et al. [2] use the same approach and provide study of well-posedness and transverse terms influence on outflow boundary conditions. In summary, the problem of specifying boundary conditions is reduced to determining wave amplitudes variations for outgoing waves (from inside information) and incoming waves (using the LODI relations) and then solving balance equations as opposed to prescribing directly values of the principal variables. This one-dimensional assumption works well in flows that are essentially unidirectional (shear layers or jets) but they are problematic in flow geometries that are strongly multi-directional [3]. This issue, however, can be alleviated with the use of transverse terms [4].

Consider the NS system of PDEs

$$\begin{aligned} \rho_t + \nabla \cdot (\rho \mathbf{u}) &= 0 \\ (\rho \mathbf{u})_t + \nabla \cdot (\rho \mathbf{u} \mathbf{u}) &= \nabla \cdot \boldsymbol{\tau} - \nabla p \\ E_t + \nabla \cdot ((E + p) \mathbf{u}) &= \nabla \cdot (\mathbf{u} \boldsymbol{\tau}) - \nabla \cdot \mathbf{q} \\ p &= \rho R_g T \end{aligned} \quad (3.1)$$

where p is the pressure, ρ is the density of the fluid, $\mathbf{u} = (u, v, w)$ is the velocity vector, E is the total energy, T is the temperature and R_g is the gas constant. Viscous and heat transfer terms are expressed as

$$\begin{aligned} \tau_{ij} &= \mu \left[\left(\frac{\partial u_i}{\partial x_j} + \frac{\partial u_j}{\partial x_i} \right) - \frac{2}{3} \frac{\partial u_k}{\partial x_k} \delta_{ij} \right] \\ \mathbf{q} &= -\kappa \nabla T \end{aligned} \quad (3.2)$$

where μ is the molecular viscosity, computed using the Sutherland's law, and $\kappa = \frac{\mu c_p}{Pr}$ is the thermal conductivity.

The LODI equations on the boundary in their primitive variables become

$$\frac{\partial}{\partial t} \begin{pmatrix} \rho \\ u_n \\ u_{t1} \\ u_{t2} \\ p \end{pmatrix} + \begin{pmatrix} (\mathcal{L}_1 + \mathcal{L}_5 + 2\mathcal{L}_2)/2a^2 \\ (\mathcal{L}_5 - \mathcal{L}_1)/2\rho a \\ \mathcal{L}_3 \\ \mathcal{L}_4 \\ (\mathcal{L}_5 + \mathcal{L}_1)/2 \end{pmatrix} + \begin{pmatrix} (\mathcal{T}_1 + \mathcal{T}_5 + 2\mathcal{T}_2)/2a^2 \\ (\mathcal{T}_5 - \mathcal{T}_1)/2\rho a \\ \mathcal{T}_3 \\ \mathcal{T}_4 \\ (\mathcal{T}_5 + \mathcal{T}_1)/2 \end{pmatrix} = 0 \quad (3.3)$$

where a is the speed of sound, u_n is the boundary normal velocity and u_{t1}, u_{t2} are the boundary transverse velocities and \mathcal{T} are the transverse terms. The amplitude vector of the characteristic waves is given by

$$\mathcal{L} = \begin{pmatrix} \mathcal{L}_1 \\ \mathcal{L}_2 \\ \mathcal{L}_3 \\ \mathcal{L}_4 \\ \mathcal{L}_5 \end{pmatrix} = \begin{pmatrix} \lambda_1 \left(\frac{\partial p}{\partial x_n} - \rho a \frac{\partial u_n}{\partial x_n} \right) \\ \lambda_2 \left(a^2 \frac{\partial \rho}{\partial x_n} - \frac{\partial p}{\partial x_n} \right) \\ \lambda_3 \frac{\partial u_{t1}}{\partial x_n} \\ \lambda_4 \frac{\partial u_{t2}}{\partial x_n} \\ \lambda_5 \left(\frac{\partial p}{\partial x_n} + \rho a \frac{\partial u_n}{\partial x_n} \right) \end{pmatrix} \quad (3.4)$$

where λ_i are the characteristic velocities

$$\begin{pmatrix} \lambda_1 \\ \lambda_2 \\ \lambda_3 \\ \lambda_4 \\ \lambda_5 \end{pmatrix} = \begin{pmatrix} u_n - a \\ u_n \\ u_n \\ u_n \\ u_n + a \end{pmatrix} \quad (3.5)$$

Transverse terms are an open issue and several formulations can be found in [3–5].

Consider a subsonic outflow. All waves go out except the acoustic wave traveling at speed $u_n - a$. Therefore, all the \mathcal{L}_i can be computed with equation 3.4 except for \mathcal{L}_1 . DNS and LES of compressible flows require an accurate control of wave reflection from the boundaries of the computational domain [1]. Often, reflected waves are damped due to the numerical dissipation of the numerical scheme. This is the case when using upwind-like numerical schemes or RANS turbulence models [1]. For DNS and LES, however, numerical viscosity is reduced as much as possible, and wave reflection at boundaries has to be eliminated with appropriate formulations. If

this issue is not addressed carefully, acoustics reflection can interact with turbulent structures leading to flow instabilities and performance miss-prediction. Poinsot et al. [1] prescribe

$$\mathcal{L}_1 = K(p - p_\infty) \quad (3.6)$$

where $K = \sigma a(1 - Ma^2)/l_{x_n}$ with Ma the maximum Mach number of the boundary, l_{x_n} is the characteristic size of the domain in the boundary normal direction and σ is a constant usually set to 0.25 [5]. A perfectly non-reflecting boundary condition is achieved with $K = 0$. Expression 3.6 works well with flows that are normal to the outlet, but they produce excessive oscillations when vortices leave the domain. Alternative approaches can be found in the literature [3–5].

Summarizing, NSCBC and their posterior improvements propose a methodology to evaluate boundary conditions solving finite difference Navier Stokes equations taking advantage of their wave-like structure. Advantages of the method are its robustness, spread use and strong literature. Disadvantages include the necessity to transform the reference system velocities to the face boundary reference system, perform computations on this reference system, and then bring back results to the original reference system (expensive task on unstructured meshes), difficulty on transverse terms definition and computation, they are not suitable for edges and corners where additional formulation must be considered. Finally, they are developed in the finite difference framework, which can lead to problems in finite volume or finite elements codes. All these facts motivate the study and development of new kind of boundary conditions in order to overcome the aforementioned problems.

3.3 Development of new boundary conditions

In this thesis boundary conditions are derived within the FVM (we seek for fluxes at the boundaries), for arbitrary meshes. The full three-dimensional wave structure is considered in the hyperbolic analysis. Ghost cells are considered outside of the domain, where values for the variables are defined in order to obtain the desired flux at the boundary. Edges and corners particularly benefit from this approach. Since boundary conditions are imposed weakly though fluxes the volumes that share different boundary conditions (e.g. walls and outflow for edges and corners) are not as influenced from boundary conditions restrictions as other approaches that need to implement specific boundary conditions for corners in order to stabilize them [4]. Furthermore, impose boundary conditions weakly can have advantages on the overall numerical stability, specially when low-dissipative schemes are used in DNS and LES [6].

Following the nomenclature used in [1] a boundary condition is called a **physical** boundary condition when its value is known. For example, the velocity in a static

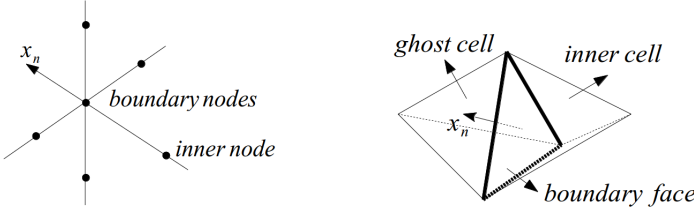


Figure 3.1: Geometrical configuration for boundary computation. On the left, the approach proposed by Poinsot et al. (finite difference). On the right, the approach proposed in this thesis (finite volume).

wall is always null. These conditions are independent of the numerical method used to solve the relevant equations. On the other hand, **numerical** boundary conditions are required when the number of physical boundary conditions are less than the number of conserved variables (which is almost always the case). In order to determine these conditions, conservation laws are solved at boundaries as opposed to prescribing directly values of the unknown variables. The details concerning the numerical procedure in order to evaluate boundary conditions are presented in the following subsections. First, we will consider fluid-type conditions. This boundary conditions connect two fluid nodes through the boundaries (e.g. inflows, outflows, periodic, etc). Solid-type conditions (i.e. walls) are treated separately.

In section 1.4 the methodology for the resolution of the NS equations using finite volume methods was presented. In order to evaluate the evolution of the conserved variables, the net rate of accumulation in each control volume has to be computed via fluxes at faces. The class of numerical methods we consider in this thesis only involves information at both sides of each face in order to compute the fluxes. Those volumes with a boundary face will use information from the ghost nodes, where boundary conditions are imposed, in the same way that interior faces.

3.3.1 Fluid-type boundary conditions

Consider the three-dimensional conservation law

$$\phi_t + \nabla \cdot f(\phi) = 0 \quad (3.7)$$

where

$$\phi = \begin{pmatrix} \rho \\ \rho\mathbf{u} \\ E \end{pmatrix} \quad f_n(\phi) = \begin{pmatrix} \rho u_n \\ \rho u_n \mathbf{u} + p \mathbf{n} \\ (E + p)u_n \end{pmatrix} \quad (3.8)$$

are the conserved variables (density, momentum and total energy, respectively) and the convective flux through a general face with normal \mathbf{n} . Now consider the convective fluxes through an arbitrary face. Using the characteristic analysis presented in section 1.3.3 we can recast the system as:

$$\phi_t + R\mathcal{L} = 0 \quad (3.9)$$

where R is the right eigenvectors matrix [7] and $\mathcal{L} = \Lambda w_{x_n}$, being Λ the characteristic speeds matrix and w_{x_n} the gradient of the different waves through the boundary normal direction. Recall that $w = R^{-1}\phi$ allows us to find the waves from the conserved variables.

$$\frac{\partial}{\partial t} \begin{pmatrix} \rho \\ \rho u \\ \rho v \\ \rho w \\ E \end{pmatrix} + R \begin{pmatrix} \lambda_1 \frac{\partial \omega_1}{\partial x_n} \\ \lambda_2 \frac{\partial \omega_2}{\partial x_n} \\ \lambda_3 \frac{\partial \omega_3}{\partial x_n} \\ \lambda_4 \frac{\partial \omega_4}{\partial x_n} \\ \lambda_5 \frac{\partial \omega_5}{\partial x_n} \end{pmatrix} = 0 \quad (3.10)$$

Hence, an algorithm to evaluate boundary values can be defined as follows:

- Step 1. Compute the characteristic speeds Λ (this will indicate which waves enter the domain and which are leaving it).
- Step 2. With ϕ^n compute the left eigenvectors R^{-1} and the waves w at the boundary and interior nodes for the waves leaving the domain (non-reflecting approach).
- Step 3. Compute \mathcal{L}' s for numerical boundary conditions.
- Step 4. Compute the residue $R\mathcal{L}$ and solve equation 3.9 to obtain ϕ^{n+1} .
- Step 5. Prescribe new values for physical boundary conditions.

Once the general approach is presented, specific implementations are now explored for different boundary conditions.

Subsonic inflow

Subsonic inflows can be specified defining the mass flow at the inlet. This can be achieved by either specifying the flow velocity and density or the flow total pressure and temperature plus flow direction. In any case, only \mathcal{L}_5 with characteristic speed $u_n + a$ can be computed from interior points, since we consider the boundary face-unit-normal vector pointing outside the domain. The rest of the waves travel into the domain (see figure 3.2, left).

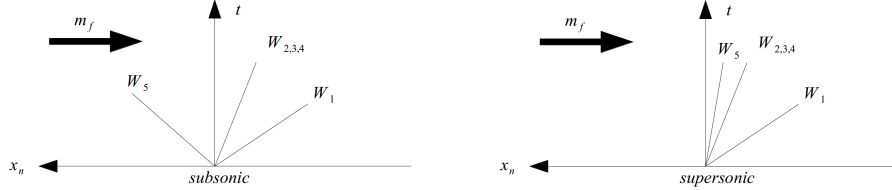


Figure 3.2: Inflow wave diagram.

If we fix the mass flow specifying the inlet density and velocity we only need to solve an equation for the total energy. Furthermore, since only one wave is leaving the domain, the equation reduces to:

$$E_t + (H + au_n)(a + u_n)w_{x_n}^5 = 0 \quad (3.11)$$

where H and a are the enthalpy and speed of sound at the boundary ghost cell.

Supersonic inflow

Supersonic inlets are the simplest boundary conditions for compressible flows. Since no information can travel upstream, all the variables are fixed.

Outflow

Outflow conditions can be specified with a static pressure value or without any value at all. Velocity is unknown and both subsonic and supersonic cases can coexist, thus requiring local adaptation depending on the Mach number at each boundary face. In a subsonic outflow, all the waves leave the domain except for \mathcal{L}_1 with characteristic speed $u_n - a$. In a supersonic outflow, all the waves are leaving. Therefore, as in the supersonic inflow, no information travels upstream (see figure 3.3).

If we specify a static pressure, only equations for density and momentum have to be solved. In the other case, also the energy equation must be considered. Supersonic outlets must solve the entire system of equations 3.9 while the subsonic case is solved simply with $\mathcal{L}_1 = 0$.

3.3.2 Solid-type boundary conditions

Since waves cannot travel through solids, and there is no mass flow through this type of boundary conditions, the mass flux crossing a solid type surface is zero.

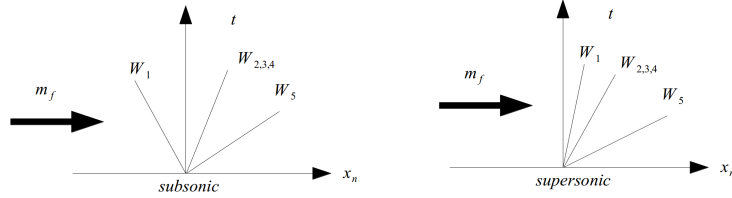


Figure 3.3: Outflow wave diagram.

$$f(\phi) = \begin{pmatrix} 0 \\ p\mathbf{n} \\ 0 \end{pmatrix} \quad (3.12)$$

In case of non slip walls, boundary conditions are specified at wall nodes assuming a zero-pressure gradient and a fixed velocity equal to the velocity of the wall. For isothermal walls, temperature (and hence density) is fixed. For adiabatic walls, zero-temperature gradient in the wall-normal direction is assumed. Therefore, temperature and density are also known. Since all the values are known, no need for solving equations is required.

3.4 Numerical tests

A series of numerical tests are presented now in order to evaluate the performance of the boundary conditions presented in this thesis.

3.4.1 Acoustic pulse

One simple test to evaluate the reflecting properties of the boundary conditions is a simple acoustic pulse. Figure 3.4 shows the time evolution of a pressure pulse in a steady flow. Left and bottom boundary conditions are treated as non-slip walls, hence wave reflection is expected. On the other hand, right and top boundary conditions are treated as non-reflecting outlets, hence the acoustic waves should leave the domain without reflections.

3.4.2 Two-dimensional vortex advection

Both inflows and outflows conditions are tested on the advection of a two-dimensional vortex. The problem consists of a vortex superimposed on a freestream u_0 , as depicted in figure 3.5. The vortex is then convected downstream until it reaches the

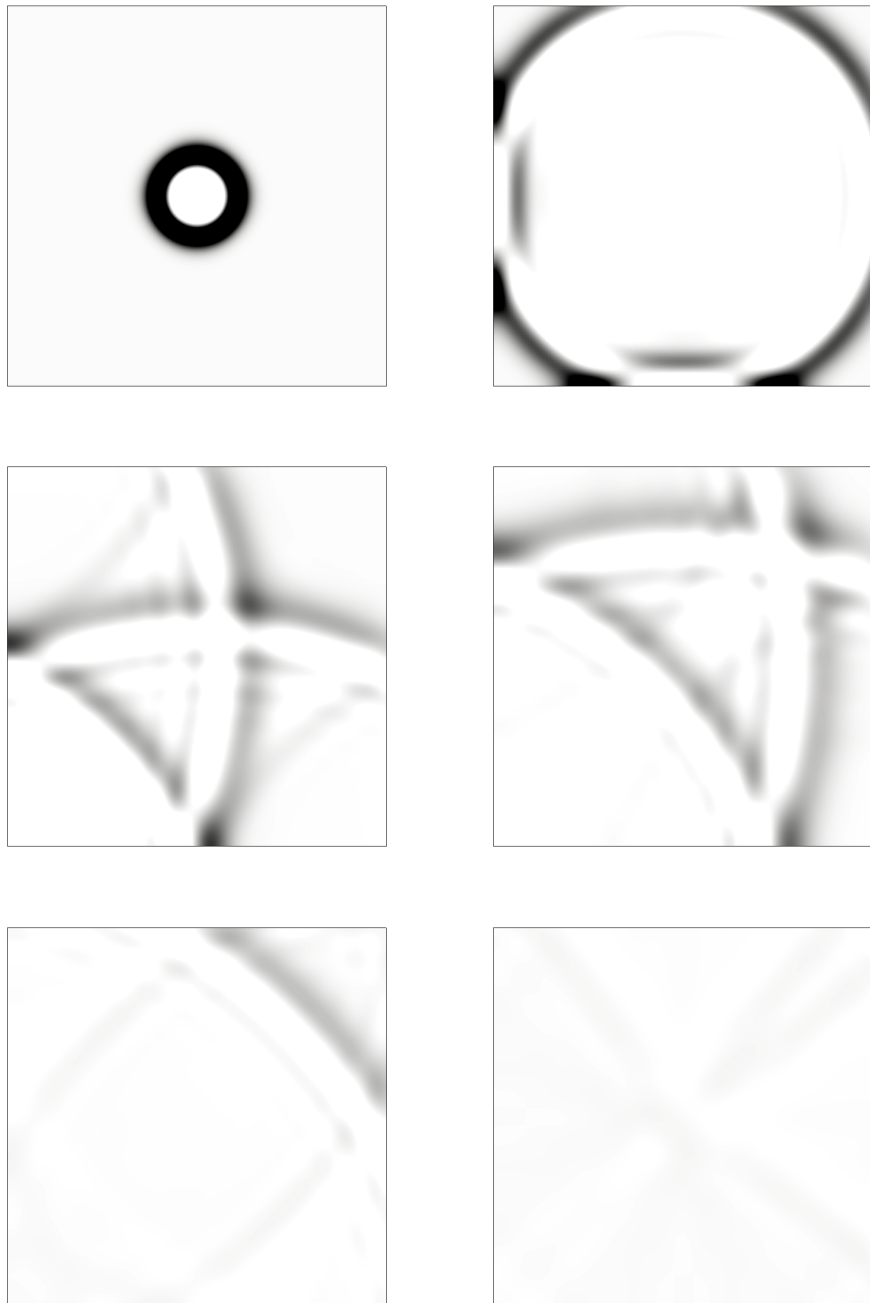


Figure 3.4: Wave front for a pressure pulse in a steady flow reflecting on the left and bottom walls, and leaving the computational domain without reflecting through top and right outlets.

outlet. The vortex must be able to exit the computational domain without reflections. The velocity field of the vortex is initialized using the stream function for an incompressible non-viscous vortex in cylindrical coordinates:

$$\begin{pmatrix} u \\ v \end{pmatrix} = \begin{pmatrix} u_0 \\ 0 \end{pmatrix} + \frac{1}{\rho} \begin{pmatrix} \frac{\partial \Psi}{\partial y} \\ -\frac{\partial \Psi}{\partial x} \end{pmatrix} \quad (3.13)$$

$$\Psi = C \exp\left(-\frac{x^2 + y^2}{2R_c^2}\right) \quad (3.14)$$

where C determines the vortex strength and R_c is the vortex radius. The pressure field is initialized as:

$$p - p_\infty = \rho \frac{C^2}{R_c^2} \exp\left(-\frac{x^2 + y^2}{2R_c^2}\right) \quad (3.15)$$

for this case the mean flow characteristics are

$$Ma = 0.5 \quad Re = 10000 \quad (3.16)$$

A 2×2 squared domain with a total number of 120×120 control volumes was used. The vortex is initially located in the center of the domain and is defined by

$$R_c/l = 0.15 \quad C/(cl) = -0.0005 \quad (3.17)$$

Boundary conditions were treated using the methodology presented before, with an inlet, an outlet and slip walls for lateral boundaries.

Vorticity fields are represented in figure 3.6 at different time instants. The initial vortex is convected downstream. At $t = 1$ half of the vortex has already left the computational domain, the vorticity profile is preserved for the other half without instabilities. At $t = 2$ the original vortex has disappeared and no noticeable perturbations within the flow are observed.

3.4.3 Driven Cavity

In order to test the non-slip boundary condition, the driven cavity problem is solved. This problem consists of a two-dimensional square cavity where the top wall has non-zero velocity. Walls are adiabatic for this case. This is an interesting problem because we have both static and moving walls. The mesh used was a 50×50 structured mesh with $\Delta x_w = 0.005$ in order to ensure good boundary layer reproduction. Figures 3.7 and 3.8 show the velocity profiles for two different cases. As it can be seen, numerical solution is in good agreement with reference data, what tell us that the walls are acting as expected.

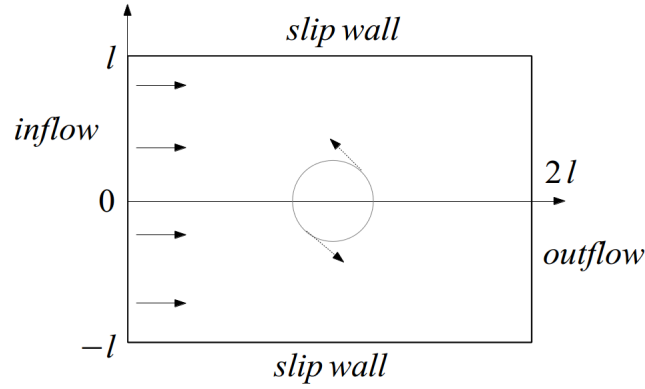


Figure 3.5: Configuration for two-dimensional test: vortex propagating through sub-sonic outlet.

3.4.4 Flow over a circular cylinder

In this section, boundary conditions are tested in a more complex problem. A three-dimensional turbulent compressible flows around a circular cylinder on an unstructured grid is simulated. In this test we can verify that a mass flow specified at an inlet is kept at the desired value even with disturbances in the flow travel upstream. The turbulent structures can leave the domain without reflections though outlets. Additionally, wall behavior is as expected.

The geometry used for this test is depicted in figure 3.9. First, the objective of this test is not to obtain very accurate results concerning the flow phenomenology, but to solve the treatment of the boundary conditions. This is the reason why a coarse mesh is used. A total of $53k$ triangles are placed in a $15d \times 10d$ computational domain, where d is the cylinder diameter. The grid is clustered along the cylinder wall and triangle size grows when approaching boundaries (which is a common configuration in typical simulations). A fixed mass flow is prescribed at the inlet, an outlet is set at the right boundary, and slip walls are used for lateral boundaries. A non-slip wall is used at the cylinder surface. The physical selected magnitudes are $Re = 3900$ and $Ma = 0.2$. Reference data exists for this case, since it has been subject of numerous studies, like in [8]. The flow is initialized with the inlet conditions and, after a short transitional state, the flow achieves a statistical stationary behavior due to the low-Reynolds configuration with a regular vortex shedding at a frequency of $St = 0.2$.

Figure 3.10 show a sequence of vorticity contour fields for the test configuration.

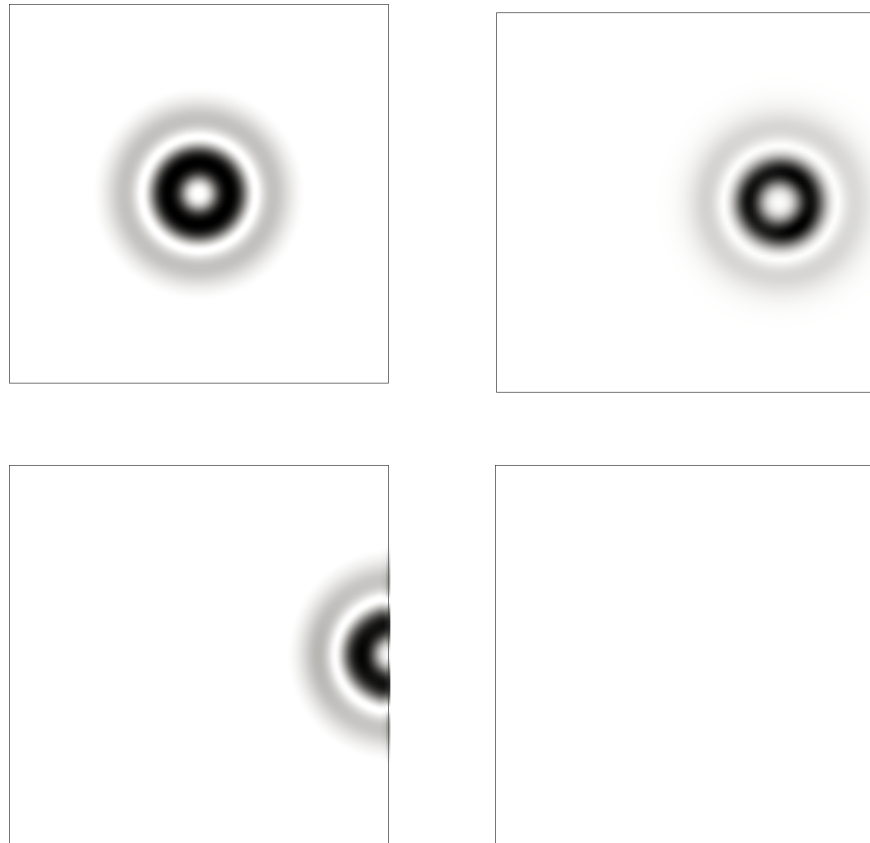


Figure 3.6: Vorticity contours (maximum value of 0.02) for the 2D vortex initial condition (top left, $t = 0$), leaving the domain (top right, $t = 0.5$, and bottom left, $t = 1$) and after leaving the domain (bottom right, $t = 2$). No reflections are observed.

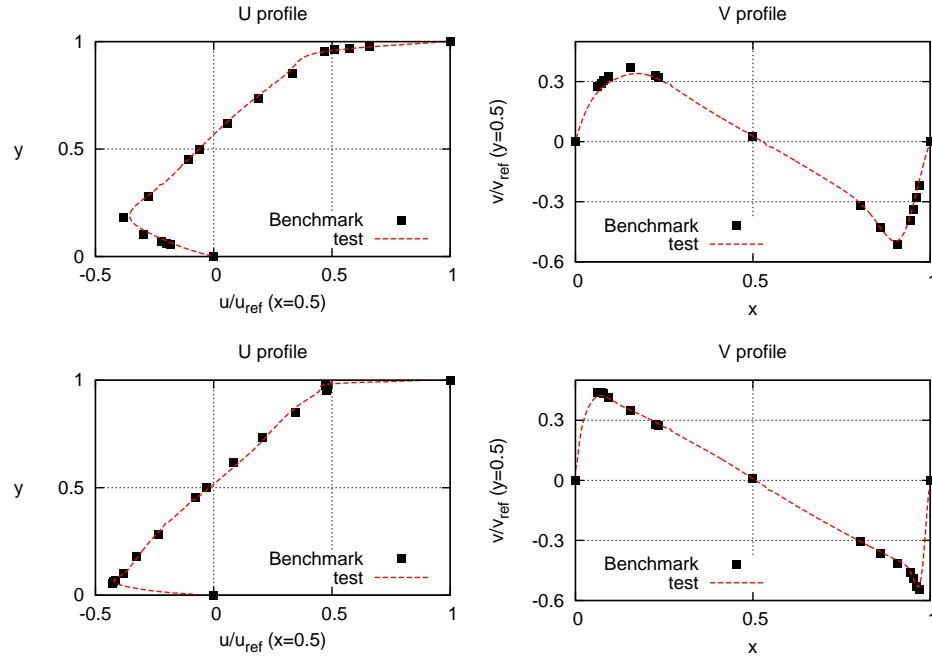


Figure 3.7: Driven cavity velocity profiles at $Re = 10^3$ (top) and $Re = 10^4$ (bottom) and $Ma = 0.3$.

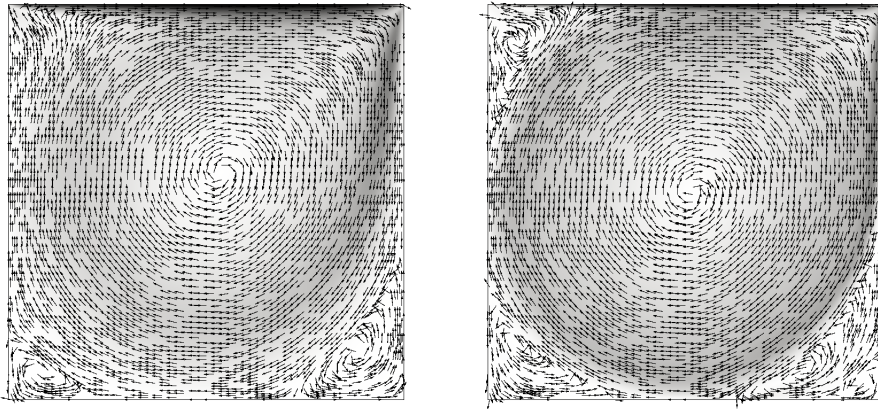


Figure 3.8: Driven cavity velocity fields at $Re = 10^3$ (left) and $Re = 10^4$ (right) and $Ma = 0.3$.

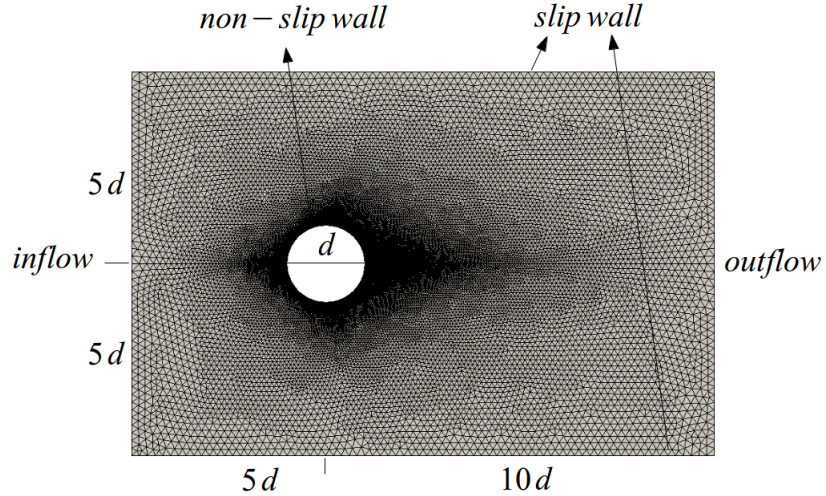


Figure 3.9: Mesh geometry and boundary conditions for the circular cylinder test.

A value of 2 is shown for the vorticity contour in order to detect any reflection at the outlet. As it can be seen, the three-dimensional turbulent structures leave the domain without reflection towards the computational domain, showing the good performance of the implemented boundary conditions.

As a final note, all the cases presented in chapter 2 and the following chapters of this thesis were performed with satisfactory results using the boundary conditions developed here.

3.5 Conclusions

A new methodology for prescribing boundary conditions has been presented. They differ from the common approach in the sense that they have been developed for the finite volume framework instead of finite difference. Ghost cells are defined outside the domain in order to impose boundary conditions weakly through fluxes as opposite of prescribing boundary conditions directly at boundary face nodes. The boundary conditions presented provide non-reflecting inflow and outflow conditions that maintain the mean imposed velocity and pressure, yet substantially eliminating spurious acoustic wave reflections, even with non-dissipative schemes. The main advantage of the method is that by using the three dimensional wave structure there is no

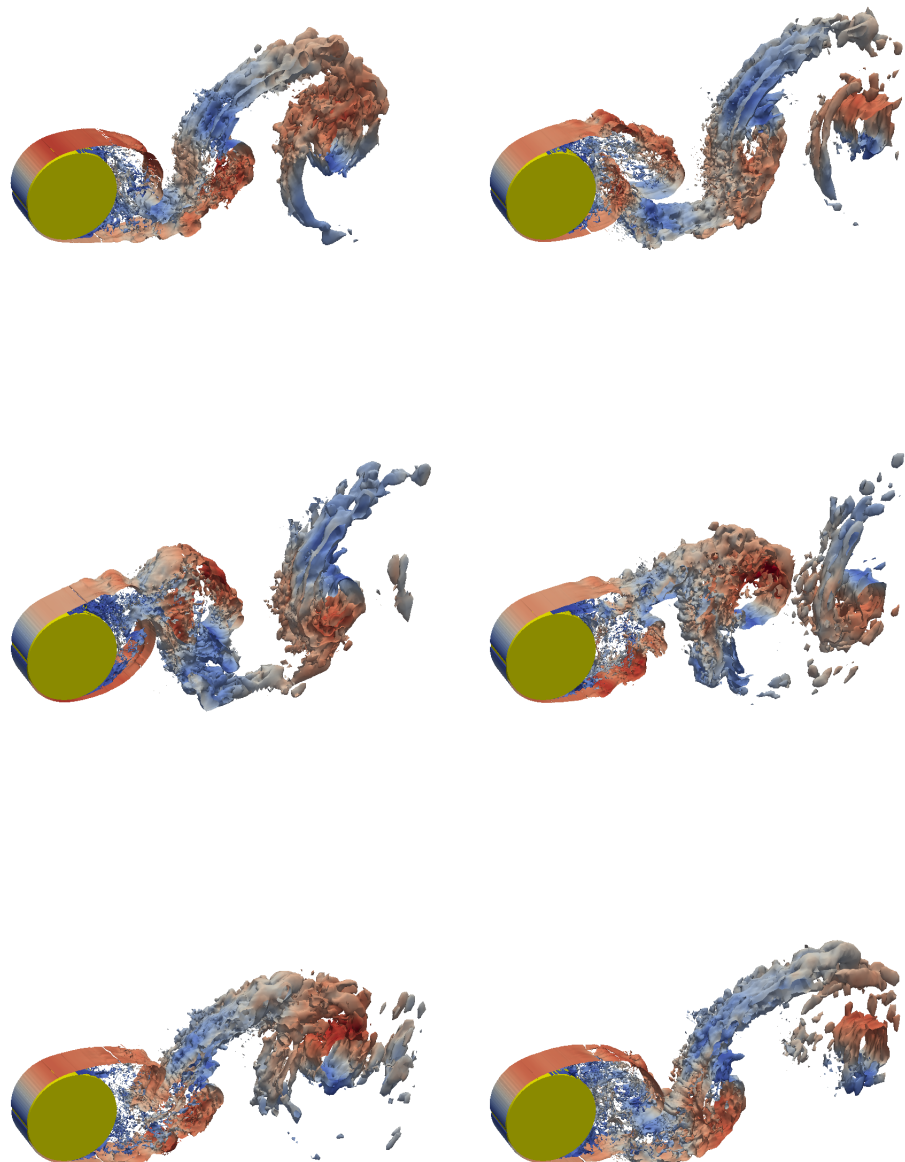


Figure 3.10: Time sequence of the vorticity contour fields for the circular cylinder problem at $Re = 3900$ and $Ma = 0.2$ (from top-left to bottom-right) each 2 time units for a total of 10 time units (around two complete shear stress periods).

need for transverse terms and several boundary conditions can coexist in the same control volume without requiring special treatment (such as corners and edges).

Different configurations have been tested in order to evaluate the presented methodology. An acoustic pulse is set in a steady flow and its temporal evolution is explored. Waves reflect on walls, while being able to leave the computational domain through outlets without significant reflection. A two-dimensional vortex convected in a freestream is also simulated. The vortex was able to leave through the outlet without reflections or vortex distortion. The driven cavity problem was solved at different Reynolds numbers in order to evaluate boundary conditions behavior. Results compare very well with benchmark data. Finally, a subsonic flow over a circular cylinder is simulated in order to evaluate boundary conditions performance in a three-dimensional turbulent case, more similar to the type of applications that lie within the objectives of this thesis. Results show how inlet mass flow is conserved at the desired value, turbulence structures are able to leave the domain without reflections, and vortex structures created behind the cylinder match with reference studies. Even when the boundaries are placed really close to the object, they perform well without reflections (similar cases usually place the boundaries much far away to avoid undesired interactions).

The boundary conditions presented in this section have been used in all the simulations in the framework of this research (and others). In the previous and next chapters a variety of problems will support the well-behavior of the boundary conditions. They also demonstrate to be effective for subsonic and supersonic turbulent flows, even with shocks reflections in walls, and allowing shocks to leave the domain through outlets.

References

- [1] T J. Poinsot and S K. Lele. Boundary Conditions for Direct Simulations of Compressible Viscous Flows. *J. Comput. Phys.*, 101:104–29, 1991.
- [2] G. Lodato, F. Ham, and H. Pitsch. Subsonic characteristic outflow boundary conditions with transverse terms: a comparative study. *Center for Turbulence Research, Annual Research Briefs*:135–48, 2010.
- [3] C. S. Yoo, Y. Wang, and A. TrouvÃ© abd H. G. Im. Characteristic boundary conditions for direct simulations of turbulent counterflow flames. *Combust. Theor. Model*, 9:617–646, 2007.
- [4] G. Lodato, P. Domingo, and L. Vervisch. Three-dimensional boundary conditions for direct and large-eddy simulation of compressible viscous flows. *J. Comput. Phys*, 227:5105–48, 2010.

- [5] V. Granet, O. Vermorel, T. Leonard, L. Gicquel, and T. Poinsot. Comparison of nonreflecting outlet boundary conditions for compressible solvers on unstructured grids. *AIAA J.*, 48(10):2348–64, 2010.
- [6] S. Scott Collis. Discontinuous galerkin methods for turbulence simulation. *Center for Turbulence Research.*, Conference Paper., 2002.
- [7] Axel Rohde. Eigenvalues and eigenvectors of the Euler equations in general geometries. *AIAA*, 2609, 2001.
- [8] D. A. Lysenko, I. S. Ertesvag, and K. E. Rian. Large-eddy simulation of the flow over a circular cylinder at reynolds number 3900 using the openfoam toolbox. *Flow Turbul. Combust.*, 89:491–518, 2012.

Turbulence modeling for discontinuous turbulent compressible flows.

4.1 Introduction

At this point, a numerical scheme valid for the simulation of turbulent compressible flows, with or without shocks, has been presented and tested in several academic cases. The next step consists of moving towards turbulent flows with strong interactions between shocks, boundary layers and turbulent structures, e.g. transonic and supersonic flows over aircraft, engine intakes or blade cascades. These kind of applications are characterized by high Reynolds and high Mach numbers. Turbulent structures are very small and boundary layers very thin, which results in unfeasible grids sizes. Therefore, turbulence modeling is required to allow such simulations. In this chapter we first review DNS and LES applications that can be found in the scientific literature. Afterwards, turbulence modeling is introduced for compressible flows, and RANS and LES are applied for the same problem. With all these, we aim to demonstrate the ability of the proposed hybrid method to resolve turbulent flows with shock/boundary-layer interactions (SBLIs) by means of DNS and turbulent modeling. As an example of turbulent compressible flow with SBLIs, the Sajben transonic diffuser is solved. This is a well known problem that presents all the features of a turbulent flow with discontinuities and SBLIs. Furthermore, available experimental and numerical data will be useful in the method validation. Finally, wall modeling is also discussed as a step forward in the cost reduction of the proposed methodology.

4.2 State of the art

Let's start by reviewing previous works on the subject following the excellent state-of-the-art by Pirozzoli [1]. There are numerous applications of the methods of computational gasdynamics to the analysis of flow physics. Here we only highlight recent high-fidelity simulations of flows involving the interaction of shock waves with turbulence. The simplest setting consists of the interaction of a (nominally) normal shock wave with a field of isotropic turbulence. Canonical shock/turbulence interactions were first investigated through DNS by Lee et al. [2], using a hybrid compact/ENO scheme. LES of the same problem was performed by Ducros et al. [3], by means of a characteristic-based nonlinear filtering scheme. The problem was revisited by Larsson & Lele [4], who carried out high-resolution calculations using a hybrid central WENO discretization with convective splitting. Substantial efforts in the past few decades have been devoted to the analysis of SBLIs [5]. The first DNS study of SBLI was reported by Adams [6], who investigated the flow over a 18° ramp at free-stream Mach number $Ma = 3$, using Adams & Shariff [7] hybrid compact/ENO method. DNS of a 24° compression ramp configuration at $Ma = 2.9$ was performed by Wu & Martín [8], using Taylor et al. [9] bandwidth-optimized WENO algorithm. LES of the supersonic ramp flow was carried out by Rizzetta et al. [10], using Visbal & Gaitondes [11] adaptive filtering technique, and by von Kaenel et al. [12], using Adams Stolz [13] regularization method. Another frequently used prototype SBLI consists of the reflection of an oblique shock wave from a flat plate at which a boundary layer is developing. The first LES of impinging shock interaction was performed by Garnier et al. [14], who used a baseline central fourth-order discretization augmented with a nonlinear WENO filter, with its local activation controlled by the Ducros sensor. Pirozzoli & Grasso [15] carried out a DNS study with flow conditions similar to Garnier et al., using a seventh-order WENO scheme. LES of the impinging shock interaction has also been performed by Touber & Sandham [16]. Their numerical method relied on a baseline SHOEC scheme, and shock-capturing was achieved through a TVD-based filter controlled by the Ducros sensor. Sample results of Touber & Sandham calculations compared against reference experimental data [17]. Overall, the LES results are in very good agreement with experimental PIV data, with the most apparent difference being the size of the separation bubble. However, the boundary layer thickening is well captured, as well as the amplification of the Reynolds shear stress past the interaction zone, which is associated with the shedding of vortices. SBLIs also occur under transonic conditions. Sandham et al. [18] performed the first LES of transonic SBLI over a circular-arc bump using the SHOEC scheme with nonlinear TVD filtering. Pirozzoli et al. [19] have recently reported DNS results of transonic SBLI at $Ma = 1.3$ over a flat plate using a hybrid discretization of the convective fluxes, whereby smooth flow regions are handled by means of conservative sixth-order central discretization of the split convective form,

and shock waves are captured through a fifth-order WENO scheme, with the switch based on the modified Ducros sensor. Results show the 3D nature of the lambda-like shock pattern, whereby the vortical structures in the incoming boundary layer cause the spanwise wrinkling of the upstream compression fan. Numerous hairpin-shaped vortex loops, resembling those found in incompressible boundary layer DNS, are observed both in the upstream boundary layer and past the interacting shock. The turbulent mixing resulting from the injection of an underexpanded sonic jet in a supersonic cross-flow was studied by Kawai & Lele [20] by means of LES. The authors used the artificial viscosity method in Kawai & Leleâs [21] version, employing sixth-order compact approximations of the spatial derivatives, coupled with eighth-order low-pass filtering. The flow visualizations demonstrate the capability of the numerical method to capture the front bow shock, the upstream separation shock, the barrel shock, and the Mach stem, all without spurious wiggles, and at the same time to accurately resolve a broad range of turbulence scales. Low-dissipative shock-capturing methods have also been used by Hill et al. [22] to analyze Richtmyer-Meshkov instability with reshock. The authors used a DRP-like central approximation of the equations in convective split form in smooth regions and switched to the tuned-WENO scheme of Hill & Pullin [23] near shock waves. The switch is controlled by the local curvature of the pressure and density field, in a fashion similar to the Jameson sensor. Many other applications of low-dissipative shock-capturing algorithms are collected in the review paper by Ekaterinaris [24].

The vast majority of the aforementioned applications use high-order schemes on structured grids. Here, we are restricted to low-order schemes on unstructured meshes. We will explore in the next sections how our hybrid scheme performs on such problems and how turbulent models are introduced in the compressible formulation.

4.2.1 More on SBLIs

Shock/boundary-layer interaction (SBLI) phenomena is present in a wide range of practical problems, such as transonic airfoils (see figure 4.1(a)) and wings, supersonic engine intakes (see figure 4.1(b)), diffusers of centrifugal compressors and turbomachinery cascades. Such interactions can be produced if the slope of the body surface changes producing a sharp compression of the flow near the surface as occurs, for example, at the beginning of a ramp or a flare, or at the front of an isolated object attached to a surface such as a vertical fin. If the flow is supersonic, a compression of this sort usually produces a shock wave originated in the boundary layer. This has the same effect on the viscous flow as an impinging wave coming from an external source. In the transonic regime, shock waves are formed at the downstream edge of embedded supersonic regions, where these shocks come close to the surface, thus, an SBLI is produced [25]. In any SBLI, the shock imposes an intense adverse pressure

gradient on the boundary layer, causing it to thicken and usually leading to boundary layer detachment. In either case, this increases the viscous dissipation within the flow. Frequently, SBLIs are also the cause of flow unsteadiness. On transonic wings, they increase the drag and they have the potential to cause flow unsteadiness and buffet. They increase blade losses in gas-turbine engines, and complicated boundary-layer control systems must be installed in supersonic intakes to minimize the losses that they cause either directly by reducing the intake efficiency or indirectly because of the disruption they cause to the flow entering the compressor. These systems add weight to aircraft and extract energy to the flow. In hypersonic flight, SBLIs can be disastrous because at high Mach numbers, they have the potential to cause intense localized heating that can be severe enough to destroy a vehicle. In the design of scramjet engines, the SBLIs that occur in the intake and in the internal flows can limit the range which vehicles using this form of propulsion can be deployed successfully.

Studies on SBLI have been performed for over 70 years [26]. First, experiments in high-speed tunnels were conducted in order to evaluate SBLI importance and its interaction with solid elements. One example is the work by Sajben's group. [27,28]. Measurements of the streamwise velocity component in unsteady separated flow-fields in a two-dimensional transonic diffuser were obtained via laser doppler velocimeter [27]. Also, pressure profiles along the diffuser walls were measured in different flow configurations [28] in order to evaluate characteristic frequencies on the flow oscillations. This data is used in the present study to compare against our results. Numerical studies first appear in the late 80s [29], but they were restricted to one- or two-dimensional inviscid models. Confined flows can present several flow features depending on the strength of the SBLI (usually defined by the Mach number at the shock wave). The boundary layer growth due to the SBLI can result in shock trains (see figure 4.1(c) and (d)), a succession of shock waves forming along the fluid and moving upstream. This phenomenon is useful in supersonic engines intakes, for example, because the fluid pressure increases after each shock (we want high pressures at the combustion chamber). On the other hand, in nozzles (see figure 4.1(e)) strong SBLIs result in flow detachment and flow asymmetries harming engine performance. This is the most challenging type of problem we can face, in which we can see a discontinuous turbulent flow with SBLI, flow transition and detachment, shock-turbulence interaction, etc.

4.3 Turbulence modeling

With advances in computer technology and the development of suitable numerical algorithms, computation of SBLI has become feasible [30].

Direct numerical simulation (DNS), with the advantages of resolving all scales of

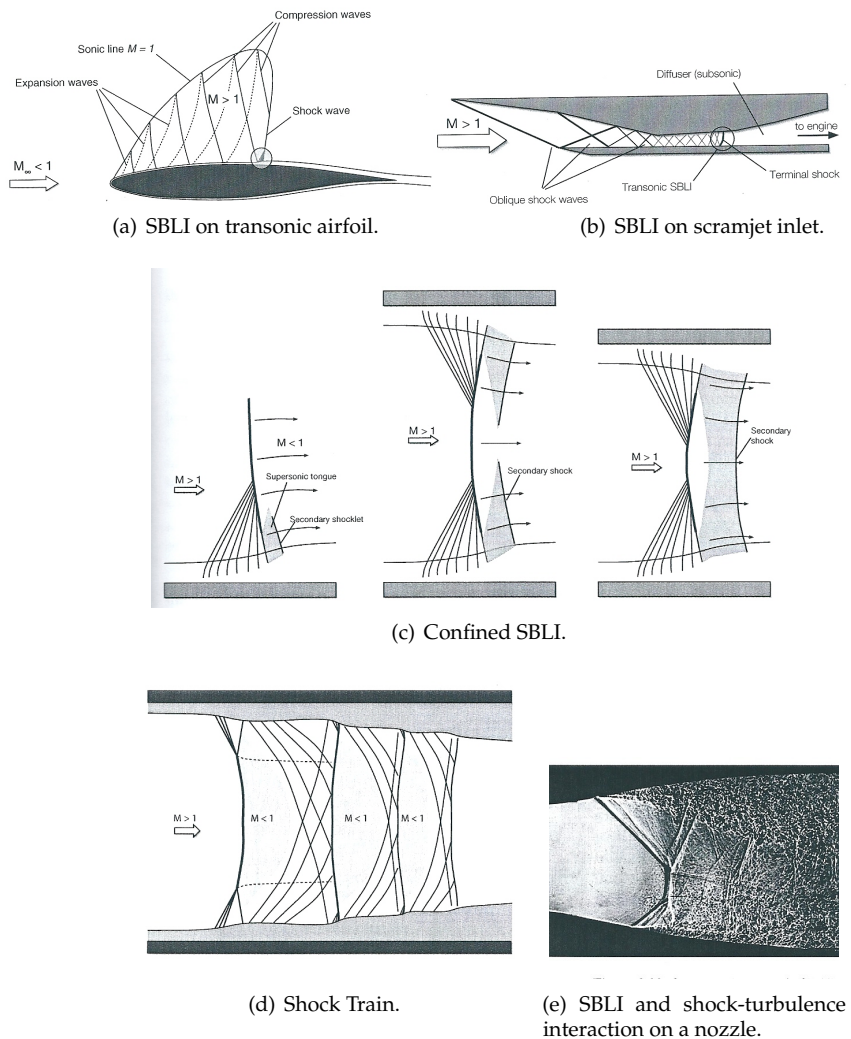


Figure 4.1: SBLI examples extracted from [25].

fluid motion, has been adopted for the study of several simplified problems. Nevertheless, the application of DNS to high-speed, high-Reynolds turbulent flows in complex geometries is still prohibitive in most cases. The Reynolds Averaged Navier Stokes (RANS) approach has been widely used to overcome DNS restrictions. It allows less expensive simulations, since turbulence is not directly resolved, introducing the need of turbulence modeling [31]. However, the averaging procedure leads to extra correlations that appear throughout the equations of motion, and turbulence modeling must close these new unknowns [32]. However, such approach may lead to unsatisfactory predictions of flows with significant SBLI. Discrepancies can be attributed to various deficiencies in the models, such as a failure to resolve anisotropy of the normal stresses. It is also a concern that steady state solvers will be in error if the flow is naturally unsteady and the shock location oscillates. On the other hand, Large Eddy Simulation (LES) solve the largest scales of motion and model the smallest non-resolved scales, resulting in a less-demanding approach than DNS that can overcome the inherent problems of the RANS approach (but at higher computational cost). Hence, LES seems to be a perfect candidate to carry out computations of high-Reynolds, high-speed turbulent flows with SBLI. LES have been extensively developed for incompressible flows, and the compressible approach usually consists of an extension of existing models [33]. LES has not been widely applied to shock/boundary-layer interaction problems [18]. Therefore, its performance is an issue of increasing interest.

The considered turbulence models are compressible extensions of existing incompressible models, implemented in the in-house software TermoFluids [34]. They have been tested in several cases, such as the flow over a NACA0012 airfoil [35, 36] and a circular cylinder [37]. The considered turbulence models are selected taking into account their simplicity and good computational performance. Concerning RANS models, the Spallart-Allmaras (SA) model is studied. The compressible solver implemented in TermoFluids takes into account the transient terms of the fluid equations, so strictly speaking we refer to the RANS approach as Unsteady RANS, or URANS. On the LES side, the Smagorinsky (SMG), the Wall Adaptative Large Eddy (WALE) and the Variational Multiscale (VMS) models are compared. Our objective is to study how to address the extra terms arising from the equations of motion and how to deal with transport equations for URANS. The proposed compressibility corrections in the literature are tested and the performance of the different methods on the Sajben transonic diffuser in terms of prediction of shock position, pressure distribution along the walls and velocity profiles through the diverging part is quantified. In addition, other aspects such as shock wave oscillation have also been studied qualitatively.

4.3.1 RANS

Compressible Navier-Stokes Equations

The conservative form of continuity, momentum and energy equations can be written as:

$$\rho_t + \nabla \cdot (\rho \mathbf{u}) = 0 \quad (4.1)$$

$$(\rho \mathbf{u})_t + \nabla \cdot (\rho \mathbf{u} \mathbf{u}) = \nabla \cdot \boldsymbol{\tau} - \nabla p \quad (4.2)$$

$$E_t + \nabla \cdot (H \mathbf{u}) = \nabla \cdot (\mathbf{u} \cdot \boldsymbol{\tau}) - \nabla \cdot \mathbf{q} \quad (4.3)$$

where ρ is the fluid density, $\mathbf{u} = (u_1, u_2, u_3)$ is the velocity vector referred to the coordinate system $\mathbf{x} = (x_1, x_2, x_3)$, p is the pressure, and E is the total energy. The subscript $(\cdot)_t$ refers to the time derivative $\partial/\partial t$. The fluid total enthalpy is $H = E + p$. The viscous stress tensor is defined as,

$$\boldsymbol{\tau}_{ij} = 2\mu(S_{ij} - \frac{1}{3}S_{kk}\delta_{ij}) \quad (4.4)$$

where μ is the fluid viscosity and $S_{ij} = \frac{1}{2}(\frac{\partial u_i}{\partial x_j} + \frac{\partial u_j}{\partial x_i})$. Finally, $\mathbf{q} = -\kappa \nabla T$ is the heat flux, where $\kappa = \frac{\mu c_p}{Pr}$ and T is the temperature.

In the present study the working fluid is air with the ideal gas hypothesis, with $\gamma = 1.4$, $c_p = 1004 \text{ J kg}^{-1} \text{ K}^{-1}$, and $Pr = 0.72$.

$$E = \frac{p}{\gamma - 1} + \frac{1}{2}\rho \mathbf{u} \cdot \mathbf{u} \quad (4.5)$$

The systems of equations are closed with the equation of state,

$$p = \rho R_g T \quad (4.6)$$

being $R_g = 287 \text{ [J kg}^{-1} \text{ K}^{-1}]$. The viscosity is computed with the Sutherland's law,

$$\mu = 1.461^{-6} \frac{T^{3/2}}{110.3 + T} \quad (4.7)$$

URANS Formulation

In order to mass average in time the conservation equations 4.1 to 4.3, flow variables are decomposed in mean and fluctuating parts. The result of the substitution are the Favre-averaged equations:

$$\bar{\rho}_t + \nabla \cdot (\bar{\rho} \tilde{\mathbf{u}}) = 0 \quad (4.8)$$

$$(\bar{\rho} \tilde{\mathbf{u}})_t + \nabla \cdot (\bar{\rho} \tilde{\mathbf{u}} \tilde{\mathbf{u}}) = \nabla \cdot (\bar{\boldsymbol{\tau}} - \bar{\rho} \tilde{\mathbf{u}}'' \tilde{\mathbf{u}}'') - \nabla \bar{p} \quad (4.9)$$

$$\bar{E}_t + \nabla \cdot (\bar{H}\tilde{\mathbf{u}}) = \nabla \cdot (\tilde{\mathbf{u}}(\bar{\tau} - \bar{\rho}\mathbf{u}''\mathbf{u}'')) - \nabla \cdot (\bar{\mathbf{q}} + \bar{\mathbf{u}''H''} - \bar{\tau}\mathbf{u}'' + \bar{\rho}\mathbf{u}''k) \quad (4.10)$$

$$\bar{p} = \bar{\rho}R_g\tilde{T} \quad (4.11)$$

where $\bar{\phi}$ refers to the time-averaged dependent variable ϕ , and $\tilde{\phi} = \bar{\rho\phi}/\bar{\rho}$ is its Favre average. Equations 4.8, 4.9 and 4.11 differ from their laminar counterpart only by the appearance of the Favre-averaged Reynolds-stress tensor, $\tau_T = -\bar{\rho}\mathbf{u}''\mathbf{u}''$. Several terms appear in equation 4.10, the turbulent transport of heat $\mathbf{q}_T = \bar{\mathbf{u}''H''}$, the molecular diffusion $\bar{\tau}\mathbf{u}''$ and the turbulent transport of turbulent kinetic energy $\bar{\rho}\mathbf{u}''k$. The definition of the total energy is also modified, $\bar{E} = \frac{\bar{p}}{\gamma-1} + \frac{1}{2}\bar{\rho}\tilde{\mathbf{u}}\tilde{\mathbf{u}} + \bar{\rho}k$.

The closure approximations used in the present study are [31]:

$$\tau_T = 2\mu_T(S_{ij} - \frac{1}{3}S_{kk}\delta_{ij}) - \frac{2}{3}\bar{\rho}k\delta_{ij} \quad (4.12)$$

$$\mathbf{q}_T = -\frac{\mu_T c_p}{Pr_T} \nabla \tilde{T} \quad (4.13)$$

The molecular diffusion and the turbulent transport of turbulent energy are approximated together as follows:

$$\bar{\tau}\mathbf{u}'' - \bar{\rho}\mathbf{u}''k = (\mu + \frac{\mu_T}{\sigma_k})\nabla k \quad (4.14)$$

Although this term is only relevant for hypersonic flows. The problem reduces, therefore, to the computation of the eddy viscosity μ_T .

Spalart-Allmaras Model

In the present work, the Spalart-Allmaras model is chosen to calculate the eddy viscosity. According to [38], the differential equation is derived by using empiricism and arguments of dimensional analysis, Galilean invariance and selected dependence on the molecular viscosity. This model does not require finer grid resolution than one required to capture the velocity field gradients with algebraic models. The transport equation for the working variable \hat{v} is given by:

$$\hat{v}_t + \nabla \cdot (\nu \hat{\mathbf{u}}) = c_{b1}\hat{S}\hat{v} + \frac{1}{\sigma} [\nabla((\nu + \hat{v}) \cdot \nabla \hat{v} + c_{b2}\nabla \hat{v} \cdot \nabla \hat{v}] - c_{w1}f_w \left(\frac{\hat{v}}{d} \right)^2 \quad (4.15)$$

The eddy viscosity is defined as

$$\mu_T = \bar{\rho}\hat{v}f_{v1} \quad (4.16)$$

where, the damping function f_{v1} is defined as:

$$f_{v1} = \frac{\chi^3}{\chi^3 + c_{v1}^3} \quad (4.17)$$

with $\chi = \frac{\hat{v}}{v}$.

$$\hat{S} = \sqrt{2S_{ij}S_{ij}} + \frac{\hat{v}}{\kappa^2 d^2} f_{v2} \quad (4.18)$$

being $f_{v2} = 1 - \frac{\chi}{1+\chi f_{v1}}$. In order to obtain a faster decaying behaviour of destruction in the outer region of the boundary layer, a function f_w is used:

$$f_w = g \left(\frac{1 + c_{w3}^6}{g^6 + c_{w3}^6} \right)^{1/6} \quad (4.19)$$

where $g = r + c_{w2}(r^6 - r)$ acts as a limiter that prevents large values of f_w and $r = \frac{\hat{v}}{\hat{S}\kappa^2 d^2}$. Constants models are, $c_{b1} = 0.1355$, $c_{b2} = 0.622$, $\sigma = 2/3$, $\kappa = 0.41$, $c_{w1} = \frac{c_{b1}}{\kappa^2} + \frac{1+c_{b2}}{\sigma}$, $c_{w2} = 2$ and $c_{v1} = 7.1$. Since the Spalart-Allmaras method does not involve the transport of turbulent kinetic energy, k is not available for the Favre-averaged equations with this turbulent model.

Extension To Compressible Flow

The first thing to take into account on the extension of the SA model to compressible flows is to use $\bar{\rho}\hat{v}$ instead of \hat{v} as working variable, in order to solve the transoport equation in conservative form.

$$(\bar{\rho}\hat{v})_t + \nabla \cdot (\bar{\rho}\hat{v}\mathbf{u}) = c_{b1}\hat{S}\bar{\rho}\hat{v} + \frac{1}{\sigma} [\nabla((\mu + \bar{\rho}\hat{v}) \cdot \nabla\hat{v} + c_{b2}\nabla\hat{v} \cdot \nabla\hat{v})] - c_{w1}\bar{\rho}f_w \left(\frac{\hat{v}}{d} \right)^2 \quad (4.20)$$

Catris and Aupoix [32] suggest to use $\sqrt{\bar{\rho}}\hat{v}$ as diffused quantity, nevertheless this strategy complicates the numerical implementation. An alternative form of 4.20 can be found in [39], and it involves only the computation of $\nabla\bar{\rho}\hat{v}$ which appears in the source term.

$$(\bar{\rho}\hat{v})_t + \nabla \cdot (\bar{\rho}\hat{v}\mathbf{u}) = c_{b1}\hat{S}\bar{\rho}\hat{v} + \frac{1}{\sigma} [\nabla((\mu + \bar{\rho}\hat{v}) \cdot \nabla\hat{v} + c_{b2}\nabla\hat{v} \cdot \nabla\bar{\rho}\hat{v})] - c_{w1}\bar{\rho}f_w \left(\frac{\hat{v}}{d} \right)^2 \quad (4.21)$$

Both formulations, conservative and conservative corrected respectively, are tested and compared against the original incompressible version 4.15, referred as non-conservative.

4.3.2 LES

In LES the contribution of the large, energy-carrying structures to momentum and energy transfer are computed exactly and only the effect of the smallest scales of turbulence are modeled. While a substantial amount of research has been carried out into modeling for the LES of incompressible flows, applications to compressible flows have been significantly fewer, due to the increased complexity introduced by the need to solve an energy equation, which introduces extra unclosed terms. Furthermore, the form of the unclosed terms depends on the chosen energy equation [40]. To obtain the equations governing the motion of the resolved eddies, we must separate the large scales from the small ones. LES is based on the definition of a spatial filter operator:

$$\bar{f}(x) = \int_D f(x') G(x, x'; \bar{\Delta}) dx' \quad (4.22)$$

where D is the entire domain, G is the filter function, and $\bar{\Delta}$ is the filter-width associated with the wavelength of the smallest scale retained by the filtering operation. Thus, the filter function determines the size and structure of the solved scales. In compressible flows it is convenient to use Favre-filtering, as in the URANS equations, to avoid the introduction of SGS terms in the equation of conservation of mass. Applying the Favre-filtering operation, we obtain a system of equations similar to 4.8 to 4.11.

The Smagorinsky model

The compressible version of the Smagorinsky model was proposed in [41],

$$\mu_t = f_{vd} C_R \bar{\rho} \bar{\Delta}^2 \sqrt{\tilde{S}_{mn} \tilde{S}_{mn}} \quad (4.23)$$

with $C_R = 0.01$. The SGS isotropic stress tensor term is given by,

$$k = C_I \bar{\Delta}^2 \tilde{S}_{mn} \tilde{S}_{mn} \quad (4.24)$$

where $C_I = 0.0066$. The Smagorinsky model is known to fail in the inner portion of the boundary layer. This is why a van Driest damping factor is used.

$$f_{vd} = 1 - e^{(-y^+/26)} \quad (4.25)$$

The WALE model

The WALE model by Nicaud and Ducros [42] is based on the square of the velocity gradient tensor. In its formulation the SGS viscosity accounts for the effects of both,

the strain and the rotation rate of the smallest resolved turbulent fluctuations. In addition, the proportionality of the eddy viscosity near walls is recovered without any dynamic procedure,

$$\mu_t = \bar{\rho} C_w^2 \Delta^2 \frac{(\tilde{s}_{ij}\tilde{s}_{ij})^{3/2}}{(\tilde{S}_{ij}\tilde{S}_{ij})^{5/2} + (\tilde{s}_{ij}\tilde{s}_{ij})^{5/4}} \quad (4.26)$$

where $C_w = 0.325$ is a true model constant, \tilde{S}_{ij} is the strain rate tensor of the resolved field and \tilde{s}_{ij} is the traceless symmetric part of the square of the resolved velocity gradient tensor.

$$\tilde{s}_{ij} = \frac{1}{2} \left(\frac{\partial \tilde{u}_i}{\partial x_l} \frac{\partial \tilde{u}_l}{\partial x_j} + \frac{\partial \tilde{u}_j}{\partial x_l} \frac{\partial \tilde{u}_l}{\partial x_i} \right) - \frac{1}{3} \frac{\partial \tilde{u}_m}{\partial x_l} \frac{\partial \tilde{u}_l}{\partial x_m} \delta_{ij} \quad (4.27)$$

The aforementioned expressions are developed for incompressible flow, and it thus gives only μ_t . The modification is to use the relation between μ_t and k for the original Smagorinsky model in order to close the computation of the isotropic SGS tensor.

$$\tau_T = 2\mu_T(\tilde{S}_{ij} - \frac{1}{3}\tilde{S}_{kk}\delta_{ij}) - \frac{2}{3} \frac{C'_I}{\bar{\rho}} \left(\frac{\mu_t}{\Delta} \right)^2 \delta_{ij} \quad (4.28)$$

where $C'_I = 45.8$. With that we have updated the model to deal with compressible flows.

The Variational Multiscale model

In the Variational Multiscale approach three classes of scales are considered: large, small and unresolved scales. If a second filter with filter length \hat{l} is introduced (usually called test filter), a splitting of the scales can be performed,

$$f' = \bar{f} - \hat{f} \quad (4.29)$$

Neglecting the effect of unresolved scales, we only need to model the small scales. Here, we close these terms using the WALE model.

4.3.3 WMLES

Wall models for LES appear as a solution to overcome the high computational costs of full-resolved LES at high Reynolds numbers. Low-viscosity high-speed flows present small but dynamically important eddies in the near-wall region. These eddies are of the special importance in attached boundary layers and require fine grids in the near-wall regions, proportional to Re^2 (nearly the same size as for DNS), that

result in extremely low time steps. Additional problems are present for separated flows, where the boundary layer becomes a free shear layer at separation and the opposite occurs at reattachment.

The solution to this problem consists in taking advantage of the relative independence between the boundary layer and the outer simulation region, and use one as a boundary condition for the other. A coarse grid can be used to the LES of the flow with $y^+ \approx 100 - 500$ and supply the model with a correct wall shear stress via a wall model. This results in dramatic savings compared to fully resolve LES, where typically $y^+ \approx 1$.

Simple wall models for LES are analogous to the wall functions commonly used in RANS. Nevertheless, they are not successful in transition, separated flow. They work well in equilibrium flows where mean flow have a logarithmic behavior, which is not valid in complex flows, especially with separation. These models are required to produce logarithmic profile near lower boundary of domain and handle adverse and favorable pressure gradients, separation and reattachment (which is very challenging for existing models). Experience with these simple methods show a reduction in computation time by factor of 10 or more. They work well in attached flow but do not predict accurately separated flows. They work better at higher Reynolds. Among these type of methods, we explore the Werner-Wengel model.

More complex models consist in using a RANS model for the inner part of the boundary layer and couple to LES for the outer region. These approach is commonly known as hybrid LES-RANS and should have advantage of both methods: accuracy of LES and speed of RANS. Here we explore the Detached Eddy Simulation (DES) in its variant DDES.

Other methods exist but are out of the scope of this thesis.

Werner & Wengel

Simple wall models were developed from channel flow calculations. The Schumann model (1976) assumes linear relation between instantaneous streamwise velocity at first grid point off the wall and instantaneous wall shear stress.

$$\tau_{12}(x, z) = \frac{\bar{u}_1(x, y_1, z)}{U_1(y_1)} < \tau_w > \quad (4.30)$$

where the wall normal direction is y , y_1 is the first point off the wall and $< \cdot >$ represents time average. Values for $U_1(y_1)$, the mean streamwise velocity at first point off the wall have to be provided or computed. Skin friction $< \tau_w >$ should be provided (for a plane channel flow it is equal to the driving mean pressure gradient). For complex problems where $< \tau_w >$ is not known a priori, the time average is replaced by a mean over the plane parallel to the solid wall at y_1 (flow is homogeneous in planes

parallel to the wall). This is known as the Grotzbach method (1987) and allows to estimate the mean wall shear stress, $\langle \tau_w \rangle = \rho u_\tau^2$. We still need the logarithmic law. A variant of this method is the Werner-Wengle method, a more flexible and widely used method that allow to analytically evaluate the wall shear stress components from the velocity field. It assumes that instantaneous velocity components at the wall in directions parallel to the wall are in phase with the associated wall shear stresses. Instantaneous velocity profile given by a 1/7 power law rather than the logarithmic law.

$$\begin{aligned} u^+ &= y^+ & \text{if } y^+ < 11.8 \\ u^+ &= 8.3(y^+)^{1/7} & \text{if } y^+ > 11.8 \end{aligned} \quad (4.31)$$

The values of the tangential velocity components can be related to the corresponding values of the wall shear stress components by integrating the velocity profile given above over the distance separating the first cell from the wall.

Hybrid RANS/LES

Detached Eddy Simulation (DES) is based on the idea of using RANS in the boundary layer and LES in detached region. The original version is based on the Spalart-Almaras RANS model and is fairly easy to implement if the RANS model. New versions, nevertheless, might use other RANS models such as SST, $k - \omega$, etc. Hybrid RANS/LES has the advantage of resolving time-dependent, three-dimensional turbulent motion as in LES but using RANS in the near-wall region. In this way, the problem of resolving narrow streaks that are important in the wall shear stress prediction is alleviated.

The SA based DES model is based on a modification of the length scale in the destruction term of the one equation eddy viscosity model. DES reduces to a RANS closure in the attached boundary layers (using the SA model) and to a Smagorinsky-like subgrid scale model away from the wall. Recall equation 4.15 that gives the transport equation for the turbulent eddy viscosity ν_t . The DES formulation is obtained by replacing the distance to the nearest wall, d , by \bar{d} in the production/dissipation terms and model parameters.

$$\bar{d} = \min(d, C_{DES}\Delta) \quad (4.32)$$

where $C_{DES} = 0.65$ [43]. Thus, DES switches to LES in regions where the grid spacing (in all directions) is smaller than the wall distance. Because in this latter region the more energetic turbulent eddies are generally not much smaller than the scale of the geometry, one may expect that the grid refinement necessary to obtain a much better flow description will not be exaggerated compared to RANS. Nevertheless, a further improvement can be done with a few tweaks to the model. The development of

Delayed DES (DDES), a extension of DES, has the objective of relaxing the transition between the RANS and LES models (specially troublesome on coarse meshes) [44].

$$\bar{d} = d - f_d \max(0, d - C_{DES}\Delta) \quad (4.33)$$

$$f_d = 1 - \tanh((8r_d)^3) \quad (4.34)$$

where

$$r_d = \frac{\nu_t + \nu}{\sqrt{(S_{ij}S_{ij})\kappa^2 d^2}} \quad (4.35)$$

Note that if $r_d \ll 1$ (LES region) then f_d is 1 and 0 elsewhere. Setting f_d to 0 yields RANS ($\bar{d} = d$) while setting it to 1 yields DES ($\bar{d} = \min(d, C_{DES}\Delta)$).

4.4 Numerical tests

4.4.1 Channel Flow

In order to test the LES models, the channel flow case is proposed. The channel flow test is a good candidate to study wall turbulence because it is homogeneous in two directions, avoiding uncertainties of the boundary conditions. Isothermal walls at $T_w = 500K$ are imposed in the remaining boundaries. The flow is initialized with a Pouseille function that introduces early disturbances to the flow. Once the turbulent state is achieved, average of the flow is computed in order to further evaluate turbulent statistics.

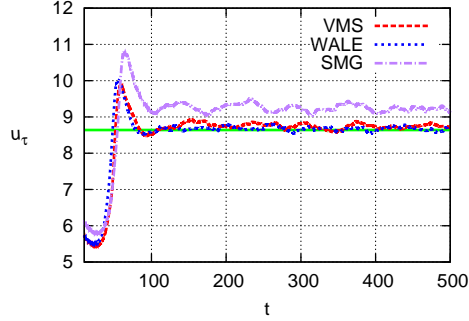
Six different cases were studied at two different compressibility regimens. First, a $Ma = 0.3$ and $Re = 2820$ (based on the bulk velocity, wall properties and channel semi-height). The turbulent channel flow was simulated in order to evaluate the LES models in the near incompressible regimen. Reference results are available for comparison: Kim et al. [45], Foysi et al. [46] and also experimental data can be found for the incompressible channel flow [47]. Afterwards, a $Ma = 1.5$ and $Re = 3000$ channel flow was studied to asses the LES performance in the supersonic regimen. Reference results are available for comparison: Coleman et al. [48] and Foysi et al. [46]. See table 4.1 for all the details.

The performance of the LES models on the compressible channel flow are explored with reference to mean profiles and second-order statistics of velocity and thermodynamic properties, compared to reference DNS and experimental data.

We begin with the analysis of mean flow properties. The time evolution of u_τ for the case M03 is depicted in figure 4.2 for the different LES models. WALE and VMS models converge well to the DNS average value (marked with solid line), while

Table 4.1: Data for the different cases.

Case	M	Re	Re_τ	L_x	L_y	L_z	N_x	N_y	N_z	Δx^+	Δy_w^+	Δz^+
M03	0.3	2820	181	12	2	6	64	64	96	19	0.5	6
KIM	0	2300	180	4π	2	2π	192	129	160	12	0.05	7
FOY	0.3	2820	181	9.6	2	6	192	129	160	9.12	1.02	6.84
M15	1.5	3000	221	12	2	6	64	64	96	19	0.5	6
COL	1.5	3000	220	4π	2	$4\pi/3$	114	119	80	19	0.1	12
FOY	1.5	3000	221	4π	2	$4\pi/3$	192	151	128	14.46	0.84	7.23

**Figure 4.2:** Time evolution of u_τ for the case M03.

the SMG model over-predicts this value. Figure 4.3 shows the law of the wall for both cases. Results show good tendency and match reference data except for the SMG model. For the subsonic case, results for the WALE and VMS models match slightly better experimental data by Eckelmann et al. [47], but they also approximate very well to the wall of the law and DNS data. The failure of the SMG model in reproducing flow mean properties is more visible. Results for the supersonic case agree with Coleman et al. [48] DNS when the WALE or VMS model are used. Again, the SMG fails in the outer boundary layer. We can see how the logarithmic law rises when the Mach number is increased. Alternative definitions of u^+ can be found in the literature, such as the Van Driest transformation, that accounts for the density variations that causes this difference.

Following with second-order statistics, the root-mean-square velocity fluctuations for the case M03 are presented in figure 4.4. All three methods give good approxima-

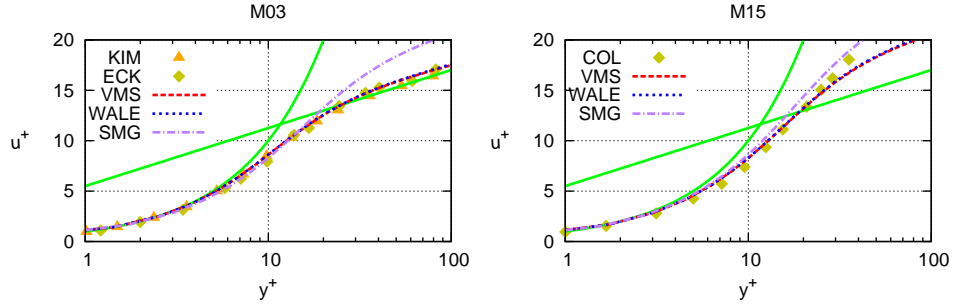


Figure 4.3: Law of the wall for the case M03 (left) and M15 (right) compared against references. For the inner boundary layer the law $u^+ = 2.5 \ln(y^+) + 5.5$ is used, meanwhile $u^+ = y^+$ is the expression for the outer boundary layer (solid lines).

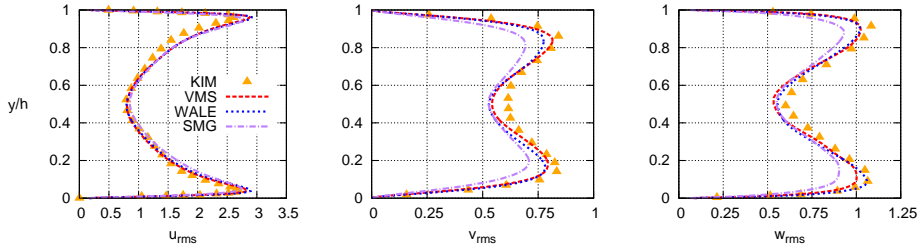


Figure 4.4: Root-mean-square velocity fluctuations for the case M03, compared to Kim et al.

tions to reference data, being VMS results slightly better and SMG the worst among the three models. Reynolds shear stresses are depicted in figure 4.5, showing that for the subsonic case the use of the WALE and SMG models mispredict the shear stress, due to energy accumulation and over-dissipation, respectively, while the use of VMS match exactly reference DNS. Concerning the supersonic case, both WALE and VMS give fairly good results, being the VMS model slightly better. The use of the SMG model results again in the shear stress over-prediction.

Finally, Q iso-contours of instantaneous fields using the VMS model are presented in figure 4.6 to evaluate near-wall turbulence structures. It can be seen how near-wall streaks are elongated and more sparsely distributed as Mach number increases.

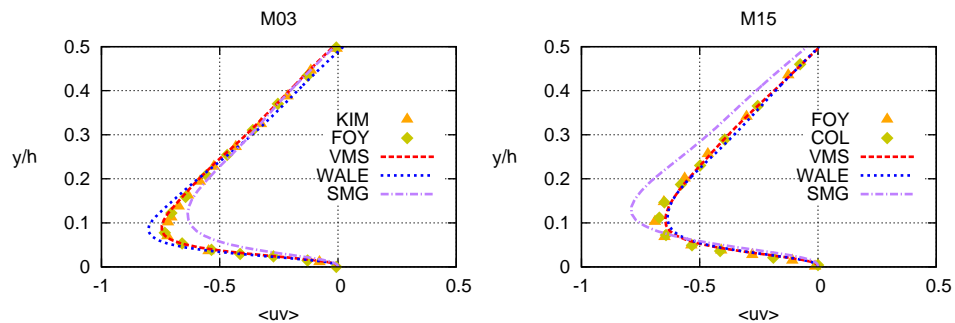


Figure 4.5: Reynolds shear stresses compared against reference data.

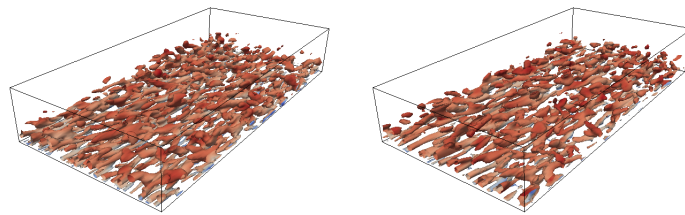


Figure 4.6: Iso-contours of $Q = 0.1$ colored by Mach number for the case M03 (left) and M15 (right).

Compressible extension of the incompressible LES models implemented in Ter-
moFluids has been carried out. Overall, the WALE and VMS models show good
performance on the compressible turbulent channel flow. The SMG model, however,
does not perform as good as the other methods. Between the WALE and VMS mod-
els, the VMS gives better solutions but results in a more expensive method in terms
of computational costs.

4.4.2 Sajben's transonic diffuser

The flow through a transonic diffuser was investigated with the numerical tools pre-
sented in this thesis. The objective is to determine the performance of the differ-
ent turbulent models and the ability of the hybrid scheme to deal with transonic
flows with SBLIs. This validation case examines the transonic air flow through a
converging-diverging diffuser with comparison to experimental data obtained by
Sajben et al. RANS, LES, DDES and WMLES were tested in two- and three-dimensional
configurations of the same diffuser at two different outlet pressures, related to the
strength of the SBLIs, weak and strong, listed in table 4.2. Pressure distributions
along the walls as well as velocity profiles and location of the shocks were compared.

Inflow		Outflow	
Total Pressure [Pa]	134447.767	Static Pressure [Pa] (weak)	110660.855
Total Temperature [K]	277.78	Static Pressure [Pa] (strong)	97216.077

Table 4.2: Flow conditions for the Sabjen's diffuser.

The two-dimensional geometry of the Sajben diffuser is shown in figure 4.7. The
throat is located at $x = 0$ and has a height of $h = 44$ millimeters. Two different
meshes were used, the first one consisting of a 200×80 and the second one of $400 \times$
 200 control volumes. Both meshes were formed by quadrilaterals clustered along
the wall at a distance $y_{wall} = 1 \times 10^{-5}$ space units to ensure well boundary layer
reconstruction. Three-dimensional studies were conducted with the same meshes
extruded in the span-wise direction with a total number of 32 planes.

We begin by examining results with the different forms of the SA model pre-
sented in section 4.3.1. Figure 4.8(a) shows that the three variants of the SA method
(non-conservative, conservative and conservative corrected) give similar results. Nev-
ertheless, when the original incompressible non-conservative formulation is used,
the shock waves is placed slightly forward to the correct position, which is well re-
produced by the two conservative formulations. Concerning the velocity profiles
in figure 4.8(b), the RANS approach is able to reproduce the bottom wall flow pat-
tern, while the top wall flow is mispredicted. This fact has in turn an effect on the
evolution of the core flow, resulting also in a small difference when compared with

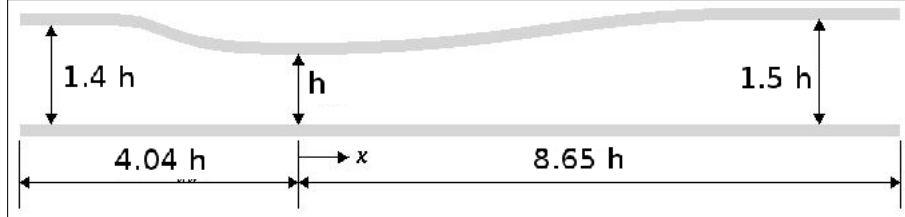


Figure 4.7: Sajben's diffuser geometry.

reference profiles. Due to the geometry and the flow conditions, the boundary layer developed at the bottom wall stays attached even after the shock-wave. On the other hand, the boundary layer developed on the top wall transitions to turbulence due to the high adverse pressure gradient and the change of the slope in the diverging zone, detaching and reattaching forming a separation bubble. It is a known fact that RANS approach is well suited for attached flows, which is true for the bottom near wall flow of our case, but fail in detached flows (hence the study and development of methods such as DES). We can see this problem in the near top wall flow, where SA is unable to well capture flow behavior. Figure 4.9 shows the same results for the strong case. Since the outlet total pressure has been diminished, the shock wave is formed closer to the outlet and hence its strength raises. Concerning pressure profiles along the walls showed on 4.9(a), again the three models behave similar. But, as happened for the weak case, the conservative models capture slightly better the shock position. Velocity profiles for the strong case can be seen in figure 4.9(b), where the features that were previously mentioned are now magnified. Bottom wall boundary layer, since it is attached along the diffuser, is well reproduced by the SA models. On the other hand, once the top wall flow detaches due to the strong adverse pressure gradient induced by the shock wave and the wall slope, the model is unable to calculate accurate average velocity profiles. In this case, since the SBLI is of strong type, the detached flow cannot reattach. Overall, the conservative models are preferred over non-conservative formulations since they give slightly better results in terms of shock positioning and, moreover, since the rest of equations are solved in conservative form it is preferred to keep the same formulation across the entire numerical model.

As it has been observed, RANS models are a good choice for attached turbulent flows. The method is cheap in terms of computational resources as long as the y^+ provided by the mesh is *good enough* ($y^+ \approx 1 - 5$). Nevertheless, if we face detached flows or three-dimensional transient effects (shock-wave formation frequency or shock trains for example), RANS models are not adequate and we have to resort to LES. We present results for the weak case in a three-dimensional configuration

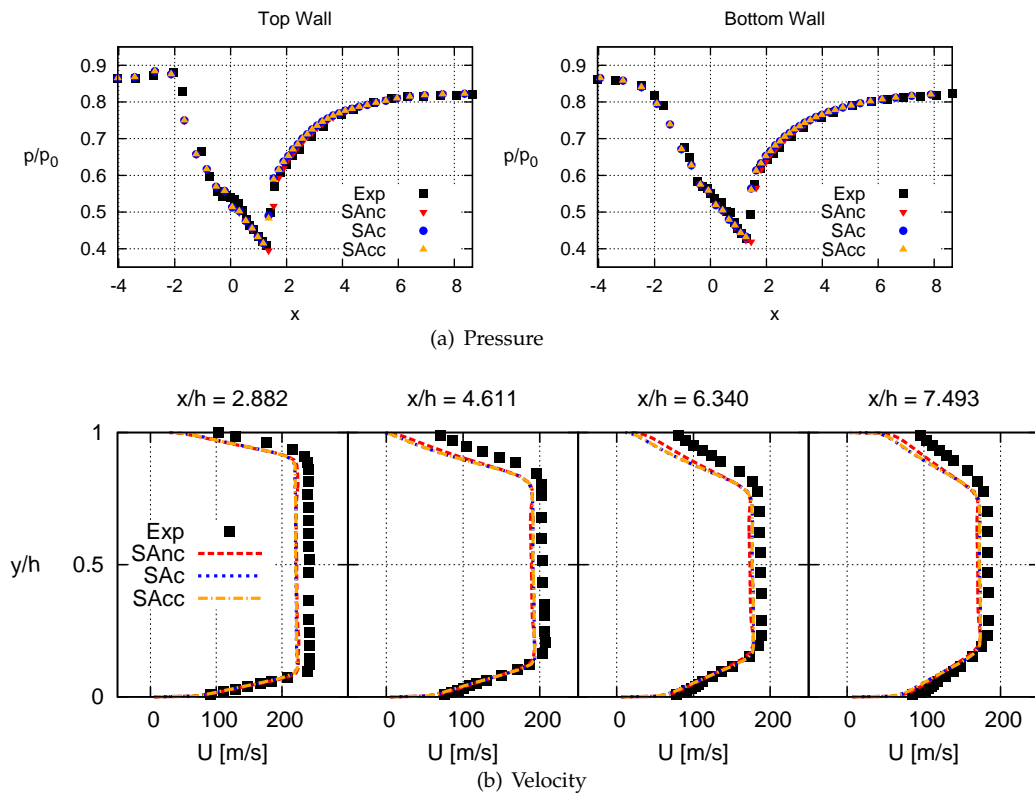


Figure 4.8: Sabjen's diffuser weak case.

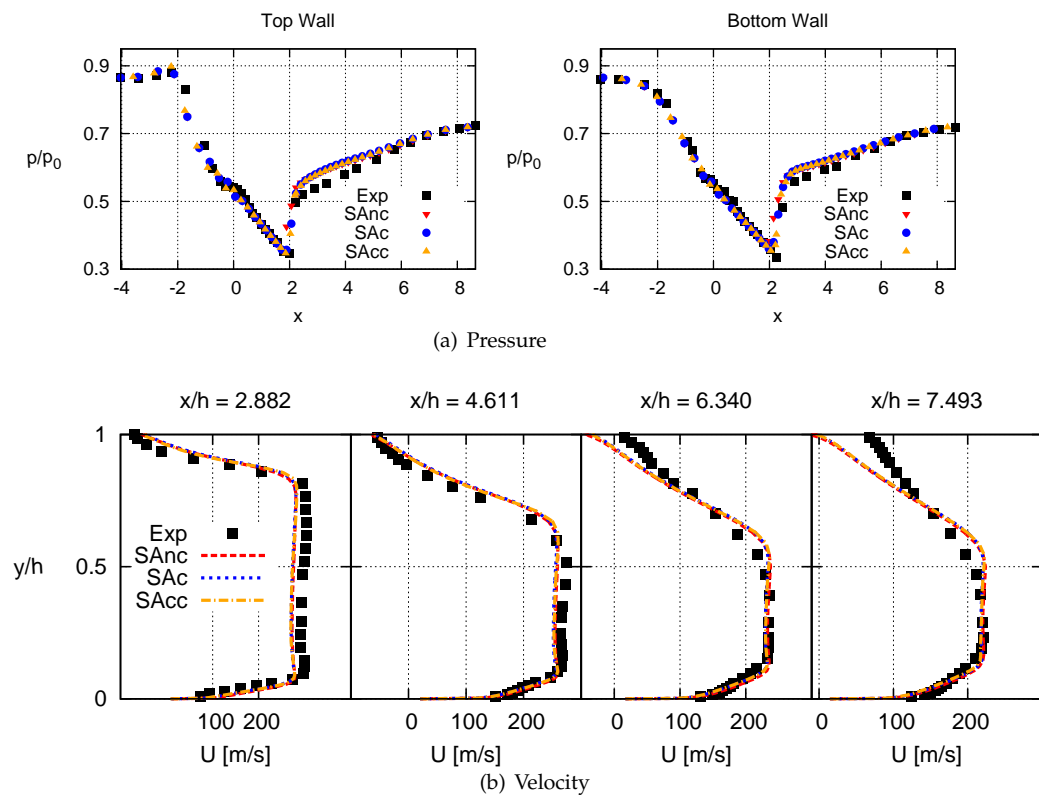


Figure 4.9: Sabjen's diffuser strong case.

in figure 4.10. In terms of wall pressure distribution and shock wave position, all the methods except LES were able to capture the right location. LES, since it is not modeling boundary layers, is unable to reproduce a viscous boundary layer, giving results similar to those obtained with Euler solvers. In order to capture a boundary layer with LES, and predict the shock wave accurately, DNS levels of precision is required. In order to overcome this issue, DDES and WMLES were tested, resulting in a good shock-wave position representation. In the case of DDES, this result is expected since the difference between LES and DDES is the use of the SA-RANS model in the boundary layer, which was identified as the main cause of problems for LES. On the other hand, the accurate prediction of the WW model it is not only surprising but also encouraging due to the simplicity and power of the method, since it does not require a y^+ as small as RANS (or DDES for that matter). Velocity profiles are depicted in figure 4.10(b) showing very interesting results. First, as previously mentioned, LES is not able to capture a boundary layer resulting in almost inviscid results. DDES results in an excessive boundary layer thickness that completely disagree with reference data. This can be due to the opened issue concerning the interaction between the RANS model and LES (which has been proved to be successful for external fluids but seems to fail in internal flows such as the flow through diffusers). Finally we can see how the introduction of the wall model allows the LES model to *see* the boundary layer resulting in much more accurate profiles, specially in the near wall regions, which in turn results in better core flow representation.

4.5 Conclusions

Throughout this chapter, we have seen how turbulence modeling impacts the study of turbulent compressible flows, specially with those that present interactions between shock-waves, boundary layers and vortex structures (common configurations for transonic and supersonic aircraft or rocket engines, for example). We also have studied how our hybrid model developed in chapter 2 fits and behaves in the context of turbulent modeling.

First, as a result of a detailed review of the state-of-the-art, we can conclude that turbulence modeling is required in order to solve the kind of applications we are interested in (transonic and supersonic aerodynamics and combustion in engines). The required computational power to solve such applications is unfeasible by means of DNS due to the extremely small control volumes required to solve boundary layers and small vortex, which in turn results in very small time-steps for the explicit integration of the NS equations. RANS and more recently LES studies exist on this field, primary using high-order hybrid-like schemes on structured meshes. Relatively low to nonexistent studies exist using low-order hybrid schemes on unstructured meshes, such as the one developed in this thesis.

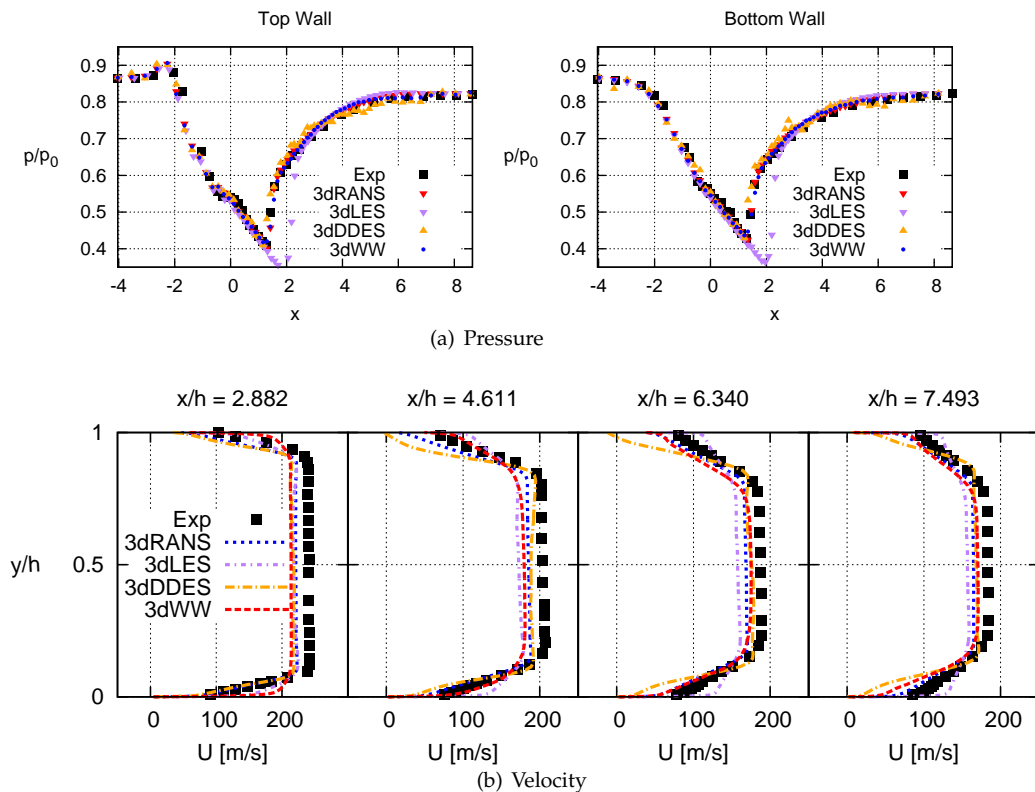


Figure 4.10: Three-dimensional Sabjen's diffuser weak case.

The turbulence models studied in this work are: the Spalart-Allmaras RANS model, the Smagorinsky, WALE and VMS LES models, the Werner & Wengel wall model and the DDES hybrid RANS/LES model. They represent only a small percentage of the existing turbulent models. A subsonic and supersonic channel flow was studied to asses the performance of the different LES models in the compressible framework. Among the three different proposed methods, WALE and VMS gave the better results, and similar among them. The WALE model was chosen to continue the research since it is cheaper in terms of computing time when compared to VMS and it gave almost the same level of accuracy.

The models were all tested and compared in a transonic diffuser. This problem was chosen because it presents all the features we are interested in: a subsonic flow undergoing supersonic, forming a shock wave that in turn interacts with boundary layers which results in flow separation and turbulence. Concerning the RANS results, although the pressure profiles showed the ability of the method to capture shock wave position, velocity profiles presented qualitative discrepancies. This difference has been reported by other authors and attributed to three-dimensional effects [30], which is indeed the weakness of the RANS modeling. We decided to use the SA model in its conservative form since it gave slightly better results than the original non-conservative formulation. The introduction of compressible corrections proposed in the literature did not seem to affect the result. Continuing with the three-dimensional studies, LES results showed that accuracy on boundary layers is required in order to predict accurately the flow features. Since they do not introduce turbulent modeling on boundary layers, DNS levels of accuracy is required. This fact has been observed by other researchers, and alternative have been proposed which consists of providing boundary layer modeling to the LES model, via a RANS model (DDES) or an analytical function (WW). DDES approach was able to provide the right information in order to allow the LES model to predict the shock position, but it also resulted in extremely large boundary layer thickness. This fact can be due to the interaction between the RANS and LES models. On the other hand, the WW model was able to provide the right information in order to predict the shock position accurately on the LES model, as well as to reproduce velocity profiles, specially in the near wall regions. The most important ideas resulting of this study are presented in table 4.3. Overall, results show that the hybrid methodology is suitable for SBLI numerical studies. It is a good option for LES and DNS of discontinuous compressible flows where classical artificial diffusion schemes are too dissipative [1].

Finally, the study on wall modeling for LES is encouraged in sight of our results. They allow the use of LES for internal and external flows with thick boundary layers avoiding the requirements of DDES or other RANS-based or hybrid RANS/LES models, which need primary a small y^+ .

Model	3D unsteady	y^+	Flow type	SBLIs
RANS	NO	1-5	attached	YES
LES	YES	< 1	medium to low Re	NO
DDES	YES	1-5	external	NO
WMLES	YES	10-100	high Re and Ma	YES

Table 4.3: Summary of turbulent models aspects.

References

- [1] S. Pirozzoli. Numerical Methods for High-Speed Flows. *Annu. Rev. Fluid Mech.*, 43:163–94, 2011.
- [2] S. Lee, S K. Lele, and P. Moin. Interaction of isotropic turbulence with shock waves: effect of shock strength. *J. Fluid Mech.*, 340:225–47, 1997.
- [3] F. Ducros, V. Ferrand, F. Nicoud, C. Weber, D. Darracq, C. Gachereau, and T. Poinsot. Large-eddy Simulation of Shock-turbulence Interaction. *J. Comput. Phys.*, 152(2):517–49, 1999.
- [4] J. Larsson and S K. Lele. Direct numerical simulation of canonical shock/turbulence interaction. *Phys. Fluids*, 21:126101, 2009.
- [5] J. Délery and J G. Marvin. Shock-wave boundary layer interactions. *AGARDograph 280*, AGARD, 1986.
- [6] N A. Adams. Direct simulation of the turbulent boundary layer along a compression ramp at $M = 3$ and $Re = 1685$. *J. Fluid Mech.*, 420:47–83, 2000.
- [7] N A. Adams amd K. Shariff. A high-resolution hybrid compact-eno scheme for shock-turbulence interaction problems. *J. Comput. Phys.*, 127:27–51, 1996.
- [8] M. Wu and M. Martín. Direct numerical simulation of supersonic turbulent boundary layer over a compression ramp. *AIAA J.*, 45:879–89, 2007.
- [9] E M.Taylor, M. Wu, and m P. Martín. Optimization of nonlinear error for weighted essentially non-oscillatory methods in direct numerical simulations of compressible turbulence. *J. Comput. Phys.*, 223:384–97, 2007.
- [10] D P. Rizzetta, M R. Visbal, and D V. Gaitonde. Large-eddy simulation of supersonic compression-ramp flow by high-order method. *AIAA J.*, 39:2283–92, 2001.

- [11] M R. Visbal and D V. Gaitonde. Shock capturing using compact-differencing-based methods. *Presented at AIAA Aerosp. Sci. Meet. Exhib.*, 43rd, Reno, AIAA Pap. 2005-1265, 2005.
- [12] R. von Kaenel, L. Kleiser, N A. Adams, and J B. Vos. Large-eddy simulation of shock-turbulence interaction. *AIAA J.*, 42:2516–28, 2004.
- [13] N A. Adams and S. Stolz. A subgrid-scale deconvolution approach for shock-capturing. *J. Comput. Phys.*, 178:391–428, 2002.
- [14] E. Garnier, P. Sagaut, and M. Deville. Large-eddy simulation of shock/boundary-layer interaction. *AIAA J.*, 40:1935–44, 2002.
- [15] S. Pirozzoli and F. Grasso. Direct numerical simulation of impinging shock wave/turbulent boundary layer interaction at $M = 2.25$. *Phys. Fluids*, 18(6):065113, 2006.
- [16] E. Touber and N D. Sandham. Large-eddy simulation of low-frequency unsteadiness in a turbulent shockinduced separation bubble. *Theor. Comput. Fluid Dyn.*, 23:79–107, 2009.
- [17] P. Dupont, S. Piponnaiu, A. Sidorenko, and J F. Debieve. Investigation by particle image velocimetry measurements of oblique shock reflection with separation. *AIAA J.*, 46:1365–70, 2008.
- [18] N D. Sandham, Y F. Yao, and A A. Lawal. Large-eddy simulation of transonic turbulent flow over a bump. *Int. J. Numer. Method H.*, 24:584–95, 2003.
- [19] S. Pirozzoli, M. Bernardini, and F. Grasso. Direct numerical simulation of transonic shock/boundary layer interaction under conditions of incipient separation. *J. Fluid Mech.*, 657:361–93, 2010.
- [20] S. Kawai and S K. Lele. Large-eddy simulation of jet mixing in supersonic cross-flows. *AIAA J.*, 48:2063–83, 2010.
- [21] S. Kawai and S K. Lele. Wall-modeling in large eddy simulation: Length scales, grid resolution, and accuracy. *J. Comput. Phys.*, 227:9498–526, 2007.
- [22] D J. Hill, C. Pantano, and D I. Pullin. Large-eddy simulation and multiscale modelling of a richtmyer-meshkov instability with reshock. *J. Fluid Mech.*, 557:29–61, 2006.
- [23] D J. Hill and D I. Pullin. Hybrid tuned center-difference-weno method for large-eddy simulations in the presence of strong shocks. *J. Comput. Phys.*, 194:435–50, 2004.

- [24] J A. Ekaterinaris. High-order accurate, low numerical diffusion methods for aerodynamics. *Progr. Aerosp. Sci.*, 41:192–300, 2005.
- [25] H. Babinsky and J K. Harvey. *Shock Wave-Boundary-Layer Interactions*. Cambridge University Press, 2014.
- [26] D S. Dolling. Fifty Years of Shock-Wave/Boundary-Layer Interaction. *AIAA J.*, 39(8):1517–31, 2001.
- [27] J T. Salmon, T J. Bogar, and M. Sajben. Laser Doppler Velocimeter Measurements in Unsteady, Separated, Transonic Diffuser Flows. *AIAA J.*, 21(12):1690–7, 1983.
- [28] T J. Bogar, M. Sajben, and J C. Kroutil. Characteristic Frequencies of Transonic Diffuser Flow Oscillations. *AIAA J.*, 21(9):1232–9, 1998.
- [29] T. Hsieh, J. Wardlaw, and P. Collins. Numerical investigation of Unsteady Inlet Flowfields. *AIAA J.*, 25(1):75–81, 1987.
- [30] <http://www.grc.nasa.gov/WWW/wind/valid/transdif/transdif.html>.
- [31] D C. Wilcox. *Turbulence modeling for CFD*. DCW Industries, Inc., 1998.
- [32] S. Catris and B. Aupoix. Density corrections for turbulence models. *Aerosp. Sci. Technol.*, 4:1–11, 2000.
- [33] E. Garnier, N. Adams, and P. Sagaut. *Large Eddy Simulation for Compressible Flows*. Springer, 1993.
- [34] O. Lehmkuhl, C D. Pérez-Segarra, R. Borrell, M. Soria, and A. Oliva. TER-MOFLUIDS: A new Parallel unstructured CFD code for the simulation of turbulent industrial problems on low cost PC Cluster. *Proc. Parallel CFD Conf.*, pages 1–8, 2007.
- [35] I. Rodríguez, O. Lehmkuhl, R. Borrell, and A. Oliva. Direct Numerical Simulation of a NACA0012 in Full Stall. *Int. J. Heat Fluid Fl.*, 43:194–203, 2013.
- [36] O. Lehmkuhl, I. Rodríguez, A. Bæz, A. Oliva, and C D. Pérez-Segarra. On the Large-Eddy Simulations for the flow around aerodynamic profiles using unstructured grids. *Comput. Fluids*, 84:176–89, 2013.
- [37] O. Lehmkuhl, I. Rodríguez, R. Borrell, J. Chiva, and A. Oliva. Unsteady Forces on a Circular Cylinder at Critical Reynolds Numbers. *Phys. Fluids*, 26:12, 2013.
- [38] P. Spalart and S. Allmaras. A one-equation turbulence model for aerodynamic flows. *AIAA J.*, 92, 1992.

- [39] S. Catris. Etude de contraintes et qualification de modeles a viscosite turbulente. PhD thesis, SupAero., 1999.
- [40] M. Pino, U. Piomelli, and G V. Candler. Subgrid-Scale Models for Compressible Large-Eddy Simulations. *Theor. Comp. Fluid Dyn.*, 13:361–7, 2000.
- [41] G. Erlebacher, M Y. Hussaini, C G. Speziale, and T A. Zang. Towards the large-eddy simulation of compressible turbulent flows. *J. Fluid Mech.*, 238:155–85, 1992.
- [42] F. Nicoud and F. Ducros. Subgrid-scale stress modeling based on the square of the velocity gradient tensor. *Flow Turbul. Combust.*, 62:183–200, 1999.
- [43] M. Shur, P. R. Strelets, M. Spalart, and A. Travin. Detached-eddy simulation of an airfoil at high angle of attack. *Engineering Turbulence Modelling and Measurements*, 4:669–678, 1999.
- [44] P. R. Spalart, S. Deck, M. L. Shur, and K. D. Squires. A new version of detached-eddy simulation, resistant to ambiguous grid densities. *Theor. Comput. Fluid Dyn.*, 20:181–195, 2006.
- [45] J. Kim, P. Moin, and R. Moser. Turbulence statistics in fully developed channel flow at low reynolds number. *J. Fluid Mech.*, 177:133–66, 1987.
- [46] H. Foysi, S. Sarkar, and R. Friederich. Compressibility effects and turbulence scalings in supersonic channel flow. *J. Fluid Mech.*, 509:207–16, 2004.
- [47] H. Eckelmann. Mitteilungen aus dem mpi für stromungsforschung und der ava. Gottingen, 1970.
- [48] G N. Coleman, J. Kim, and R. Moser. A numerical study of turbulent supersonic isothermal-wall channel flow. *J. Fluid Mech.*, 305:159–83, 2004.

Multi-component turbulent compressible flows.

5.1 Introduction

In previous chapters we have restricted our work to the numerical resolution of the NS equations for perfect gases with constant heat capacities, or ideal gases, such as air. This formulation allows to solve an enormous number of cases of interest and applications in the aerodynamics and industrial field where only one (ideal) gas is present. We used the single component equations to solve, among other, the turbulent flow around an airfoil in section 2.5, and the transonic turbulent flow with SB-LIs in a diffuser in section 4.4.2. Although this model is useful in many applications, other problems require more sophisticated mathematical models. This is the case, for example, of the flow in a H_2 - O_2 liquid-rocket engine where the two gases are injected together in a combustion chamber, reacting to form H_2O and other species, releasing heat and then evolving in a converging-diverging nozzle (where shock waves may appear and interact with boundary layers and turbulent structures). Another example would be the flow in a turbine, where the air (which is indeed a mixture of gases) is mixed with some fuel, then reacts, forming a lot of different products, and they are expelled through the nozzle. We can see the difficulty since the flow and the chemical species have to be simultaneous solved, and the number of chemical species can be very large for many applications.

Concerning numerical models, multi-component flows cannot only see discontinuities due to shock waves but also due to components interface. This is the case,

for example, of a jet where some gas is being released into the environment. This gas can have low velocities, even so slow that the flow is incompressible. Nevertheless, in the interface of the gas that is being ejected, the surrounding air can have very different thermodynamic properties, in density for example, that can be seen as a discontinuity similar to a shock wave. This fact has the same implications on the numerical schemes that those presented in chapter 2. This is the reason why we will update our hybrid numerical scheme in order to identify not only shocks but also gas interfaces, where a dissipative scheme will be used instead of the kinetic energy preserving scheme in order to avoid numerical oscillations and simulations blow-up.

This chapter begins with a review of work by other authors in the field of compressible numerical combustion. Then, the multi-component NS equations are derived. They represent a more general formulation than the one proposed in section 1.3.2. Afterwards, our hybrid numerical scheme will be modified in order to be able to solve flows with mixtures of gases. Finally, a non-reactive propane jet is solved in order to show the ability of the new scheme to solve this kind of problems.

5.2 State of the art

The number of applications in which combustion plays a key role are huge, such as the rocket industry, aircraft engine or military. More than 85% of the energy obtained today comes from burning something. Despite the growth of renewable energy is increasing, its growth is slower than the required amount of energy consumed. This means that combustion will play a role also in the future, since it will continue to be an important source of energy. Furthermore, energy overproduction by renewable systems is often stored in some form of chemical process in order to later recover that energy with a combustion process.

Nevertheless, combustion comes with some known drawbacks such as pollution emission and noise. Also, probably the most challenging problem that humanity face at the present moment is climate change and global warming, which is caused mainly by combustion. These facts lead the field of numerical combustion to pursue efficiency by reducing emissions while producing the same amount of power. This requires optimizing devices where combustion is used to generate power, such as gas turbines. This process of optimization can be very expensive. Therefore, it is preferable to compute something before building it. This requires trust in the code and a lot of experiments. Here, we face the first issue: the computational code.

Numerical combustion is a multi-physics phenomenon since chemistry, radiation, flow and acoustics is mixed. These entangled phenomena have different scales associated (from nanometers to kilometers) heavily impacting the required computational power and constraining the numerical methods. The strategy to tackle nu-

merical combustion of turbulent compressible flows has not converged to an optimal solution, so the numerical methods found in the literature are numerous. Direct Numerical Simulations (DNS) are restricted to very few relatively simple and small scale cases with less to none practical application. Traditional solvers used Reynolds-Averaged Navier-Stokes models (RANS) to compute combustion, but due to the important unsteady effects (maximum temperatures are always a design constrain, not the mean temperature) the approach that is most used today is Large Eddy Simulation (LES). Moreover, RANS solvers cannot predict combustion instabilities, cycle-to-cycle variations, self-ignition and emissions formation. LES is based on the idea of computing the large scales of the motion and model the small ones. For non-reactive flows, we already explored this approach in section 4.3.2. For reacting flows, nevertheless, closure terms have to be provided also for the reaction rate terms. To overcome this issues, the most used approaches are:

- Flamelet Progress Variable models (FPV) [1–3]. The reaction rates are assumed to take place in thin layers, separating the reactant mixture from the product mixture, wrinkled by turbulence.
- Probability Density Function models (PDF) [4]. The filtered reaction rates are presumed through probability density functions.
- Finite Rate Chemistry models (FRC) [5–7]. They use different mathematical and phenomenological models of the filtered reaction rates. Some examples are the Thickened Flame Model (TFM), PaSR model or the Eddy Dissipation Concept (EDC).
- Conditional Moment Closure (CMC) [8]. The species equations are conditionally averaged on a few variables on which the reaction rates are critically known to depend.
- Linear Eddy Models (LEM) [9]. They use a grid-within-the-grid approach to solve one-dimensional species equations with full resolution.

All these methods have certain features that limit their usefulness for engineer applications. Therefore, the development of more versatile and cost-effective LES combustion models is encouraged. Some recent works, like [10], propose the idea of using the mathematical treatment of multiphase flows for the description of fine-scale structures dissolved in a background turbulence, characterized by lower intensity mixing. Transport equations for the closure terms are proposed and the method is tested against other LES models in the Volvo validation rig [11], where experimental data is available showing its better performance when compare to the aforementioned models.

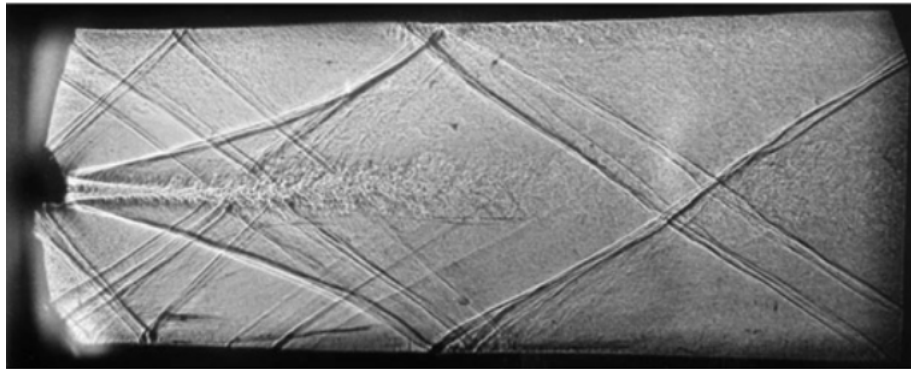


Figure 5.1: Non-reactive scramjet extracted from [6].

A particular interesting application which fits into the frame of this thesis is the study of supersonic ramjet combustors [6,12]. Numerous numerical and experimental tests study this case because it involves the interaction of the typical combustion phenomenon (chemistry, radiation, flow and acoustics) with shock-waves. Figure 5.1 shows a Schlieren image for a class of scramjet combustor where no chemical reactions take place. Air enters the combustor at supersonic speed, forming shock-waves in the interior augmenting the pressure of the flow. Then, hydrogen is introduced with injectors and mixes with the air. If the mix is ignited we can observe something like figure 5.2. As we can see, the flow features are completely different. A good numerical scheme must account not only for shock-waves but also for the flame fronts that take place in the combustion process. The optimization of the injectors position, the combustor geometry and the conditions at which the hydrogen is introduced, among others, are the perfect example of application of the numerical methodology presented in this thesis.

5.3 Multi-component Navier Stokes equations

In this section the conservation equations for reacting flows are presented. The differences between this form and the already discussed one for non-reactive flows are also highlighted.

Conservation of mass and species

The total mass conservation equation is unchanged compared to non-reacting flows since combustion does not generate mass.

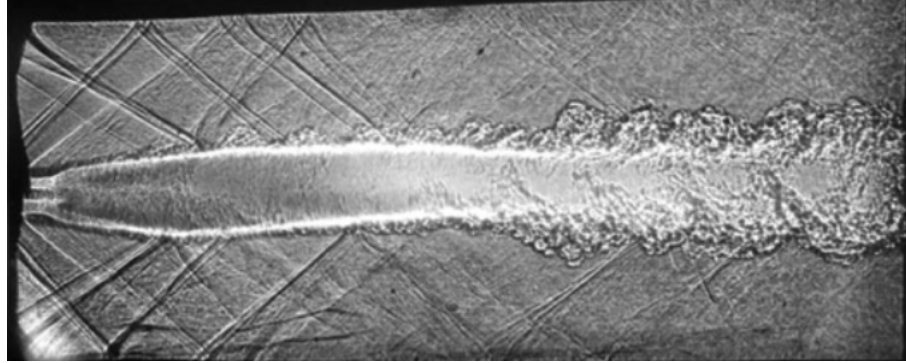


Figure 5.2: Reactive scramjet extracted from [6].

$$\rho_t + \nabla \cdot (\rho \mathbf{u}) = 0 \quad (5.1)$$

Nevertheless, multi-component flows involve multiple species and the NS equations are required to account for the transport of each one of them. Species are characterized through their mass fraction Y_k for $k = 1$ to N , where N is the number of species in the mixture.

$$Y_k = \frac{m_k}{m} \quad (5.2)$$

Here, m_k is the mass of species k , while m is the total mass, $m = \sum m_k$.

Going to multi-component flows requires solving $N + 5$ variables instead of 5. Most chemical reactions involve a large number of species, which results in a significant effort needed to compute reacting flows. The mass conservation equation for species k is

$$(\rho Y_k)_t + \nabla \cdot (\rho(\mathbf{u} + \mathbf{V}_k)Y_k) = \dot{\omega}_k \quad (5.3)$$

where \mathbf{V}_k is the diffusion velocity of the species k in the mixture and $\dot{\omega}_k$ is the reaction rate of species k . By definition:

$$\sum_{k=1}^N Y_k \mathbf{V}_k = 0 \quad \text{and} \quad \sum_{k=1}^N \dot{\omega}_k = 0 \quad (5.4)$$

The diffusion velocities can be obtained using the Fick's law

$$\mathbf{V}_k Y_k = -D_k \nabla Y_k \quad (5.5)$$

where D_k is the diffusion coefficient of species k in the mixture. Then, equation 5.3 become

$$(\rho Y_k)_t + \nabla \cdot (\rho \mathbf{u} Y_k) = \nabla \cdot (\rho D_k \nabla Y_k) + \dot{\omega}_k \quad (5.6)$$

Conservation of momentum

The equation of momentum has the same form in reacting flows and non-reacting flows:

$$(\rho \mathbf{u})_t + \nabla \cdot (\rho \mathbf{u} \mathbf{u}) = \nabla \cdot \boldsymbol{\tau} - \nabla p \quad (5.7)$$

The flow is modified by combustion because the viscosity μ strongly changes because of temperature and species concentration. Density also changes, resulting in local Reynolds number strong variations.

Conservation of energy

Multiple forms of the energy equation exist. The total energy is chosen as conserved magnitude in the conservation equation in order to be consistent with the formulation presented in chapter 1 where the work carried out by body forces is neglected.

$$E_t + \nabla \cdot ((E + p)\mathbf{u}) = \nabla \cdot (\boldsymbol{\tau} \cdot \mathbf{u}) - \nabla \cdot \mathbf{q} - \nabla \cdot (\rho \sum_{k=1}^N h_{s,k} Y_k \mathbf{V}_k) + \dot{\omega}_T \quad (5.8)$$

where E is the total energy, \mathbf{q} is the heat flux, $\dot{\omega}_T = -\sum_{k=1}^N \Delta h_{f,k}^\circ \dot{\omega}_k$ is the heat release being $\Delta h_{f,k}^\circ$ the formation enthalpy of species k .

The definition of the total energy given in equation 1.16 was a simplification derived from the constant c_p assumption. Since this hypothesis no longer apply, new definitions have to be used. We begin defining the specific enthalpy for one species.

$$h_k = \int_{T_0}^T c_{p,k} dT + \Delta h_{f,k}^\circ \quad (5.9)$$

where T_0 is the reference temperature, which can be an arbitrary value. Due to the difficulty to gather experimental information at $T_0 = 0K$, formation enthalpy is usually tabulated at standard temperature $T_0 = 298.15K$. Nevertheless, we use $T_0 = 0K$ as our reference value due to numerical issues.

By definition $h_k = e_k + p_k/\rho_k$ where e_k is the specific total energy of the species k . Summing for all species, we can then conclude that

$$E = H - p \quad (5.10)$$

where $E = \rho e$ and $H = \rho h$ are the total energy and enthalpy respectively. On the other hand, we can split the total energy in internal energy and kinetic energy

$$E = \rho e_s + \frac{1}{2} \rho \mathbf{u} \cdot \mathbf{u} \quad (5.11)$$

Internal energy and total energy are related with the expression

$$e_s = e - \sum_{k=1}^N \Delta h_{f,k}^\circ Y_k \quad (5.12)$$

As we already know, the total energy, momentum and density are the conserved variables of our system of equations. Hence, they are the magnitudes that we will find after each resolution step. From these, we can easily obtain the velocity $\mathbf{u} = \rho \mathbf{u} / \rho$. In the system of equations presented in chapter 1 we could compute the pressure from the total energy equation 1.16 and then find the temperature with the equation of state, or viceversa. This is not the case now, since pressure and temperature are coupled. Some iterative procedure must be used in order to solve the thermodynamic magnitudes of the problem.

The equation of state

For a mixture of N perfect gases, the total pressure is the sum of partial pressures:

$$p = \sum_{k=1}^N p_k \quad (5.13)$$

where $p_k = \rho_k \frac{R}{W_k} T$, W_k is the molecular weight of species k and $R = 8.314 \text{ J/molK}$. Since the density of a multi-component mixture is

$$\rho = \sum_{k=1}^N \rho_k \quad (5.14)$$

we can define the equation of state as

$$p = \rho \frac{R}{W} T \quad (5.15)$$

where W is the mean molecular weight of the mixture

$$\frac{1}{W} = \sum_{k=1}^N \frac{Y_k}{W_k} \quad (5.16)$$

Summary

All the problems presented in the previous chapters can also be solved with the multi-component formulation, since air is in fact a mixture of gases composed by approximately 79% of N_2 , 21% of O_2 and small fractions of H_2O , CO_2 and other gases (usually in chemical equilibrium, hence with no chemical reactions).

The continuity equation has not been changed compared to the original NS equations. Nevertheless, N new conservation equations must be solved for the N species of the problem. In order to solve these new equations, the diffusion of each species in the mixture (given by the Fick's law) and the reaction rate of each species have to be computed. Concerning the momentum equation, no changes are required. On the other hand, the energy equation introduces some changes. The first one is in its own definition, since c_p is no longer constant. Then, the heat released by any chemical reaction has to be included as well as the enthalpy flux. Finally, the equation of state has the same form except for the gas constant, that now takes into account the molecular weight of the mixture.

Some issues remain open, such as the computation of the diffusion coefficient of the species k in the species equation as well as its reaction rate. These magnitudes can be computed in different ways. The work presented in this chapter is built on top of previous work by fellow researchers [13], where more information on the implementation of these magnitudes can be found. Hence, a simple definition of the diffusion coefficient based on the Lewis number is used. On the other hand, Arrhenius law is employed for the evaluation of the reaction rates.

5.4 Upgrading the hybrid flux

As we did in the development of our hybrid scheme, we first distinguish between inviscid and viscous fluxes.

$$F(\phi_f) = F^{inv}(\phi_f) + F^{visc}(\phi_f) \quad (5.17)$$

Inviscid fluxes are computed using a Kinetic Energy Preserving scheme as a basis. When the discontinuity sensor recognizes a discontinuity within the flow, artificial diffusion is added in a very selective way by means of an upwind method. This approach minimizes the amount of numerical viscosity while having a stable scheme provided a fine tune of the discontinuity sensor, Φ .

$$F^{inv}(\phi_f) = (1 - \Phi)F^{KEP}(\phi_f) + \Phi F^{UDS}(\phi_f) \quad (5.18)$$

Viscous fluxes are treated in the same way as described in section 2.3.4.

In the KEP approach, the value of ϕ_f is computed following the skew-symmetric form of the convective term.

$$\phi_f = \frac{1}{2}(\phi_P + \phi_O) \quad (5.19)$$

Remember that using the divergent form leads to unstable solutions.

The artificial diffusion required to make the numerical scheme stable in presence of flow discontinuities is introduced by means of upwind-like schemes. These methods are based on the Godunov's method, which solves the Riemann problem at each cell interface. Following the same procedure that in section 2.3.2, one can derive the expression for the flux function as

$$F(\phi_f) = A\phi_O + \sum_{p=1}^m (\lambda^p)^- \alpha^p r^p \quad (5.20)$$

or

$$F(\phi_f) = A\phi_P - \sum_{p=1}^m (\lambda^p)^+ \alpha^p r^p \quad (5.21)$$

where λ and α are respectively the characteristic velocities and wave coefficients of the Riemann problem associated at the face f . In section 2.3.2, we found these quantities for the original 5 equation system, which are the same for mixtures of perfect gases. Nevertheless, since now we deal with $N + 5$ equations, extra values for λ and α are required to solve the conservation equations of species. Luckily, this is the easiest characteristic problem to solve. Consider the convective part of equation

$$(\rho Y_k)_t + \nabla \cdot (\rho \mathbf{u} Y_k) = 0 \quad (5.22)$$

The Jacobian matrix for each component is $A = \frac{\partial f}{\partial \phi} = \frac{\partial(\rho \mathbf{u} Y_k)}{\partial(\rho Y_k)} = \mathbf{u}$. Now, if we compute the eigenvalues and eigenvectors of this matrix we obtain that $R = 1$ and $\lambda = u_n$. Following with the hyperbolic analysis, an approximate Riemann solver would give as a results that

$$\alpha = \delta_{\rho Y_k} = (\rho Y_k)_P - (\rho Y_k)_O \quad (5.23)$$

Notice that the N extra equations are independent from each other, making the hyperbolic analysis quite simple.

Upgrading the discontinuity sensor

In section 2.3.3, we developed a shock capturing sensor that was able to identify the presence of shock waves in the flow while discriminating turbulent structures. In this sense, we could introduce the numerical diffusion in a very selective way, only where it is required. Nevertheless, for multi-component flows, discontinuities may also appear even in the subsonic incompressible regimen if the thermodynamic properties of different components in the mixture are different. Remember that the Larsson sensor has the form

$$\Phi = \begin{cases} 0 & \text{if } \Theta \leq 1 \\ 1 & \text{if } \Theta > 1 \end{cases} \quad (5.24)$$

where

$$\Theta = \frac{-\nabla \cdot \mathbf{u}}{\max(L_{ss1}|\nabla \times \mathbf{u}|, L_{ss2}(\frac{a}{ds}))} \quad (5.25)$$

Here, a is the speed of sound, $ds = V_c^{1/3}$ and L_{ss1} and L_{ss2} are problem dependent constants. If we take a close look at the form of the sensor, we can interpret it as the ratio between the velocity gradient and the maximum speed at which information is transmitted through the flow. Based on this same idea, we can identify a scalar front comparing the gradient of a species with the maximum possible gradient, resulting in

$$\Theta = \frac{-\nabla \cdot \mathbf{u}}{\max(L_{ss1}|\nabla \times \mathbf{u}|, L_{ss2}(\frac{a}{ds}))} + \frac{\nabla Y_k}{L_{ss3}(\frac{1}{ds})} \quad (5.26)$$

since by definition Y_k can only take values between 0 and 1. The constant L_{ss3} allows us to tune the sensor to be more selective or less.

5.5 Numerical tests

5.5.1 Non-reactive propane Jet

A non-reacting propane jet [14–17] is used to analyse the behaviour of the upgraded hybrid scheme. The case featured in the TNF Workshop. It consists of a propane (C_3H_8) jet issuing through a central $D = 5.2mm$ pipe at $V_b = 53m/s$. The pipe thickness is $t_f = 3.8mm$. The coflow is regular air, flowing at $9.2m/s$. Both propane and air are at $292K$ and $107500Pa$. The central jet Reynolds number is 68000.

Numerical simulations have been carried out on a $9D \times 65D \times 2\pi$ domain in the radial 'r', axial 'y' and azimuthal direction, respectively. A structured mesh was

created, which consisted of $125 \times 300 \times 64$ control volumes. The mesh was concentrated near the pipe wall, $(D/2) < r < (D/2 + t_f)$, to better resolve the shear layer. For the numerical simulations, inflow velocity is set through a mean turbulent profile without fluctuations

$$V = V_c(1 - r/D)^{1/9} \quad (5.27)$$

where V_c is the centerline velocity, whose value is set by evaluating the integral of equation (5.27) and setting it equal to V_b . The exponent value has been set to better match the experimental inflow velocity profile.

Results

To study the behavior of our hybrid scheme in the context of multi-component flow, the different schemes that form it are considered for the analysis:

- The base kinetic energy-preserving scheme, denoted as 'KEP'.
- The 1st order upwind scheme, denoted as 'UDS'.
- A flux limiter scheme, specifically a Minmod, denoted as 'FL'.
- The hybrid scheme using the modified detector, equation 5.26, denoted as 'HYB' with $L_{ss3} = 0.1$.

For the four convective schemes considered, instantaneous mixture fractions snapshots are shown in figure 5.3. Comparing the results, it can be seen that the mixture fraction field computed with KEP evidences a jet break up close to the fuel inlet. Oppositely, UDS does not break up and the core potential jet extends indefinitely downstream. Hence, no transition to a turbulent jet occurs. When the current HYB is applied, the jet break up is found around $6D$ downstream the fuel inlet. Similarly, with FL the core jet is seen to extend around $6D$ and the transition to a turbulent jet taking place thereafter.

Figure 5.3 shows that FL gives more smoothed transitions between core jet and coflow compared to the current HYB scheme. Furthermore, the mean time average mixture fraction field is compared against experimental data [14, 15] in figure 5.4. Results are presented at three axial distances, specifically at $y/D = 4, 15, 30$. It can clearly be seen that results obtained with UDS show that the core jet extends too far downstream. With the KEP scheme the transition to a turbulent jet occurs too early. Both FL and HYB schemes show improved results, being the latter closer to the experimental results.

Mean and rms of the velocity for the different schemes analyzed are shown in figure 5.5. Focusing on the results obtained with KEP, it can be seen that mean velocities around the jet are higher than the experimental results. Additionally, velocity

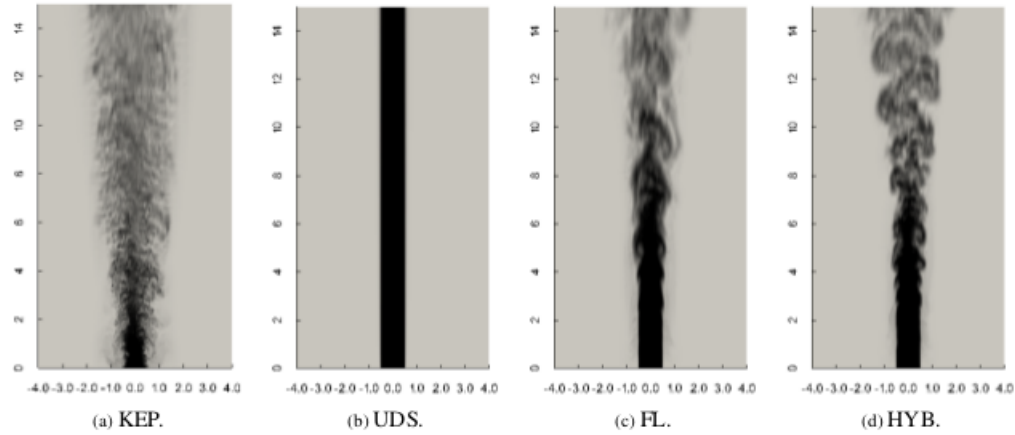


Figure 5.3: Mixture fraction instantaneous snapshots. Radial-axial cutplane. Axis have been scaled by the jet diameter D . Black to white coloring denotes mixture fraction values ranging from 1 to 0.

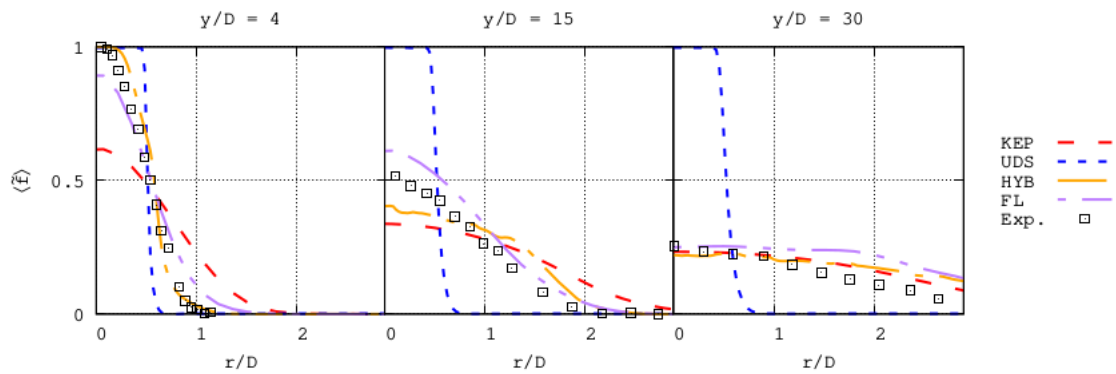


Figure 5.4: Mean mixture fraction. Experimental results from [14,15]

fluctuations are too high compared to the experimental ones. The reason for this behavior is the jet breaking-up too early. On the other hand, with UDS the jet is seen to extend too far downstream. The potential core of the jet remains unperturbed at all axial locations. This behavior is caused by the diffusive properties of the upwind scheme. Results obtained using the hybrid scheme with the proposed sensor show good agreement with the experimental data, showing the suitability of the approach.

Furthermore, to illustrate the ability of the detector to act locally the regions where the detector is active at one instant of the simulation are depicted in figure 5.6. In the snapshots, the control volumes where the sensor value is larger than the threshold are shown superimposed to the mixture fraction and velocity fields, respectively. As it can be seen, the low-order scheme is only applied to certain control volumes, corresponding to regions with sharp changes in composition.

In terms of computational effort, the upwind scheme presents the higher cost because of the amount of operations required by the approximate Riemann solver. Nevertheless, the unstable nature of the kinetic-energy preserving scheme requires smaller time steps. On the other hand, the hybrid scheme presents similar requirements than the KEP since the upwind scheme is only applied in a few control volumes. In terms of computational time, the hybrid scheme results in the most expensive one compared with its components solely (UDS and KEP), because the coupling between the two methods requires slightly better temporal accuracy. However, the increased accuracy accounts for this drawback.

Conclusions

Results show how the amount of numerical diffusion introduced into the simulation is limited with the hybrid approach. Furthermore, it is shown that using only a kinetic energy-preserving scheme is not appropriate for multi-component flows with sharp species gradients. Instabilities arising within the flow produce the early break up of the jet and result in wrong flow predictions. Nevertheless, with the application of a dissipative scheme in the control volumes that present large species gradients, where unphysical oscillations can appear, the simulation becomes stabilized and thus, obtaining more accurate results in terms of mean values and second-order statistics.

5.6 Conclusions

In this chapter we have presented the NS equation for multi-component reacting flows. We saw that the mass conservation equations remains unchanged as well as the momentum equation. On the other hand, two extra terms appear in the energy

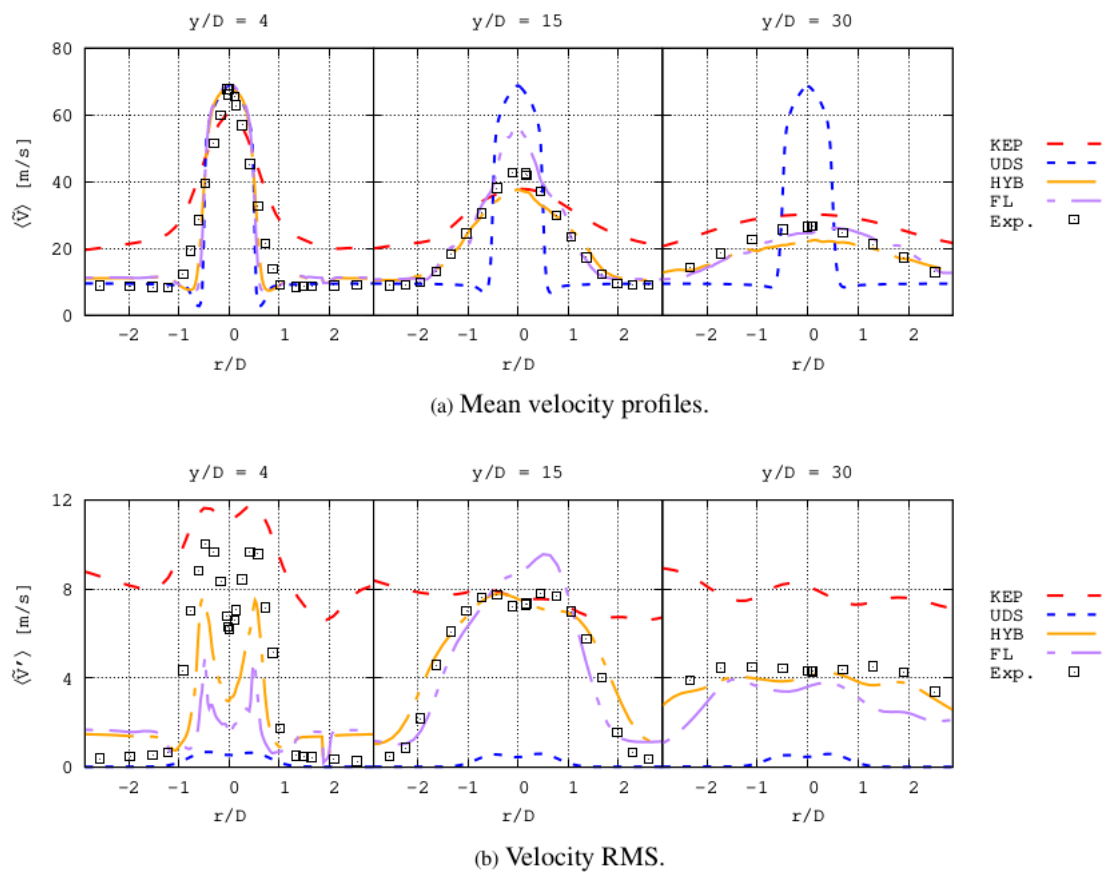


Figure 5.5: Radial velocity profiles. Experimental results from [14,15]

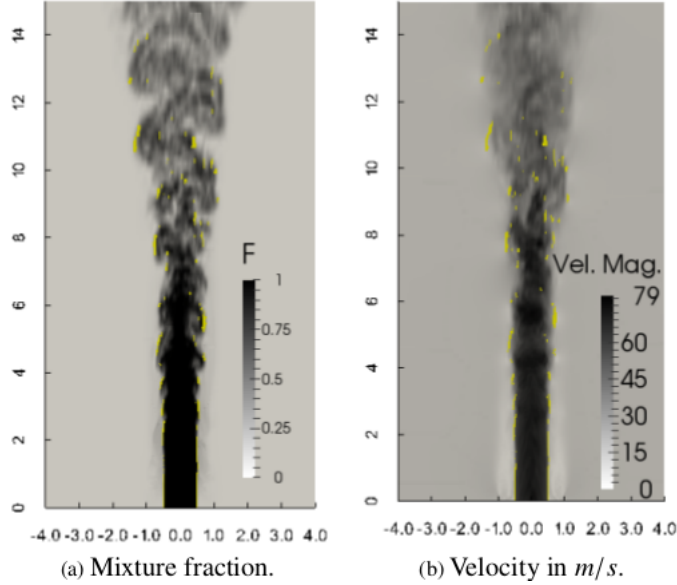


Figure 5.6: Instantaneous snapshots with the front detector highlighted. Radial-axial cutplane. Axis have been scaled by the jet diameter D .

equation accounting for the heat released in combustion processes and energy consumption in species formation. Also, N new conservation laws are required to solve the transport of the considered N species that form the mixture, giving as a result a system of $N + 5$ equations to be solved.

Once the new formulation was presented, our hybrid scheme was upgraded in order to work properly in the multi-component context. Concerning the KEP part of the scheme, no changes had to be made. For the computation of the upwind scheme used to add numerical diffusion, no changes are required as long as we work with a mixture of perfect gases. Finally, N new Riemann problems have to be solved for the N species transport equations. Nevertheless, the hyperbolic analysis was very simple. The upgrade of the discontinuity sensor consisted of the addition of an extra term accounting for scalar fronts. This can cause flow discontinuities that have nothing to do with shock waves but have to be addressed in order to avoid simulation divergence. The detector uses the gradient of the scalar of interest and compares it to a theoretical maximum scalar gradient.

The upgraded hybrid scheme for scalar fronts has been tested in order to detect regions with sharp scalar gradients in a propane jet issuing into an air coflow. It has

been evidenced that the application of shock capturing techniques to identify multi-component flow fronts is a suitable technique that give accurate results. An advantage of the present method is that no high-order reconstructions are required. This fact makes the hybrid method specially attractive for unstructured grids. Having control of the total numerical diffusion introduced is important in LES where subgrid methods are relied upon to introduce the required turbulent dissipation. This cannot be achieved with upwind-like dissipative schemes, even in high-order forms, since some level of numerical diffusion is always introduced throughout the domain. Furthermore, computational costs are reduced compared to high-order approaches such as flux limiters.

References

- [1] P. Wang and X. S. Bai. Large eddy simulation of turbulent premixed flames using level-set g-equation. *Proc. Combust. Inst.*, 30:583, 2005.
- [2] E. R. Hawkes and R. S. Cant. A flame surface density approach to large eddy simulation of premixed turbulent combustion. *Proc. Combust. Inst.*, 28:51, 2000.
- [3] R. Knikker and D. Veynante. Experimental study of the filtered progress variable approach for LES of premixed combustion. *Advances in LES of complex flows*. Eds. R. Friedrich and W. Rodi., 353.
- [4] P. Givi. Filtered density function for subgrid scale modeling of turbulent combustion. *AIAA J.*, 44:16, 2006.
- [5] F. Charlette, C. Meneveau, and D. Veynante. A power-law flame wrinkling model for les of premixed turbulent combustion. part I: Non-dynamic formulation and initial tests. *Combust. Flame*, 131:159, 2002.
- [6] M. Berglund, E. Fedina, J. Tegnér, C. Fureby, and V. Sabelnikov. Finite rate chemistry les of self-ignition in a supersonic combustion ramjet. *AIAA J.*, 48:540, 2010.
- [7] B. F. Magnussen. On the structure of turbulence and a generalised eddy dissipation concept for chemical reactions in turbulent flow. *19th AIAA Sc. Meeting. St. Louis, USA.*, 1981.
- [8] R. W Bilger. Conditional moment closure for turbulent reacting flow. *Phys. Fluids A*, 5:436, 1993.
- [9] V. Sankaran and S. Menon. Subgrid combustion modeling of 3d premixed flames in the thin-reaction-zone regime. *Proc. Combust. Inst.*, 38:575, 2005.

- [10] V. Sabelnikov and C. Fureby. Extended LES-PaSR model for simulation of turbulent combustion. *Progress in Propulsion Physics*, 4:539–68, 2013.
- [11] S. Olovsson Sjunnesson, A. and B. Sjöblom. Validation rig - A tool for flame studies. *VOLVO Aero AB*, 1991.
- [12] T. Sunami, P. Magre, A. Bresson, F. Grisch, M. Orain, and M. Kodera. Experimental study of strut injectors in a supersonic combustor using oh-plif. *AIAA/CIRA 13th International Space Planes and Hypersonics Systems and Technologies Conference*, 2005.
- [13] J. Ventosa. Numerical simulation of turbulent diffusion flames using flamelet models on unstructured meshes. Doctoral Thesis. Universitat Politècnica de Catalunya (UPC), 2015.
- [14] R. W. Schefer and R. W. Dibble. Rayleigh scattering measurements of mixture fraction in a turbulent nonreacting propane jet. In *24th Aerospace Sciences Meeting, Reno, NV, January 6-9*, 1986.
- [15] R. W. Schefer, V. Hartmann, and R. W. Dibble. Conditional sampling of velocity in a turbulent nonpremixed propane jet. *Sandia Report*, SAND87-8610, 1987.
- [16] F. C. Gouldin, R. W. Schefer, S. C. Johnston, and W. Kollmann. Nonreacting turbulent mixing flows. 12:257–303, 1986.
- [17] R. W. Dibble, W. Kollmann, and R. W. Schefer. Conserved scalar fluxes measured in a turbulent nonpremixed flame by combined laser doppler velocimetry and laser raman scattering. 55:307–321, 1984.

Conclusions and Further Research

6.1 Conclusions

This thesis was introduced in Chapter 1. These are the main conclusions:

- This thesis finds its motivation in the fields of aerodynamics and engine technology.
- Compressible flows are described by the Navier-Stokes equations, which emerge from conservation laws.
- Hyperbolicity mathematical properties apply for the Euler equations and the convective part of Navier-Stokes equations.
- Hyperbolic properties are useful for deriving numerical schemes.
- The work on this thesis has been developed using Finite Volume methods for unstructured meshes.
- The main objective has been the development of numerical tools to simulate turbulent compressible single- or multi-component flows with or without shock-waves.
- Different results of this thesis have been used by other researchers of the CTTC in their studies of application such as aerodynamics, acoustics, wall models for compressible flows and combustion.

In Chapter 2 a new hybrid scheme for the simulation of turbulent compressible flows was introduced and tested. These are the main conclusions:

- State-of-the-art numerical methods are divided in two main categories: dissipative and non-dissipative.
- Dissipative methods include upwind-like schemes, ENO and WENO. They are used in two forms: as a selective way to introduce small amounts of dissipation in order to avoid oscillations, or in very high-order formulations to obtain low-viscosity methods.
- Non-dissipative, or energy-consistent schemes, do not introduce numerical dissipation. They use the skew-symmetric formulation of the Navier-Stokes convective terms in order to be stable in smooth flows. They are unstable in the presence of shocks.
- Hybrid approaches combine the previous methods to obtain stable, low-viscosity schemes, which are required for LES and DNS.
- We have presented a new hybrid scheme. It was tested in several cases in order to evaluate its ability to simulate smooth flows and discontinuous flows.
- Our method has been used to study the subsonic and transonic flow around a NACA0012 airfoil, showing good agreement with reference data for the subsonic cases and providing valuable and genuine results for the transonic case.

Boundary conditions for turbulent compressible flows were developed in Chapter 3. These are the main conclusions:

- Boundary conditions are required to solve real-world applications.
- The common approach is based on the NSCBC method, which assumes a one-dimensional inviscid approach to compute waves at boundaries in a finite difference framework.
- We have proposed an alternative formulation based on the same idea but taking into account the full three-dimensional wave-like structure at boundaries.
- The method is framed in the Finite Volume domain, meaning that ghost cells are used at boundaries and boundary conditions are introduced softly via fluxes through boundary faces.
- The new boundary conditions were tested in several cases, showing their good performance even for three-dimensional turbulent flows in very small domains.

In Chapter 4 turbulent models for compressible flows were studied and tested. These are the main conclusions:

- Compressible flows always involve high-speed, high-Reynolds flows in real applications.
- DNS of such flows are limited to academical tests in simple configurations.
- RANS and LES are the typical approaches to overcome such restrictions.
- SBLIs are a key feature of turbulent transonic and supersonic flows.
- RANS methods are able to predict shock-wave positions and main flow characteristics, but are limited to steady and one-dimensional solutions.
- LES are able to capture three-dimensional unsteady behavior, but they require wall-models to capture boundary layer effect with a reasonable computational effort.
- More study into wall-models development is encouraged, specially for compressible flows with SBLIs, in order to build flexible and reliable numerical tools.

Finally, multi-component flows were introduced in Chapter 5. Our hybrid scheme was upgraded and tested. These are the main conclusions:

- Multi-component formulation is required for a wide range of applications such as combustion in engines, energy generation and prediction of pollution emissions.
- Navier-Stokes equations are modified to include N new transport equations for the N considered species, and heat released by combustion. Energy required in the formation of new species have also to be taken into account.
- In multi-component flows, a new source of discontinuity may appear which is the fronts formed by different species.
- We have upgraded our shock detector to detect species and flames fronts in order to stabilize the numerical method.
- The new approach was tested in a non-reactive propane jet, showing its superior performance when compared to traditional approaches.

In addition to the conclusions regarding the work presented in this thesis, other related aspects are worth to be mentioned:

- The tools developed in this thesis have been presented for the first time in specialized seminars in master courses at UPC.
- Students have been able to develop their own Bachelor and Master thesis based on the tools presented in this work.
- As mentioned before, fellow researchers have built their own research on top of the numerical tools presented here in areas such as acoustics, combustion and turbulence modeling.
- All the computational tools developed in this thesis have been implemented in the TermoFluids commercial code.

6.2 Further research

Considering all the information gathered for the development of this thesis as well as the results obtained, some issues are encouraged to pursue (both in the context of compressible flows and CFD in general):

- As problems rise in computational cost, numerical methods have to be adapted in order to allow feasible simulations. In this thesis we have restricted ourselves to low-order numerical schemes on unstructured meshes. This kind of methods work well if the space and time resolution are small enough. This, however, results in extremely big meshes and very small time steps that ultimately can harm their flexibility in certain applications. High-order numerical methods emerge as an alternative to solve this issue. They do not require as much computational resources, but also have some limitations. A clear strategy to implement high-order schemes on unstructured meshes has not been found yet. Furthermore, dispersion errors introduced by low-order schemes make them unusable for acoustics applications, since wave speeds are misspredicted. It is clear than a flexible and accurate numerical scheme to solve every feature of compressible flows in the field of thermo-acoustics (aerodynamics, acoustics and combustion) has to be a high-order scheme. It is encouraged, then, the study of this kind of "one for all" methods. In this sense Discontinuous Galerkin Methods are an appealing alternative and they have grown its popularity in the CFD community lately.
- As already mentioned, compressible flows for practical applications are always turbulent and high-speed flows with very thin boundary layers. We have restricted ourselves to explicit time-marching methods, which requires very small time steps in order to provide accurate solutions. It is not worth having the best numerical scheme if time steps of the order of 10^{-10} s are required, the

simulation will never end. In this sense, implicit numerical schemes can alleviate this problem since they allow the use of larger time steps. However, some flow phenomena such as combustion have characteristics times that are indeed small and implicit schemes with big time steps would not capture them. It is encouraged, then, the study of flexible and computationally cost-effective wall models in order to overcome the restrictions of explicit (and implicit) schemes introduced by the boundary layer.

- Another research topic which require more study is combustion models. A vast amount of models exist, and they work well for some cases and not so well for others. Flexible models are required that can be used for the majority of applications.
- Finally, an interesting topic that not only affects compressible fluids but all the CFD community is the concept of smart adaptive grids. Considering the total amount of time spent in one simulation, the majority is required to build a mesh, test it, and rebuild it until some point. We can even spend a lot of time trying to figure out a problem in a numerical scheme when the real problem is in the mesh. Smart meshes could be generates automatically for a given geometry and adapt themselves to the flow features in order to achieve an optimal balance between computational cost and accuracy (for example clustering along walls to reproduce boundary layers and growing in the smooth parts of the flow to reduce the mesh where it is not needed). This feature would dramatically reduce the time invested in running simulations, increasing efficiency in the work process and reducing costs. The implementation of Artificial Intelligence techniques in the CFD domain could allow this feature and many others that could ultimately revolutionize how we do CFD today.

Appendix A

The Shock Tube Problem

Lets consider an infinite one-dimensional tube with a membrane in the section $x = 0$ that separates gas at rest with different thermodynamic properties (pressure, density and temperature). The pressure in the region $x < 0$ (the working gas), denoted by the subscript l , is higher than the pressure in the region $x > 0$ (the driven gas), denoted with the subscript r . At $t = 0$ the membrane suddenly breaks, generating the gas flow in the tube. In the lower pressure region a shock wave travels at a speed D , meanwhile in the higher pressure region an expansion waves occur. Between the heated gas and the gas left behind by the expansion a contact discontinuity is placed that travels at the local gas speed (velocity and pressure are constant through contact discontinuities).

If initially all the particles of the gas have the same value of entropy, and there are not shock waves in the evolution of the gas, the entropy is constant and equal in all the gas, this is what is called a homentropic flow. In this case the problem is easier to solve because the different thermodynamic variables can be expressed as a function of the entropy and another variable. The system become

$$\begin{aligned}\frac{dR^+}{dt} &= 0 \quad C^+ : \frac{dx}{dt} = u + a \\ \frac{dR^0}{dt} &= 0 \quad C^0 : \frac{dx}{dt} = u \\ \frac{dR^-}{dt} &= 0 \quad C^- : \frac{dx}{dt} = u - a\end{aligned}\tag{A.1}$$

where

$$R^+ = \int \frac{dp}{\rho a} + u \quad R^- = \int \frac{dp}{\rho a} - u\tag{A.2}$$

are the Riemann variables, which will remain constant when moving through x at a speed a with respect to the fluid. In the case of perfect gases (in which this work is

focused on), the homentropic relations are

$$\left(\frac{p}{p_0}\right)^{\frac{\gamma-1}{\gamma}} = \left(\frac{\rho}{\rho_0}\right)^{\gamma-1} = \left(\frac{a}{a_0}\right)^2 \quad (\text{A.3})$$

With p_0 , a_0 and ρ_0 constants. In this case, the Riemann variables are,

$$R^+ = \frac{2}{\gamma-1}a + u \quad R^- = \frac{2}{\gamma-1}a - u \quad (\text{A.4})$$

These simplifications can be used to find several analytical solutions in some special cases, such as the Riemann problem. The Riemann problem involves the computation of the Euler equations where the initial data is a piecewise function for the different thermodynamic variables with a jump discontinuity. The Sod's shock tube is an example of a Riemann problem, and it is also the basis of the development of upwind-like numerical schemes.

In order to obtain the exact solution, the tube is divided into several regions (see figure A.1). The characteristics that arrive at point A come from the line $t = 0$, i.e., the initial conditions.

$$R^+ = \frac{2}{\gamma-1}a_A + u_A = \frac{2}{\gamma-1}a_r \quad R^- = \frac{2}{\gamma-1}a_A - u_A = \frac{2}{\gamma-1}a_r \quad (\text{A.5})$$

It can be concluded that $a_A = a_r$ and $u_A = 0$. Therefore, the fluid remains at rest until the shock wave forces the flow. This is a coherent result since the shock wave travels at a relative speed with respect to the fluid higher than the speed of sound, so the first perturbation of the fluid in the region r is due to the shock wave. In order to find the properties behind the shock wave, the Rankine-Hugoniot relations must be applied,

$$\frac{\rho_2}{\rho_1} = \frac{(\gamma+1)M^2}{2+(\gamma-1)M^2} \quad \frac{u_2^{rel}}{u_1} = \frac{\rho_1}{\rho_2} \quad (\text{A.6})$$

$$\frac{p_2}{p_1} = \frac{2\gamma M^2 - (\gamma-1)}{\gamma+1} \quad \frac{T_2}{T_1} = \left(\frac{a_2}{a_1}\right)^2 = \frac{p_2 \rho_1}{p_1 \rho_2} \quad (\text{A.7})$$

Where the subscript 1 denotes the conditions in front of the shock wave and the subscript 2 denotes the conditions behind the shock wave. The Mach number of the shock wave is $M = D/a_r$. The value of the velocities are relative to the shock wave, but the absolute values must be used : $u_1 = D - u_a = D$ and $u_2 = D - u_2^{rel}$. The discontinuity produced by the shock wave can be reinterpreted as new boundary conditions for the fluid since the values of the Riemann variables have changed. The

C^+ characteristics behind the shock wave are parallel to it, therefore only C^- and C^0 arrive at point P .

$$R^- = \frac{2}{\gamma-1}a_P - u_P = \frac{2}{\gamma-1}a_2 - u_2 \quad C^0 : \frac{dx}{dt} = u_p = u_2 \quad (\text{A.8})$$

Hence, $a_P = a_2$ and $u_P = u_2$. The properties of the fluid between the shock wave and the contact discontinuity remain constant. As it can be seen from figure A.1 the contact discontinuity is a C^0 characteristic, and because there is no flux through the discontinuity, the local velocity must be equal at both sides (and then the lines C^0 have the same slope in front of the contact discontinuity and behind). The contact discontinuity equation of motion is, therefore, $x = u_2 t$ and its speed is u_2 .

Concerning the expansion region, it can be concluded (following the same procedure that in A) that $a_B = a_l$ and $u_B = 0$. The region under the line $x = a_l t$ corresponds to the fluid that has not been affected by the expansion wave yet. At R arrives the characteristic C^+ from B and the characteristics C^- from the origin

$$R^+ = \frac{2}{\gamma-1}a_R + u_R = \frac{2}{\gamma-1}a_l \quad C^- : x = (u_R - a_R)t \quad (\text{A.9})$$

Combining the previous expressions one gets,

$$a_R = \frac{2a_l}{\gamma+1} \left(1 - \frac{\gamma-1}{2} \frac{x}{a_l t} \right) \quad u_R = \frac{2a_l}{\gamma+1} \left(\frac{x}{a_l t} + 1 \right) \quad (\text{A.10})$$

Finally, the point Q is intersected by C^+ arriving from R and C^- arriving from the contact discontinuity.

$$R^+ = \frac{2}{\gamma-1}a_Q + u_Q = \frac{2}{\gamma-1}a_l \quad R^- = \frac{2}{\gamma-1}a_Q - u_Q = \frac{2}{\gamma-1}a_c^- - u_c \quad (\text{A.11})$$

Notice that the speed of sound behind the contact discontinuity, a_c^- , is unknown. The pressure and relative velocity through the contact discontinuity are constant, but it cannot be said the same for the rest of properties. It is needed, then, the third characteristic.

$$C^0 : \frac{dx}{dt} = u_Q = u_c = u_2 \quad (\text{A.12})$$

Finally

$$a_c^- = a_Q \quad a_Q = a_b - \frac{\gamma-1}{2}u_2 \quad u_Q = u_2 \quad (\text{A.13})$$

The upper limit of the expansion is given by the conditions in Q , and corresponds to the last C^- with $a_d = a_Q$ and $u_d = u_Q$.

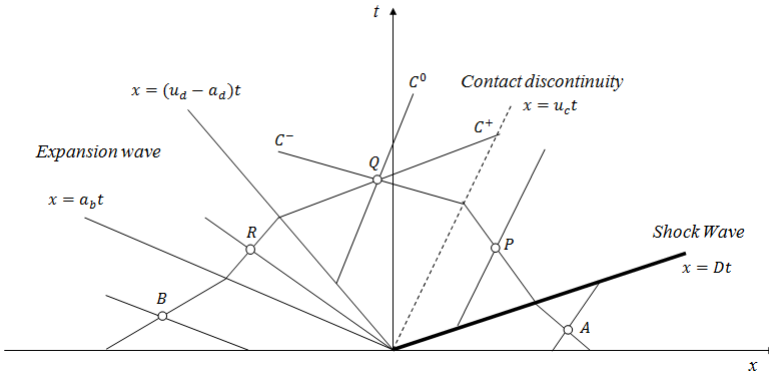


Figure A.1: Diagram of the shock tube solution.

At this point, all the relations required to get the exact solution for the shock tube problem have been developed. The isentropic relations (A.3) give us the rest of magnitudes. Notice that if D is not data, the solution must be obtained by an iterative process. Setting the condition that in the contact discontinuity the pressure must remain constant one obtain,

$$\frac{p_l}{p_r} = \frac{2\gamma D^2 - (\gamma - 1)}{(\gamma + 1) \left[1 + \frac{(\gamma - 1)D}{2} \frac{a_r}{a_l} \left(\frac{2 + (\gamma - 1)D^2}{(\gamma + 1)D^2} - 1 \right) \right]^{\frac{2\gamma}{\gamma - 1}}} \quad (\text{A.14})$$

Which is an implicit equation for D . An algorithm to solve the problem would look like this:

- Define initial Riemann problem: p_l, ρ_l, u_l and p_r, ρ_r, u_r .
- Find D from equation A.14 with an iterative process.
- Use equations A.6 and A.7 to find the jump relations through the shock wave.
- Use the Riemann variables in each zone to find the rest of values.

Appendix B

Computing Resources

The different numerical methods presented in the context of this thesis have been implemented in C++. The Object Oriented Programming paradigm and the MPI protocol is used to allow multi-cpu usage. The code is based on the OML library developed by TermoFluids SL [1]. The work presented in this thesis has allowed TermoFluids to work with compressible flows, previously it was restricted to incompressible flow studies. It has been also the objective of this thesis to implement all the advances resulting from this thesis in order to expand TermoFluids' range of applications.

The majority of the simple cases presented in this thesis have been tested in a quad-core Intel Core i5 CPU, with 8 Gb of RAM. Bigger cases, however, have been run in the CTTC JFF-Cluster (<http://www.cttc.upc.edu/node/29>) and in BSC-MareNostrum 3 (<2017) and 4 (2017) (<https://www.bsc.es/marenostrum/marenostrum>).

References

- [1] O. Lehmkuhl, C D. Pérez-Segarra, R. Borrell, M. Soria, and A. Oliva. TERMOFLUIDS: A new Parallel unstructured CFD code for the simulation of turbulent industrial problems on low cost PC Cluster. *Proc. Parallel CFD Conf.*, pages 1–8, 2007.

Appendix C

Publications

This is a list of publications derived from the work presented in this thesis:

- A. B  ez Vidal, J.B. Pedro, O. Lehmkuhl, Ivette Rodr  guez and Carles D. P  rez-Segarra. *Comparing Kinetic Energy Preserving and Godunov Schemes on the flow around a NACA0012*. WCCM XI - ECCM V - ECFD VI, July 20-25, 2014, Barcelona.
- J.B. Pedro, A. B  ez Vidal, O. Lehmkuhl, C. D. P  rez Segarra and A. Oliva. *On the extension of RANS/LES methods from incompressible to compressible transonic turbulent flows with SBLI*. Turbulence, Heat and Mass Transfer 8, September 15-18, 2015, Sarajevo.
- J.B. Pedro, A. B  ez Vidal, O. Lehmkuhl, C. D. P  rez Segarra and A. Oliva. *On the extension of LES methods from incompressible to compressible turbulent flows with application to turbulent channel flow*. 7th European Thermal-Sciences Conference, EUROTHERM 2016, Krakow, Poland.
- J. Ventosa-Molina, J.B. Pedro, C.D. P  rez-Segarra, J. Rigola, A. Oliva. *Application of shock detectors to capture flame fronts*. 8th European Combustion Meeting 2017, Dubrovnik, Croatia.

